# UNIVERSITY OF TRENTO

PhD Program in Biomolecular Sciences
Department of Cellular, Computational
and Integrative Biology – CIBIO
34° Cycle

## "Role of chromatin condensates in tuning nuclear mechano-sensing in Kabuki Syndrome"

Tutor
Prof. Dr. Alessio Zippo
*Laboratory of Chromatin Biology and Epigenetics*
*CIBIO, University of Trento*

Ph.D. Thesis of
Sarah D'Annunzio
*CIBIO, University of Trento*

Academic Year 2022-2023

## Declaration of original authorship

I Sarah D'Annunzio confirm that this is my own work and that the use of all material from other sources has been properly and fully acknowledged.

# Contents

# List of figures

# Abstract

The human genome is characterized by an extent of functions that act further than its genetic role. Indeed, the genome can also affect cellular processes by nongenetic means through its physical and structural properties, specifically by exerting mechanical forces that shape nuclear morphology and architecture.

The balancing between two chromatin compartments with antagonist functions, namely Transcriptional and Polycomb condensates, is required for preserving nuclear mechanical properties and its perturbation is causative of the pathogenic condition Kabuki syndrome (KS) (Fasciani *et al.*, 2020).

KS is a rare monogenic disease caused by the haploinsufficiency in the *KMT2D* gene encoding for MLL4, a H3K4-specific methyltransferase important for the regulation of gene expression. By interrogating the effect of *KMT2D* haploinsufficiency in Mesenchymal Stem Cells (MSCs) we discovered that MLL4 loss of function (LoF) impaired Polycomb-dependent chromatin compartmentalization, altering the nuclear architecture and the cell mechanoresponsiveness during differentiation (Fasciani *et al.*, 2020). These results suggest that altered nuclear mechanics rely on chromatin architecture and could potentially lead to changes in cell responses to external mechanical stimuli.

In the present work, we investigated the role of Transcriptional and Polycomb condensates in tuning nuclear responses to different external mechano-physical conditions. To affect nuclear mechanics, we employed the use of several mechanical devices (e. g. substrate stiffness, microchannels with constrictions, and cell confinement). We found that Polycomb and Transcriptional condensates are modulated by changes in substrate rigidity in healthy conditions and that MLL4 LoF impairs the MSCs nuclear condensates-driven mechanical response. Furthermore, we observed that MLL4 LoF impacts nuclear adaptation to confined spaces by incrementing susceptibility to nuclear envelope rupture. We also showed that the increased nuclear fragility in MLL4 LoF is accompanied by an alteration of cell migratory capacity and survival rate.

Altogether these findings suggest that MLL4 LoF impairs cell responses to external mechanical stimuli, shedding light on the pathological connection between the

32      altered cell mechanoresponsiveness during differentiation and KS phenotype in terms of skeletal and cartilage anomalies.

# 1. Introduction

## 1.1 Kabuki Syndrome (KS)

Kabuki syndrome (OMIM #147920) is a congenital syndrome firstly described in Japan in 1981 (Niikawa *et al.*, 1981). The name of the syndrome was provided by Niikawa *et al.* because the affected individuals showed peculiar facial dysmorphisms, reminiscent of actors' stage make-up in the traditional Japanese Kabuki theater. Besides these distinctive facial features, affected individuals present a broad spectrum of abnormalities.

It is a rare genetic disease, with autosomal dominant inheritance and a prevalence of 1 per 32,000 individuals (Niikawa *et al.*, 1988).

### 1.1.1 Clinical features

Being a complex disorder, KS is characterized by multiple abnormalities and a wide variety of additional symptoms affecting different organs. The disease progress with age, involving different tissues and systemic function, making it challenging for pediatricians to make a clinical diagnosis. Nonetheless, KS can be diagnosed on the basis of the existence of the following features (Cheon and Ko, 2015):

34

36

38

40

42

44

46

48

50
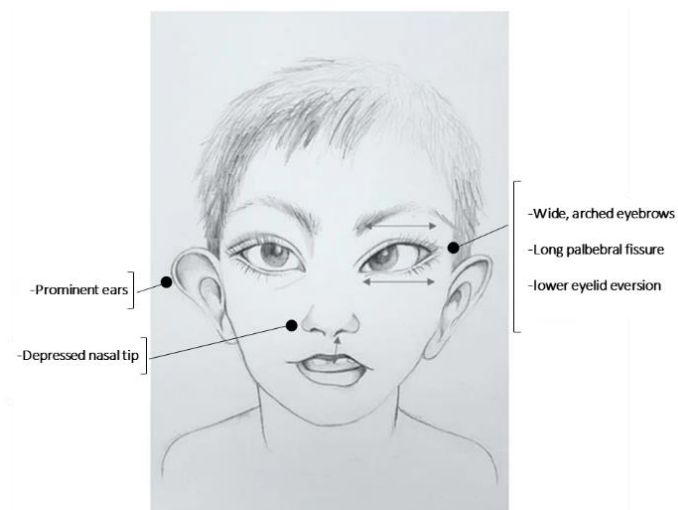
- craniofacial anomalies (arched eyebrows with lateral sparseness, eversion of the lower lateral eyelid, depressed nasal tip, and cupped ears) (Figure 1);
- skeletal anomalies (deformed spinal column with vertebrae malformations, cranial abnormalities);
- postnatal growth retardation (partially linked to feeding problems in infancy);
- infantile muscle hypotonia;
- persistent fetal finger pads;
- varying degrees of intellectual disability.

Cardiac malformations are also common in individuals affected by KS: congenital heart defects are reported with a frequency of approximately 40% and 50%, with most frequent malformations being atrial septal defects, and ventricular septal defects and aortic coarctation (Boniel *et al.*, 2021).

Individuals affected by KS also show a high prevalence of immunopathological manifestations which may worsen the general symptomatology: 44.1% and 58.2% of KS individuals exhibit infection susceptibility and hypogammaglobulinemia, respectively; 13.6% have an autoimmune disease, with the most frequent manifestation being immune thrombocytopenic purpura (7.3%) and autoimmune hemolytic anemia (4.0%) (Margot *et al.*, 2020).

Even though the genetic cause of the disease is known, up to the present time there is no cure for KS and treatments aim to relieve individual symptoms, reduce the risk of complications and improve the quality of life of the affected individuals.

### 1.1.2 Genetic etiology

14

In 2010 whole-exome sequencing led to the identification of heterozygous loss of function mutations in the *KMT2D* gene encoding for MLL4 as

causative of KS (Ng *et al.*, 2010).

They performed the exome sequencing of 10 unrelated individuals and

identified heterozygous nonsense or frameshift mutations in the *KMT2D* gene in 7 individuals. Follow-up Sanger sequencing detected *KMT2D*

mutations in 2 of the 3 remaining individuals and 26 of 43 additional cases. In all, they identified 33 distinct *KMT2D* mutations in 66% of affected

individuals. In the cases for which DNA from both parents was available, the *KMT2D* mutation was found to have occurred *de novo* in the majority

of cases, whereas parent to child transmitted mutations were found in a lower percentage.

Two years later, another group (Lederer *et al.*, 2012) identified heterozygous mutations in *KDM6A*, the gene encoding the Lysine-specific

demethylase 6A (Ubiquitously transcribed tetratricopeptide repeat, X chromosome -UTX), as causative of KS in *KMT2D*-mutation-negative

individuals, describing three KS girls with de novo partial or complete deletions in *KDM6A* gene.

Altogether the mutation detection rate in KS affected individuals is about 75% for *KMT2D* mutation and 5% for *KDM6A* (Boniel *et al.*, 2021).

About 35-37% of the mutations identified so far are stop and frameshift mutations that generate a truncated form of the protein, leading to

haploinsufficiency Missense mutations and splice-site mutations were
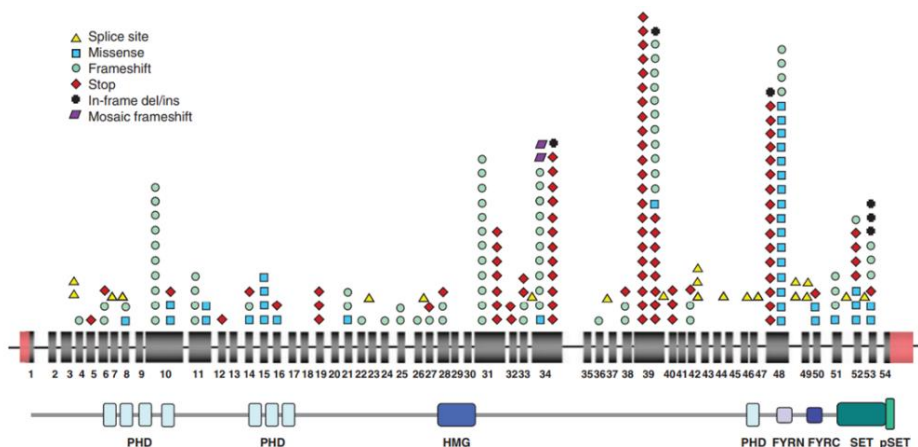
found in a minority of cases, with a frequency of 16 and 9%, respectively. Only 3% of the mutations are in-frame deletions or duplications. Overall these mutations do not show any significant mutational hot spot in a specific exon, although the ones occurring in *KMT2D* appear to be particularly enriched toward the C-terminus (Bögershausen and Wollnik, 2013) (Figure 2).

## 1.2 MLL4: role and function

### 1.2.1 MLL4-COMPASS complex

The *KMT2D* gene encodes for MLL4 protein, a histone methyl-transferase that deposits a monomethyl group on H3 lysine 4, a hallmark of an active transcription state. MLL4 is part of a macromolecular complex, named the COMPASS complex (Complex Proteins Associated with Set1), within which it interacts with its complex-specific subunit UTX, a histone H3 lysine 27 (H3K27) demethylase, encoded by *KDM6A* (Sze and Shilatifard, 2016). Like all the histone methyltransferases, MLL4 possesses a highly conserved SET domain, which is responsible for the methyl-transferase activity, and the post-SET domain, both at the C-terminus. MLL4 protein has several plant homeodomain (PHD) fingers, a high-mobility group (HMG), and two FY-rich (FYR) motifs (Figure 2). Beyond UTX, other subunits, such as PTIP (PAX transcription activation domain interacting protein), PA1 (PAXIP1-associated glutamate-rich protein 1), and NCOA6 (Nuclear Receptor Coactivator 6) were found to be associated with MLL4. Other proteins present within the complex are shared among all the MLL family members including WDR5 (WD repeat-containing protein 5), RbBP5 (Retinoblastoma-binding protein 5), ASH2L (Set1/Ash2 histone methyl-transferase complex subunit ASH2), and DPY30 (Protein dpy-30 homolog)

16

(Sze and Shilatifard, 2016). Considering that MLL proteins antagonize Polycomb group proteins (PcGs) in the regulation of gene expression and that they bear homology to the Drosophila protein TrxG (trithorax), these enzymes are also referred to as the trithorax group proteins.

## 1.2.2 Molecular pathogenesis

During development and in adult organisms, TrxG plays an important role in the epigenetic regulation of transcription, where they act as the antithetical factors to repressive PcG (Bögershausen and Wollnik, 2013). Of note, the fine-tuning of gene expression in space and time is required for a proper cell lineage commitment during differentiation and tissue homeostasis (Chou *et al.*, 2016).

Precise spatiotemporal patterns of gene expression are controlled, among other factors, by *cis*-regulatory elements known as enhancers, which are capable to boost the transcription of related promoters over long genomic distances (up to few megabases) (Fagnocchi, Poli and Zippo, 2018). These noncoding DNA sequences contain arrays of short modules that serve as binding sites for sequence-specific transcription factors, which recruit a combination of components that in concert dictate the function of the enhancer (Maniatis *et al.*, 1987; Calo and Wysocka, 2013). Chromatin signatures for enhancers include Histone post-translational modifications (PTMs) and chromatin features, such as increased chromatin accessibility. For instance, one of the PTMs that prime active enhancers is H3K4me1, introduced by the MLL4 complex. H3K27ac is deposited upon enhancer activation, and since it is highly enriched on active enhancers it is commonly used for their genome-wide identification (Fagnocchi, Poli and Zippo, 2018). Poised or repressed enhancers bear instead H3K27me3, the repressive histone modification introduced by PcG (Kim and Shiekhattar, 2015).

Several players orchestrate the deposition of the histone marks which specify the function of enhancers. Interestingly, within the MLL4 complex, it has been suggested that UTX may act as an enhancer-specific H3K27 demethylase to facilitate the transition from inactive to active enhancers (Herz *et al.*, 2012).

The MLL4 complex acts as a major enhancer regulator in mammalian cells, affecting several biological processes, including development and differentiation.

Considering the role of MLL4 in orchestrating the interplay of different epigenetic marks during development, it is not surprising that the dysregulation of this complex leads to a developmental disorder such as KS, even though the underlying pathogenesis of the disease remains unclear.

For instance, MLL4 is essential for regulating cardiac gene expression during heart development (Ang *et al.*, 2016). This notion sheds light on the pathological connection between cardiac defects and *KMT2D* mutations in KS. Another study in 2015 demonstrated the critical roles of MLL4 in craniofacial, heart, and brain development by knocking down the zebrafish orthologues of *KMT2D* and *KDM6A*. Knock-down animals showed defects in tissues affected in the majority of individuals affected by KS (Van Laarhoven *et al.*, 2015). More recent work reported that MLL4 regulates the development of growth hormone-releasing hormone (GHRH)-producing neurons in the mouse hypothalamus, suggesting that the dysregulation of MLL4 transcriptional control plays a role in the development of GHRH-neurons and dwarfism phenotype in mice, a feature also present in KS individuals (Huisman *et al.*, 2021).

Furthermore, *KMT2D* is one of the most inactivated epigenetic modifiers in cancer, with a tumor-suppressive role. It has recently been published that lung-specific *KMT2D* deficiency promotes tumorigenesis in mice and upregulates pro-tumorigenic programs, such as glycolysis (Alam *et al.*, 2020). Although cancer has been reported in some individuals with KS,

186         there is so far no clear association between KS and an increased risk for

        cancer (Bögershausen and Wollnik, 2013).

188

## 1.3 Mesenchymal Stem Cells (MSCs): a Kabuki Syndrome disease model

190     In order to dissect the molecular mechanisms behind KS pathogenesis, an *in vitro*

    model of the disease has been developed in the laboratory where I worked during

192     my PhD. Considering that the tissues that are mostly affected by KS symptoms are

    bones, cartilages, and tendons and that they all share as common precursor

194     mesenchymal stem cells (MSCs), the rationale for developing the *in vitro* model was

    to use these cells.

196     To study the effect of MLL4 loss of function (LoF) in KS, a frameshift mutation in the

    coding region (exon 39) of *KMT2D* via CRISPR–Cas9-mediated editing was inserted.

198     In this way, we generated two MSCs independent clones (MLL4$^{Q4092X}$ and MLL4$^{P4093X}$)

    carrying heterozygous frameshift mutations that truncate the MLL4 protein

200     (Fasciani *et al.*, 2020) (Figure 3). Specifically, we found that, despite the unaltered
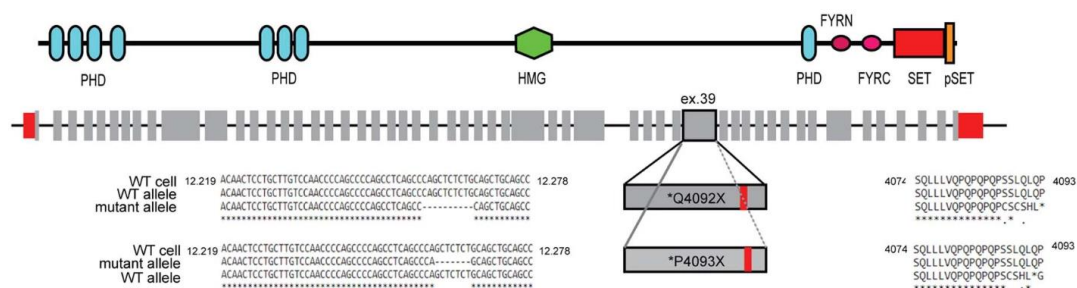


*Figure 3. An illustration of the KMT2D gene and its corresponding protein.* *The position of the inserted mutations Q4092X/ P4093X and the relative changes in the coding sequences are highlighted (Fasciani et al., 2020).*

    transcript levels, the presence of the mutations reduced the protein abundance of

202     MLL4. Of importance, in the same setting, we determined a parallel reduction of

    UTX, suggesting that its protein stability is regulated by the abundance of MLL4, in

204     line with previous findings (Herz *et al.*, 2012). This reduction was also mirrored by a

    decrease in H3K4me1 and H3K27ac levels. The mutation did not alter instead the

206     abundance of other components of the MLL4–COMPASS complex such as WDR5 and

PA1. These results have also been confirmed in primary fibroblasts isolated from individuals affected by KS.

We further investigated whether the presence of the frameshift mutation in the aforementioned chromatin regulator might affect nuclear compartments associated with transcriptionally active and repressed chromatin states.

Interestingly, we found that MLL4 LoF mutation leads to an unbalance between these two nuclear compartments, resulting in an increased abundance of PcG proteins and decreased levels of enhancer-associated cofactors MED1 and BRD4, which mirror the pattern of MLL4.

Surprisingly, the changes of these chromatin states are associated with nuclear morphological alterations and differentiation defects, indicating a key role of MLL4 in the maintenance of nuclear mechanics and cell fate determination (Fasciani *et al.*, 2020)

## 1.4 Phase separation guides nuclear condensates assembly

Liquid-liquid phase separation (LLPS) has recently been proposed to be among the physical processes that can guide nuclear compartmentalization and it is emerging as a model to explain the self-assembly and organization of membrane-less bodies within the cell. These bodies appear as droplets and are called biomolecular condensates (Sabari, Dall'Agnese and Young, 2020).

There are several levels of biomolecular condensates inside the nucleus (in this case also referred to as nuclear condensates), such as interactions between histone tails, transcriptional condensates involving the interplay between enhancer elements, and transcription factors, and gene-silenced regions compacted in heterochromatin (Feric and Misteli, 2021).

### 1.4.1 Liquid-liquid phase separation

LLPS is a phase transition process whereby a substance changes from one physical state to another (e.g. solid to liquid transition). In biological systems, LLPS occurs when a supersaturated solution of macromolecules

236      (proteins and nucleic acids) spontaneously separates into two coexisting phases, a dense phase that is enriched for these macromolecules and a

238      phase that is depleted from them (Figure 4). The interface between these droplets acts as a boundary that allows the selective passage of specific

240      molecules, thus giving liquid droplets the possibility to function as membrane-less compartments (Alberti, 2017).

242      Among the factors that can influence the phase separation behavior of proteins, there are:

244
- weak multivalent interactions that can be promoted by

    a) the presence of Intrinsically Disordered Regions (IDRs) which are

246           characterized by low sequence complexity and do not contain sufficient hydrophobic amino acids to induce cooperative folding.

248           They contain a higher proportion of polar or charged amino acids and do not fold into a three-dimensional structure;

250         b) modular protein domains;

- protein solubility;

252
- physical and chemical parameters (e.g. temperature, ionic strength);

- local availability of interactors or binding partners (e.g. other proteins,

254     nucleic acids);

- Post Translational Modifications (PTMs).

256     All the above-mentioned factors have the ability to tune the critical concentration (C critical) above which phase separation occurs. The phase-

258     separated droplets are steady as long as the total concentration is above the critical threshold of concentration, but once the total protein

260     concentration falls below this threshold again, the molecules come back to be evenly distributed (Figure 4) (Alberti, 2017). For instance, the
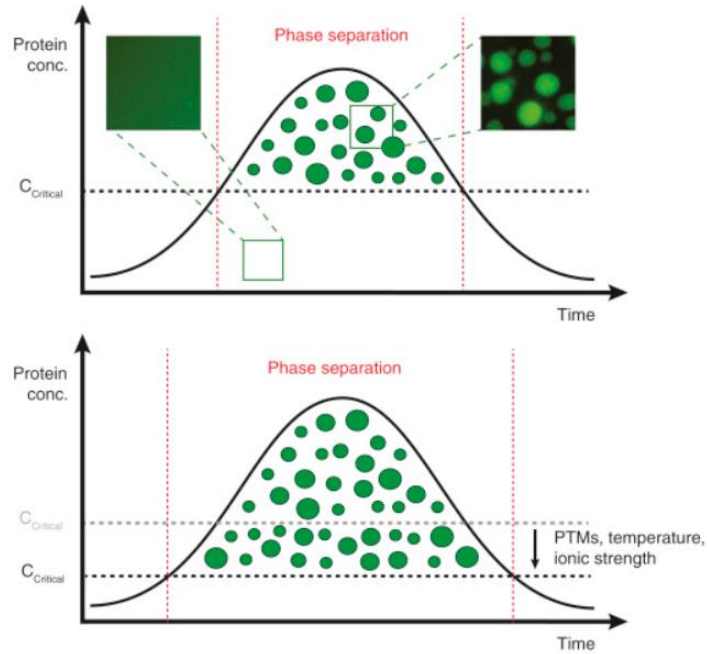
*Figure 4. Phase diagram for LLPS. A protein forms LLPS above the C critical for phase separation.* The phase-separated droplets are stable as long as the total concentration is above the critical threshold of concentration, but once the total protein concentration falls below C critical the molecules come back to a one-phase state (Alberti, 2017).

262      presence of IDRs within protein amino acids sequence reduces the

solubility of proteins in water and promotes multivalent interactions, thus

264      lowering the C critical for reaching phase separation and allowing

compartmentalization at lower concentrations. Importantly, a protein's

266      IDR is frequently assumed to be diagnostic of its ability to go through phase

separation (Martin and Holehouse, 2020).

268

## 1.4.1.1 Biological functions of Liquid-liquid phase separation

The cellular space is finely organized in membrane-bound and membrane-

270      less compartments to allow control over biochemical reactions in space

and time (Feric and Misteli, 2021). One mechanism to reach

272      spatiotemporal control is to physically organize in the cell the localization

of reaction components. For example, reaction kinetics can be increased

274      by concentrating these components or inhibited by segregating them in a

confined space (Banani *et al.*, 2017). Classic organelles are able to

276      surround reactions with their lipid bilayer membranes and regulate their

22

content by specialized transport machinery, securing the long-term stability of reactions. However, many cellular compartments, such as nucleoli and Cajal bodies in the nucleus, as well as stress granules in the cytoplasm, are able to achieve spatiotemporal control of biochemical reactions without any physical barrier (Feric and Misteli, 2021). In condensates, phase boundaries permit molecules to concentrate within "droplets" while continuously exchanging with the surrounding, allowing a flexible regulation of single components in a highly dynamic and reversible system. The physicochemical characteristics of condensates present unique features for controlling the biochemical environment of the cell. As previously mentioned, biomolecular condensates can strongly affect cellular processes by increasing or inhibiting reaction kinetics by sequestration, as well as determining reaction specificity, with the important advantage of rapidly switching on and off the formation and the dissolution of the condensates (Banani *et al.*, 2017).

## 1.4.2 Nuclear condensates

Several nuclear regulatory activities take place in biomolecular condensates, where proteins and nucleic acids are concentrated or selectively portioned at specific genomic loci for promoting processes like DNA replication, DNA repair, transcription, and chromatin remodeling (Sabari, Dall'Agnese and Young, 2020) (Figure 5).
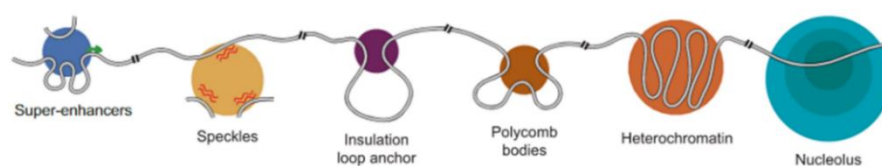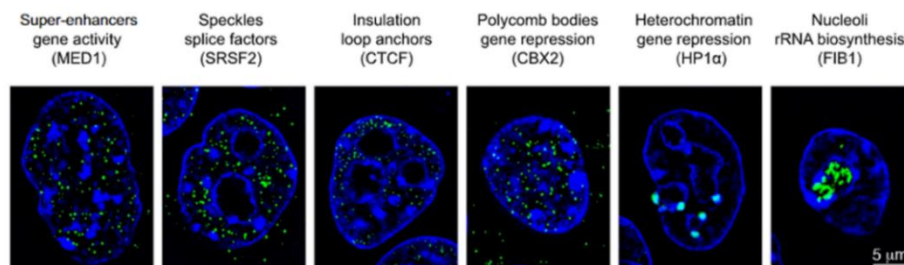
*Figure 5. Example of nuclear condensates. Top panel: Immunofluorescence images acquired by Structured Illumination Microscopy for the target protein indicated in parentheses (in green in the images, the blue color represents nuclei). For each nuclear condensate is specified its name and function. Bottom panel: Cartoon explaining the organization of nuclear condensates (grey line: chromatin fiber, green arrow: active transcription start site, red squiggled lines: RNA) (Sabari, Dall'Agnese and Young, 2020). Abbreviations: CTCF (CCCTC-binding factor), FIB1 (fibrillarin), SRSF2 (Serine/arginine-rich splicing factor 2).*

In 2017, A. R. Strom et al. provided the first evidence that chromatin compartmentalization is mediated by LLPS (Strom et al., 2017). Specifically, they found that the formation of heterochromatin domains is driven by phase separation through the condensation of HP1a (heterochromatin protein 1) in both Drosophila and mammalian cells. Their model of heterochromatin formation explains how the process starts with nucleation of HP1a, in which the highly mobile protein forms foci via multivalent, weak hydrophobic interactions, and how these foci undergo maturation over time by forming larger domains through condensates coarsening. Ultimately, mature domains are formed of both chromatin-bound HP1, an immobile fraction of HP1 that identified stable compartments, and a liquid, mobile and dynamic one.

One year later, another study proposed a phase separation model for transcriptional control at super-enhancers sites, which consist of clusters of enhancers that are densely occupied by transcription factors, cofactors, and chromatin regulators (Sabari *et al.*, 2018) (Hnisz et al., 2013). B. R. Sabari *et al.* discovered that coactivators of transcription such as MED1 (Mediator Complex Subunit 1) and BRD4 (Bromodomain-containing protein 4) form liquid-like condensates that compartmentalize the transcription machinery at super-enhancer sites at cell identity genes, bridging interactions between chromatin, TFs and RNA polymerase II (Sabari *et al.*, 2018). This phenomenon was proposed to explain the bursting behavior of transcription and the simultaneous activation of multiple genes, ensured by the high local concentrations of the transcriptional apparatus and the high frequency of interactions between super-enhancer sites and the promoter of the regulated genes within condensates. Considering their critical role in transcription, these types of

biomolecular condensates are also specifically called transcriptional condensates (Sabari et al., 2018). Of notice, in our last work, we demonstrated that MLL4 is among the proteins that participate in the transcriptional condensates, of which controls assembly and clustering dynamics (Fasciani et al., 2020). Indeed, the presence of MLL4 LoF mutation reduces the nucleation efficacy and the kinetics of transcriptional condensates.

Another example of nuclear condensates, with opposite function with respect to the one just described, are the PcG condensates. For instance, it has been demonstrated that PRC1 Polycomb subunits can promote the formation of multi-component condensates through which they can induce the writing of repressive histone marks which subsequently drive chromatin compaction (Eeftens et al., 2021). In another work, it has been seen that the phase separation behavior of PRC1 is specifically driven by the CBX2 (chromobox protein homolog 2 subunit), and that point mutations in its internal domain that abrogate nucleosome compaction in vitro and induce developmental defects in mice also disrupt phase separation (Plys et al., 2019).

## 1.4.2.1 Nuclear condensates affect chromatin structure

All the examples of nuclear condensates suggest that LLPS can play important roles in chromatin compartments reorganization. Indeed, as previously mentioned, phase separation can drive chromatin compaction through the condensation of HP1a and Polycomb proteins.

The spatial organization of chromatin can be finely tuned by biomolecular condensates to concentrate molecules at specific genomic loci and enhance biological relevant processes, as in the case of transcriptional condensates. The phase separation of chromatin itself, driven by histone tails in physiologic salt conditions, together with the one of other chromatin-binding proteins, enables the establishment and maintenance

of chromatin sub-compartments (Gibson *et al.*, 2019). Gibson *et al.* identified several factors that mediate the intrinsic ability of chromatin to undergo LLPS. For instance, the linker histone H1, which binds to the nucleosome and is involved in chromatin condensation, increases the density of droplets while decreasing their dynamics. On the contrary, acetylation of histone tails causes the dissolution of chromatin droplets, which can be restored by the addition of the multi-bromodomain containing protein BRD4, which is able of associating with acetyl-lysine modifications in a multivalent manner. The highly acetylated chromatin gives rise to a new phase-separated state with droplets having distinct physical properties, which can be immiscible with unmodified chromatin droplets, mimicking nuclear chromatin subdomains. These findings suggest that the recognition of histone modifications by chromatin-binding proteins may locally induce or facilitate the formation of genomic compartments (Gibson *et al.*, 2019).

Another mechanism underlying the phase separation of heterochromatin was identified by Sanulli *et al*., which demonstrated that the binding of multiple molecules of Swi6, the *Schizosaccharomyces pombe* HP1 protein, to the nucleosome triggers a conformational change in the nucleosome that results in increased dynamics and accessibility of buried core histone residues. Swi6 simultaneously engages the H3K9me3 mark, the α-helix in H2B, and nucleosomal DNA, destabilizing histone–histone and histone–DNA interactions within the nucleosome. This allows buried regions of the nucleosome to be exposed to additional multivalent inter-nucleosomal interactions that promote LLPS (Sanulli *et al.*, 2019).

Overall, these studies demonstrate that chromatin can undergo LLPS under physiological conditions and that this intrinsic physicochemical property can be regulated.

## 1.5 Non-genetic function of the genome

Besides its genetic functions, the genome could also affect cellular processes by non-genetic means through its physical and structural properties, specifically by exerting mechanical forces that shape nuclear morphology and architecture (Bustin and Misteli, 2016). Indeed, chromatin can be considered a viscoelastic polymer with a mass, volume, and density determined by intra-fiber, intra-chromosomal, and inter-chromosomal interactions (Figure 6). As a physical entity, the genome is not only
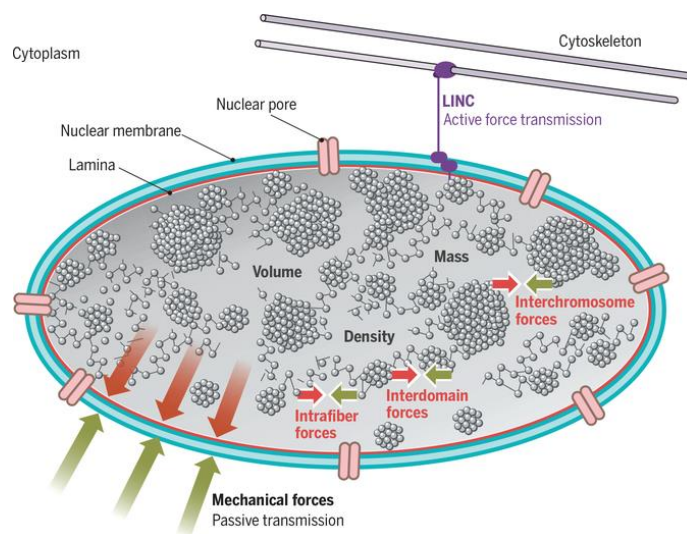


**Figure 6. The genome as a physical entity with a mass, volume, and density.**
*In the nucleus, the genome exerts (red arrows) and is exposed to (green arrows) mechanical forces which may be transmitted either in a passive way (contact points between the nuclear envelope and chromatin) or in an active way (via the LINC complex) (Bustin and Misteli, 2016).*

committed to establishing forces between chromatin domains, but it is also able to exert mechanical forces that are then transmitted from the nucleus to the cytoplasm via the LINC complex, the linker between the nucleoskeleton and the cytoskeleton. The non-genetic function of the genome comprehends its role in affecting nuclear morphology, the cellular response to mechanical forces, cell migration, cell signaling, and physiological functions such as vision in nocturnal animals.

Demonstration of the structural function of the genome in establishing nuclear architecture comes from the finding that microinjection of bacteriophage λ DNA into Xenopus eggs causes the assembly around the genetic material of double-bilayer membranes, resembling typical eucaryotic cell nuclei (Forbes, Kirschner and Newport, 1983). Another scaffold function of the genome refers to its involvement

in nuclear assembly during the formation of nuclear pore complexes (NPCs); the nuclear pore protein ELYS initiates the assembly process by mediating the interactions between chromatin and the NPC (Inoue and Zhang, 2014).

Furthermore, several studies suggest that peripheral heterochromatin does not serve only as a means to facilitate gene silencing, but also enhances the structural robustness of the nucleus, strengthening its ability to withstand physical challenges (Bustin and Misteli, 2016).

Interestingly, various observations also indicate a non-genetic signaling activity of chromatin. Indeed, the condensation status of the chromatin can be sensed by components of the DNA damage response (DDR) machinery. For instance, the cell cycle checkpoint kinase ATR is activated in response to changes in chromatin structure induced by mechanical strain (e.g. unwinding during replication) (Kumar *et al.*, 2014).

The non-genetic property of the genome can also affect the biological functions of an entire tissue as is seen in the physiology of vision in nocturnal animals. Comparative analysis of the genome organization in rod photoreceptor cells from distant species revealed an association between heterochromatin organization and the capacity of night vision in animals. Of note, in rod cells of nocturnal animals, the majority of the heterochromatin is in the nuclear interior instead of being at the nuclear periphery. The inverted pattern of heterochromatin location is evolutionarily beneficial, leading to an increased refractive index at the center of the nucleus, thereby reducing the scattering of the light (Solovei *et al.*, 2009).

## 1.5.1 Factors defining the nuclear mechanical properties

Besides chromatin, other nuclear components defining the mechanical properties of the nucleus are the nuclear envelope and the nucleo-cytoskeletal connections (LINC complex) (Bustin and Misteli, 2016).

The nuclear envelope (NE) encloses the genome and comprises three structures: the nuclear membrane, the nuclear pore complex (NPC), and the lamina. The nuclear membrane is divided into the inner nuclear

28

membrane (INM) and outer nuclear membrane (ONM), which are contiguous with each other and with the ER. The nuclear membrane restricts nuclear–cytoplasmic trafficking to the NPCs, regulating the passage of macromolecules between the nucleus and the cytoplasm with molecular weights above ∼40 kDa (Hatch and Hetzer, 2014). The nuclear lamina is formed by a dense meshwork of several lamin filaments attached to the INM. There are two types of lamin proteins, which are different isoforms of the same gene: the B-type (lamins B1 and B2) and the A-type (lamins A and C) (Dechat *et al.*, 2010). The lamin proteins have contacts on one side with the nuclear membrane by interacting with transmembrane INM proteins (e.g. lamin B receptor and Lamina-associated polypeptide 2) and on the other side with the chromatin-binding proteins at the nuclear periphery (e.g. Barrier-to-autointegration factor -BAF) (Hatch and Hetzer, 2014). Overall, these interactions form a stable network that strengthens the nuclear membrane and physically links the INM to the chromatin. The connections between the nucleus and the cytoskeleton are also pivotal for nuclear mechanics (Bustin and Misteli, 2016). Specifically, the LINC complex connects the INM with the ONM that faces the cytoplasm and is formed by two transmembrane proteins: KASH (Klarsicht, ANC-1, Syne homology; also known as nesprins) domain-containing proteins at the ONM and SUN (Sad1 and UNC-84) domain-containing proteins at the INM. Being on the ONM, Nesprins associate with the cytoskeleton (microtubules, actin, and intermediate filaments), whereas the SUN proteins interact with the nuclear lamina and lamina-associated proteins (Maurer and Lammerding, 2019). Through this complex of transmembrane proteins, mechanical forces are transferred from the actomyosin network to the NE and when this connection is perturbed cells may become insensitive to certain stimuli (e.g. tensile forces).

## 1.5.2 Nuclear mechanical properties in physiology and disease

Multiple pieces of evidence suggest that mechanical forces generated by the nucleus affect several cellular processes. Indeed, the nucleus, being the larger and stiffer organelle of the cell, if not able to adapt to external stimuli may limit the ability of cells to sustain mechanical stress. For this reason, the mechanical properties of the nucleus, determined by the viscoelastic genome and the nuclear envelope with the elastic peripheral nuclear lamina, are finely controlled within tissues.

For instance, it is known that chromatin contributes to determining nuclear size. In the absence of condensins, which physiologically promote chromosome compaction during mitosis, nuclear size increases in mammalian cells with relevant consequences. Specifically, mouse T cells, by failing to compact their nuclei, do not enter quiescence (Rawlings *et al.*, 2011). Another example is the presence of peripheral heterochromatin in the nucleus, which not only allows gene silencing but also provides structural robustness to withstand some of the mechanical insults that cells encounter in their tissue of origin or during migration (Bustin and Misteli, 2016). It has been shown that the overexpression of HMGN5 (High Mobility Group Nucleosome Binding Domain 5), an architectural chromatin protein, provokes chromatin decompaction and consequently decreases the overall rigidity of the nucleus (Furusawa *et al.*, 2015). Interestingly mice overexpressing HMGN5 develop hypertrophic hearts with cardiomyocytes having deformed nuclei and disrupted lamina. This last aberration is only in adult cardiomyocytes, in which the loss of chromatin compaction diminishes the ability of the nucleus to withstand the stress coming from the contraction of the heart. These data suggest that the interplay between heterochromatin and nuclear lamina arranges the maintenance of nuclear structure and elasticity (Furusawa *et al.*, 2015).

During processes such as cell migration, the nucleus need to counteract multiple sources of mechanical stress, since it must undergo considerable

structural changes to allow squeezing through the constrictions imposed by tissues or blood vessels. The nuclear lamina plays a key role in this process: cells overexpressing nuclear lamina present increased nuclear stiffness that lower the rate of cell migration, but at the same time decreased lamina levels reduce the viability of migrating cells, indicating the need for balancing in lamina abundance for a successful migration (Harada *et al.*, 2014). In another work, it is shown that nuclear movement during this process is facilitated by global chromatin condensation (Gerlitz and Bustin, 2010).

## 1.6 Mechanical cues

Tissues represent a dynamic landscape, in which cells are exposed to several numbers of mechanical inputs such as cell–cell and cell-Extra Cellular Matrix (ECM) adhesion, compression stress, interstitial fluid pressure, and shear stress. As an example, actomyosin contraction due to ECM stiffness causes tensile stress, whether the over-proliferation of cells in a confined space, very common in tumors' microenvironment, imposes compressive stress (Northcott *et al.*, 2018). The process through which cells sense and respond to mechanical cues is called mechanotransduction, and it is the mechanism that allows cells to convert mechanical stimuli into biochemical signals that affect cell morphology and function (Maurer and Lammerding, 2019).

## 1.6.1 Sensors and mediators of nuclear mechanotransduction

Nuclear mechanotransduction can be mediated by different key players, such as proteins that intervene in nucleo-cytoskeletal connections (LINC complex), nuclear envelope (NE), and peripheral lamina (LAMIN A/C), as well as the nuclear translocation of transcription regulators (YAP/TAZ). Interestingly, two independent works have shown recently that the nucleus can act as a ruler to measure cellular shape variations. It was

demonstrated that the nuclear envelope can sense cell deformation and that changes in its tension and folding activate a mechanotransduction pathway that controls actomyosin contractility and migration via a calcium-dependent phospholipase cPLA2 signaling (Lomakin *et al.*, 2020; Venturini *et al.*, 2020).

Lamins are also key contributors in mediating nuclear mechanotransduction. The nuclear lamina is a filamentous network of proteins that localize under the INM. It contains A-type lamins (Lamin A/C), present in specialized tissues, and B-type lamins (B1 and B2), ubiquitously expressed (Dechat *et al.*, 2008). Interestingly, while B-type lamins do not regulate nuclear mechanics, Lamin A/C expression correlates with tissue stiffness. Specifically, it is highly expressed in tissues that are subjected to high mechanical stress (e.g. bones and cartilage), but its expression is low in soft tissues that are not subjected to great mechanical stress, such as brain or adipose, with protein phosphorylation and turnover correlating inversely with matrix stiffness (Swift *et al.*, 2013). Lamin A/C function is to maintain nuclear structure, including its stiffness, and the organization of chromatin with which interacts such as the Lamin-associated domains (LADs) (Schoen *et al.*, 2017). Furthermore, A-type lamins are also involved in the regulation of cell differentiation and stemness in response to ECM stiffness. It has been demonstrated that in a soft matrix MSCs differentiation is promoted toward adipogenesis and that this process is associated with inhibited lamin A/C production. In contrast, lamin A/C overexpression in a stiff matrix enhances cell differentiation toward osteogenesis (Malashicheva and Perepelina, 2021). Furthermore, lamin A/C overexpression leads to the activation of stress-related proteins involved in cell differentiation, and of the transcriptional regulators YAP1 (yes-associated protein 1) and TAZ (Transcriptional coactivator with PDZ-binding motif) of the Hippo pathway, which promotes growth and regeneration (Swift *et al.*, 2013).

550    In particular, YAP and TAZ are conserved mechanotransducers able to respond to a vast number of different mechanical cues (e.g. shear stress,

552    ECM rigidity, and geometry). When they are mechanically activated, YAP and TAZ translocate from the cytoplasm to the nucleus where they can

554    interact with TEAD factors to regulate gene expression and activate cell-specific transcriptional programs (Panciera *et al.*, 2017). For example, in

556    cell differentiation, they have been reported to be excluded from the nucleus of MSCs placed in a soft matrix during adipogenesis and to be

558    instead functionally localized into the nucleus during osteogenesis. When cells perceive high mechanical inputs (e.g. cells on a rigid substrate,

560    stretched, plated at low density or in large adhesive area condition) YAP and TAZ are nuclear, while they remain evenly distributed at more

562    intermediate levels of mechanical stress (Panciera *et al.*, 2017).


564

## 1.7 Unbalance between Transcriptional and PcG in MSCs-based Kabuki Syndrome disease model

566    By investigating the effect of MLL4 LoF in MSCs we found that its haploinsufficiency impacted chromatin compartments, which show an unbalancing between

568    Transcriptional and PcG condensates (Fasciani *et al.*, 2020).

Indeed, MLL4 LoF impairs enhancer-associated cofactor clustering, causing a

570    decrease in the number and size of BRD4 and MED1 condensates (Figure 7A). Considering the known antagonism between the TrxG and PcG complexes, we

572    sought to investigate whether the MLL4 LoF-driven perturbation of Transcriptional condensates could affect PcG repressive compartments. Although the abundance of

574    Polycomb repressive complex 2 (PRC2) components was unaltered, analysis of Polycomb repressive complex 1 (PRC1) components revealed increased RING1B

576    (RING finger protein 1B) and BMI1 (B lymphoma Mo-MLV insertion region 1 homolog signals) protein clustering in MLL4 LoF condition (Figure 7B), even though
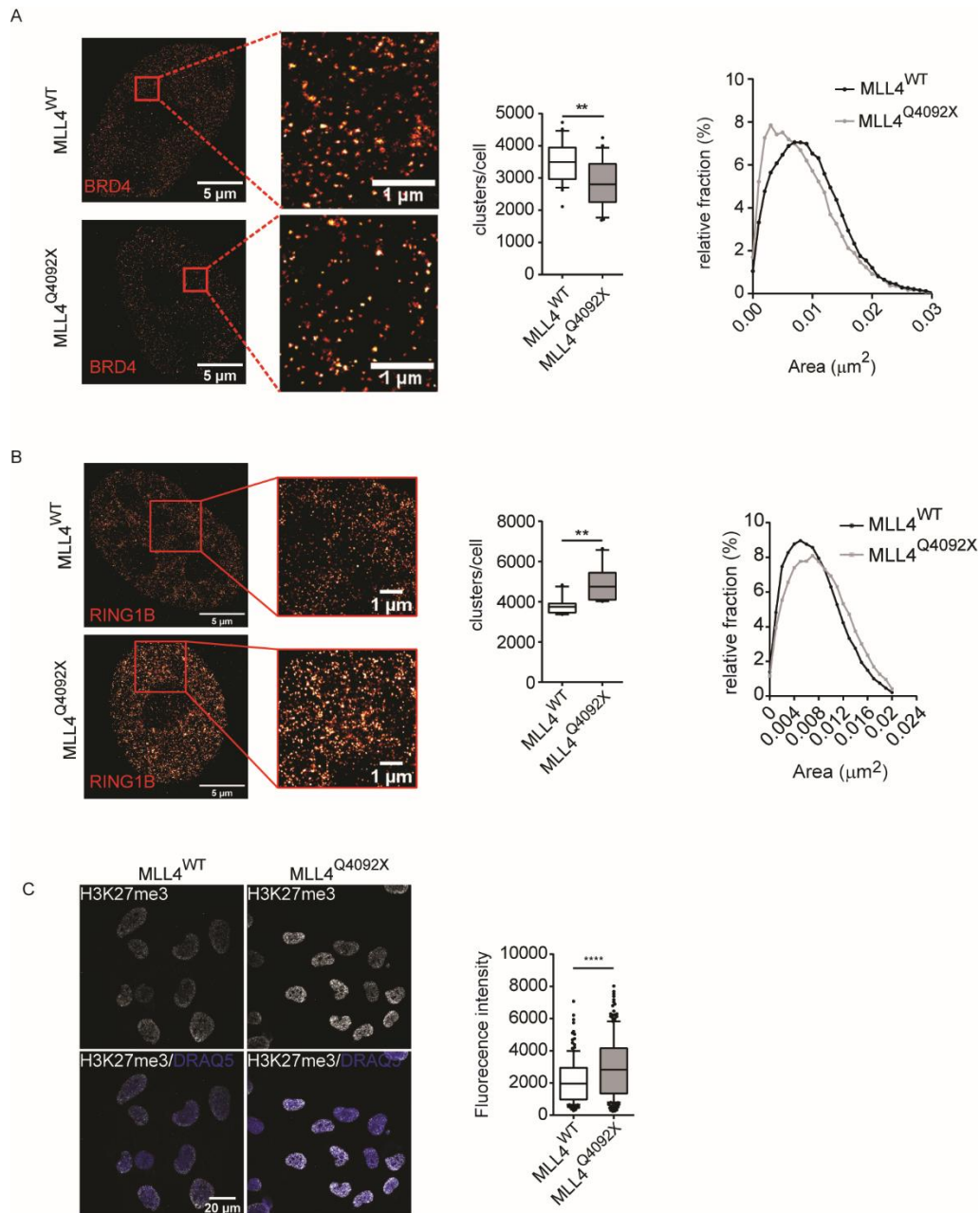
*Figure 7. Unbalancing between active (Transcriptional condensates) and repressive (PcG condensates) compartments in MLL4 LoF (MLL4$^{Q4092X}$). A and B) STORM images of Immunofluorescence staining against BRD4 (A) or RING1B (B) (on the left) with relative quantification of the number of clusters per nucleus and distribution of the area (on the right). Scale bars: 5µm for the right panel, 1µm for the left panel representing an enlargement of the previous image highlighting the distribution of the clusters. C) Confocal images of Immunofluorescence staining against H3K27me3 (gray) with nuclear quantification normalized on DRAQ5 signal intensity (blue). Scale bar 10µm. Modified from Fasciani et al., 2020.*

578    their transcripts levels were unaltered. The augmented level of PRC1 clustering is

also mirrored by increased deposition of H3K27me3, which is the histone

580    modification associated with PcG activity (Figure 7C).

By rescuing MLL4 protein expression via CRISPRa (CRISPR-mediated gene activation), we confirmed that the augmented PcG clustering and H3K27me3 deposition were dependent on MLL4 abundance.

Of note, the evidence that the transient re-establishment of MLL4 protein levels counteracted the augmented PcG clustering and H3K27me3 deposition indicates that MLL4 LoF affects repressive compartments, with increased PcG protein clustering.

## 1.7.1 Kabuki Syndrome is characterized by impairment of the mechano-response

Considering that chromatin compartments exert forces that shape nuclear structure, we further investigated the effects of MLL4 LoF on nuclear architecture. We noticed that MLL4 LoF MSCs presented an altered nuclear morphology with respect to the wild-type counterpart, with a reduction in the nuclear area, volume, and flatness (Figure 8A). This morphological phenotype was rescued in MLL4 LoF via CRISPRa re-establishment of MLL4 expression, suggesting that although MSCs were grown in standard culture conditions that allow force transmission to the nuclei, MLL4 LoF affects nuclear architecture. Knowing that the Lamin A/C level is modulated in response to changes in tensile forces, we tested its protein abundance in our model. We found that MLL4 LoF had reduced Lamin A/C levels when compared with WT cells, with an increased fraction of the protein being in the phosphorylated state, indicating an increased protein turnover (Figure 8B) (Fasciani *et al.*, 2020). Furthermore, the altered MLL4 LoF nuclear morphology leads to reduced nuclear localization of the mechanoeffectors YAP and TAZ.
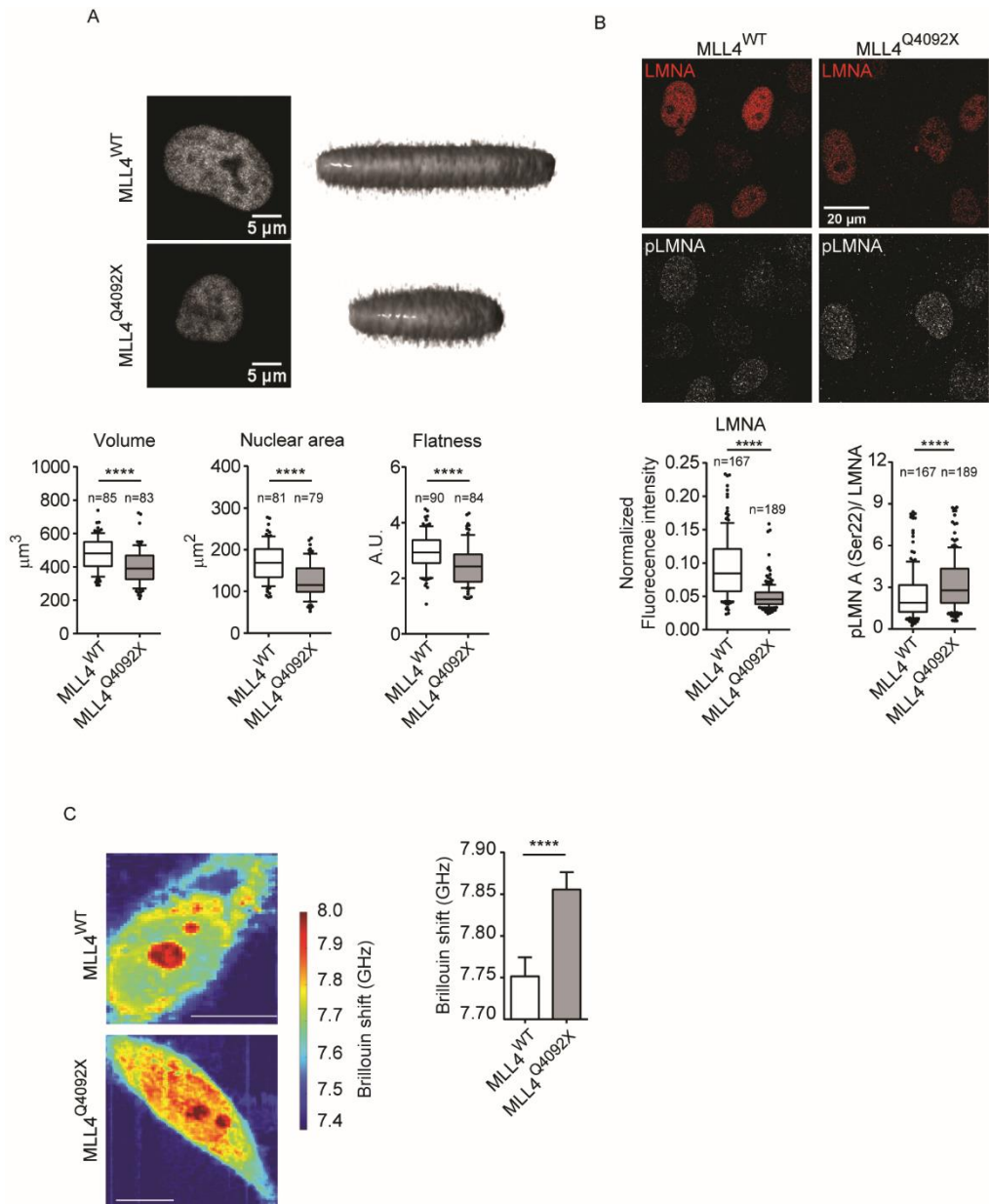
*Figure 8. Kabuki Syndrome is characterized by impairment of the mechano-response. A) Upper panel: on the left are depicted images of nuclei of WT and MLL4^Q4092X, scale bars, 5μm. On the left, reconstructed 3D images of the nuclear shape highlight nuclear volume and flatness. Lower panel: quantification of Nuclear Volume, Area, and Flatness. B) Upper panel: confocal images of Immunofluorescence of Lamin A -LMNA- and phLaminA on Ser22 - pLMNA(Ser22)- of WT and MLL4^Q4092X cells. Scale bar, 10μm. Lower panel: quantification of LMNA nuclear signal normalized on DRAQ5 signal (not shown), and ratio between pLMNA (Ser22) nuclear signal and LMNA. C) Left panel: maps of the stiffness distribution in WT and MLL4^Q4092X of images acquired with Brillouin microscopy. A higher Brillouin shift (GHz) corresponds to a higher stiffness in the cell. Scale bars, 10μm. Right panel: bar plot showing the quantification of the nuclear Brillouin shift. Fasciani et al., 2020.*

Overall, these results led us to hypothesize that MLL4 LoF resembles cells
that are under low-nuclear-stress conditions.

606

36

To further investigate nuclear mechanical properties, we took advantage of Brillouin microscopy to measure nuclear stiffness, which can be determined by quantifying the longitudinal elastic modulus calculated on the base of the Brillouin frequency shift (Antonacci *et al.*, 2018). The increased Brillouin shift in MLL4 LoF indicated that these cells were characterized by increased nuclear stiffness with respect to WT cells (Figure 8C) (Fasciani *et al.*, 2020).

To test whether the altered nuclear morphology observed was dependent by the increased PcG-clustering driven by MLL4 haploinsufficiency, we rescued PcG abundance in MLL4 LoF by overexpressing histone H3.3 harboring a mutation of lysine 27 (K27) to methionine in the N-terminal tail (H3.3K27M), which is known to have a dominant negative effect on PcG activity (Lewis *et al.*, 2013). As expected, H3.3K27M overexpression reduced BMI1 and RING1B protein abundance as well as H3K27me3 levels in MLL4 LoF MSCs. Interestingly, PcG rescue re-established nuclear architecture parameters such as nuclear volume, area, flatness as well as lamin A/C protein abundance and nuclear stiffness in MLL4 LoF MSCs.

To investigate the relevance of these results in the context of the pathology, we assessed whether MLL4 LoF affects MSCs mechanoresponsiveness during differentiation, finding that MLL4 LoF commitment towards chondrocytes was strongly affected, while osteogenesis was mildly impaired. Interestingly, by releasing the nuclear mechanical stress through inhibition of the nuclear mechanosensor ataxia telangiectasia and Rad3-related protein (ATR), we re-established the mechanosignaling of MSCs. Specifically, the treatment with the ATR-inhibitor restored YAP/TAZ nuclear localization in MLL4 LoF, as well as MSCs commitments toward chondrocytes and osteocytes. Furthermore, blocking ATR in an *in vivo* Kabuki syndrome model developed in medaka fish, restored the observed chondrogenic and skeletal defects, rescuing proper head morphogenesis without evidence of toxicity.

Altogether these results indicate that MLL4 is necessary for preserving nuclear mechanical properties and that its haploinsufficiency leads to an increased PcG clustering which strongly affects nuclear structure and mechanoresponse. Of importance, inhibiting ATR could represent a novel therapeutic option for restoring nuclear mechanical properties and cell mechanoresponsiveness.

## 1.8 Nuclear phase separation in mechanobiology

LLPS has recently been demonstrated to be a crucial organizing principle for the cell, resulting in the formation of membraneless compartments that work as organizational hubs, sequestration centers, or reaction accelerators (Alberti, 2017). Within the nucleus, several aspects of gene expression appear to be facilitated by multiple condensates, including repressive heterochromatin foci and the super-enhancers (Strom *et al.*, 2017; Sabari *et al.*, 2018; Sanulli *et al.*, 2019). Although the role of biomolecular condensates in the regulation of the "genetic" functions of the genome (e.g. gene transcription) has been investigated, their connection with the non-genetic functions of the genome still remains elusive. Indeed, even if multiple studies suggest that they structurally shape chromatin compartments, little is known about how they contribute to the regulation of nuclear mechanical properties. However, it is reasonable to think that if they have a role in shaping chromatin domains, which in turn affect nuclear mechanics, they are likely to be one of the structural elements of mechanobiology. Of note, in Fasciani *et al.*, we demonstrated the existence of a connection between the unbalancing of nuclear condensates and nuclear mechanics in Kabuki Syndrome, even though we did not further investigate this aspect and other studies will be required to clarify their interplay in the regulation of biological processes.

## 2. Aim of the thesis

The main aim of this thesis was to investigate the role of nuclear condensates, specifically Transcriptional and PcG condensates, in regulating the response of the nucleus to mechanical stimuli. Our hypothesis is that different sources of mechanical stress may impinge on the nuclear structure affecting the re-organization of chromatin biomolecular condensates.

Considering that our recent findings highlighted a functional connection between defects on chromatin compartments and nuclear mechanics in Kabuki Syndrome, we hypothesized that nuclear condensates could be key factors in tuning nuclear responses to external stimuli. Therefore, we tested the response of Transcriptional and PcG condensates to different mechano-physical conditions, with the idea that cells can exploit the synergy and efficiency of the process of phase separation for cellular sensing, as well as the sensibility and the velocity of condensates formation, occurring in a timescale of seconds. This timespan would also be compatible with a mechano-response, ensuring an adaptive and fast response for survival under stressful conditions.

First, in order to characterize the phase separation behavior of MLL4 in MLL4$^{WT}$ MSCs and MLL4$^{LoF}$ MSCs, we used a Halo-Tag- based optogenetic tool to control the spatio-temporal assembly of condensates. Second, we registered the response of biomolecular condensates in MLL4$^{WT}$ MSCs and MLL4$^{LoF}$ MSCs at different substrate stiffness, both at the steady state and by stimulating MLL4 condensates in living cells.

Last, we sought to assess the effect of MLL4 haploinsufficiency on nuclear deformation capacity, cell migration, and survival rate by taking advantage of two devices: microchannels with restrictions of different widths and static confinement.

# 3. Materials and methods

## 3.1 Cell lines and cell culture conditions

690

All the experiments were carried out using hTERT-immortalized human adipose-derived MSCs (a gift from P. Tatrai). MSCs were cultured in 1:1 DMEM/F-12 medium (Gibco; 11320-074) supplemented with 10% fetal bovine serum (Euroclone; ECS0180L) and 100 U/mL Penicillin/Streptomycin (Gibco; 15140122). Cells were maintained at 37°C under 5% $CO_2$.

696

### 3.1.1 Generation of stable cell lines

698       $MLL4^{Q4092X}$ and $MLL4^{P4093X}$ ($MLL4^{LoF\_1}$ and $MLL4^{LoF\_2}$ respectively) carrying frameshift mutation in the exon 39 of KMT2D were generated and genome edited via CRISPR–Cas9 by Alessandra Fasciani as described in Fasciani *et al.*, 2020.

MSCs expressing pTRIP-SFFV-EGFP-NLS, pCDH-MiniNesprin1-GFP, pCDH-MiniNesprin1-GFP-cpstFRET, pCDH–EF1–MCS–IRES–PURO–H3.3K27M, PGK-H2B-mCherry and PGK-H2B-eGFP were obtained transducing with the corresponding lentiviral vector. For the FLIM-FRET experiments, after co-transduction with PGK-H2B-mCherry and PGK-H2B-eGFP, positive cells were sorted at single cell with FACS Aria IIu (BD Bioscience) in MW96 for single clone generation.

MSCs expressing piggyBAC-MLL4-PrLD-HaloTag-Cry2 were obtained by co-nucleofecting 50.000 cells with piggyBAC-MLL4-PrLD-HALOtag-Cry2 (1µg) and pCMV- Pbase (0.2µg) using P1 Primary Cell 4D-NucleofectorTM X Kit L (Lonza; V4XP-1024) Amaxa Nucleofector (program FF104, Lonza) following manufacturer's instructions.

## 3.2 DNA constructs

714

For the in vitro droplet formation assay (phase separation experiments) the pET-mCherry-MLL4-PrLD/ PrLD-ΔQ was subcloned from pET-mCherry-MED1-IDR, a gift from Richard A. Young laboratory. The MLL4 PrLD region (from amino acid 3560 to 4270) was amplified by PCR (oligonucleotides: FW_GCCAGATCTGGTGATGCTGAGAAGCTCAAGCT; RV_GCCGTCGACTTTACTGTGGTCCAGGGAAGCC) and cloned between the BglII and SalI sites in the pET mCherry-MED1 IDR, while the MLL4 PrLD ΔQ region was obtained by overlap-extension PCR and cloned between the BglII and SalI sites in the pET-mCherry-MED1-IDR (oligonucleotides: FW_GCTCAGCCCATGGGCTCTTTTTTTAAACCAGAGTCGAACTTTACTGTCTC; RV_TAAAGAGCCCATGGGCTGAGCGCTCAGTT). For the optogenetic experiments, the construct piggyBAC-MLL4-PrLD-HaloTag-Cry2 was cloned by Lisa Fol as follows: the HaloTag sequence was PCR amplified (oligonucleotides: FW_GCCGCTAGCATGGCAGAAATCGGTACTGG; RV_GCCACGCGTGCCGGAAATCTCGAGCG) with the restriction sites for NheI and MluI. The fragment was then cloned in the piggyBAC mCherry-MLL4-PrLD-Cry2 (Fasciani *et al.*, 2020) between the NheI/MluI sites. For the generation of the stable cell line pCMV- Pbase (PiggyBac transposase), donated from Luca Tiberi laboratory, was also used.

For the FLIM-FRET experiments the plasmids PGK-H2B-mCherry and PGK-H2B-eGFP were used (Addgene plasmid #21217 and #21210).

The plasmid used to generate the stable cell lines for assessing Nuclear Envelope rupture inside microchannels with restrictions was pTRIP-SFFV-EGFP-NLS, purchased on Addgene (#86677).

The lentiviral vectors pCDH-MiniNesprin1-GFP for Nesprin overexpression and pCDH-MiniNesprin1-GFP-cpstFRET for studying Nuclear Envelope tension were kindly gifted from Paolo Maiuri laboratory.

The construct for performing PcG rescue on MLL4[LoF] MSCs, pCDH–EF1–MCS–IRES–PURO–H3.3K27M, was gifted from the Allis laboratory.

## 3.3 Immunofluorescence

746    MSCs were seeded at a density of 7.500 cells/ cm$^2$ (low density condition) or 15.000

cells/ cm$^2$ on coverslips coated with 0.1% gelatin (Sigma–Aldrich; G1393). Cells were

748    fixed after 48h with 4% paraformaldehyde for 10min at room temperature (RT),

washed three times with phosphate-buffered saline (PBS), and then processed as

750    follows: permeabilization and blocking with PBS/ 1% bovine serum albumin

(Millipore; 126579)/ 5% goat serum (Fisher Scientific; 11475055)/ 0.5% Triton X-100

752    (blocking solution) for 1h at room temperature, incubation with primary antibody

diluted in the blocking solution for 2h at room temperature or overnight at 4°C,

754    washes in PBS and incubation with secondary antibodies (Alexa Fluor conjugated

produced in goat by Thermo Fisher), diluted in the blocking solution, and DAPI

756    (Sigma–Aldrich; D9542) for nuclear staining for 1h at RT.

The primary antibody used and dilutions are listed below: BRD4 (abcam; ab128874)

758    1:200, BMI1 (Millipore; 05-637) 1:100, RING1B (Cell Signaling; 5694) 1:200,

phospho-Lamin A/C (Ser22) (Cell Signaling; 13448) 1:100, H4K16ac (Millipore; 06-

760    762) 1:200, YAP/TAZ (Cell Signaling; 8418) 1:100, H3K27me3 (Millipore; 07-449)

1:100, Lamin A/C (Abcam; ab40567) 1:200, KMT2D (Invitrogen; 701869) 1:200,

762    Vinculin (Sigma–Aldrich; V9264) 1:200.

Coverslips were mounted on glass slides using ProLong Gold (Invitrogen; P36934).

764    Images were acquired using a Leica TCS SP8 confocal microscope with a HCX Plan

Apo ×63/1.40 objective. When needed (nuclear volume and flatness quantification),

766    z stacks were acquired with sections of 0.5 μm. Image acquisition settings were kept

constant for downstream image analysis.

768

### 3.3.1 Image analysis

Images acquired by confocal were analyzed using ImageJ (FIJI) software.

770    For 2D analysis, the DAPI signal was used to define the ROI (region of

interest) of the nucleus. To measure the nuclear mean intensity and area,

772    LIF files were firstly converted to TIFF composite images, then the

minimum value of the threshold and the size range parameters were

774     determined for each independent experiment to identify the nuclei on the

binary image.

776     For the measure of nuclear volume and flatness, a 3D analysis was performed by using the 3D plugin suite (ImageJ plugin) and segmenting the

778     nuclei on the DAPI signal.

For measuring cluster size, mean intensity, and area in 2D the analysis was

780     performed in ImageJ as follows: first, background subtraction was applied (rolling ball correction), then unsharp masking and median filters were

782     applied. The clusters were finally identified with the Shanbhag dark automatic threshold.

784     To quantify the nuclear to cytosolic localization of YAP/TAZ, a MATLAB routine deposited in GitHub

786     (https://github.com/SZambranoS/RoutinesNucCytoYAP) was used. In brief, images of the DAPI and YAP/TAZ channels were saved as 16-bit TIFF

788     files. Nuclei were segmented on the basis of the DAPI signal, after choosing the correct physical parameters (e.g. area). A ring of 30-pixel width around

790     each segmented nuclei was found to calculate the YAP/TAZ cytosolic fraction. Lastly, the nuclear to cytosolic intensity was calculated as the

792     ratio of the nuclear and cytosolic average YAP/TAZ intensities.

For calculating nuclear envelope (NE) invaginations, the perimeter was

794     measured by quantifying the Nesprin-GFP nuclear signal.


## 3.4 Protein extraction and Western Blot (WB) analysis

796

For histones and histone modifications, acid extracts were obtained with the

798 following procedure: cells were washed twice with cold PBS, harvested in 1 ml of

cold PBS, and centrifuged for 5 minutes at 1500 rpm. Pellet was resuspended in the

800 histone extraction buffer (10mM Hepes pH 8, 10mM KCl, 0,1mM MgCl2, 0,1mM

EDTA pH 8, 2mM PMSF, 0,1mM DTT) to achieve a concentration of $10^7$ cells/ml. Cells

802 were left at 4°C for 10 minutes and then centrifuged for 10 minutes at 5000 rpm at

4°C. The supernatant, corresponding to cytosolic extract, was discarded and the pellet was resuspended in 0,2N HCl (4x10$^7$ cells/ml) and left O/N at 4°C on the rotating wheel. Proteins were then recovered by centrifugation for 10 minutes at 4000rpm at 4°C, and supernatant, containing histones protein, was quantified to measure protein concentration by Bradford assay (Biorad; 5000006) according to manufacturer's instructions.

For western blots analysis, 2, 8 or 15µg of protein samples were subjected to SDS-PAGE in a gradient gel (NuPAGE™ 4 to 12%, Bis-Tris, Invitrogen; NP0322BOX) runned in MES Buffer (Invitrogen; NP0002). Proteins were transferred to a nitrocellulose membrane, that was subsequently blocked in PBS-Tween containing 5% milk for one hour at RT in agitation and incubated with primary antibody O/N at 4 °C keeping the membrane in motion. The membrane was then washed three times with PBS-Tween for 5 min and incubated with HRP- conjugated secondary antibody for one hour at RT. The chemiluminescent signal was captured, after incubation with ECL reagents (GE Healthcare; RPN2232), using ChemiDoc XRS+ System (Bio-Rad). When needed, relative optical density was quantified with FIJI (http://fiji.sc/). Primary antibodies with corresponding dilution used and specific amount of protein loaded for each antibody are the following: H2B (Abcam; ab1790) 1:5000 (8µg), H3 (Cell Signaling; 9715) 1:1000 (2 µg), H3k27me3 (Millipore; 07-449) 1:500 (15µg), mCherry (Abcam; AMab167453) 1:1000 (2 µg), GFP (Santa Cruz; sc-9996) 1:200 (2 µg).


## 3.5 Recombinant Protein Purification

The Protein purification was performed as follows: bacterial pellet (BL21(DE3)pLysS bacterial strain) was resuspended in 25mL of Ni-NTA Lysis Buffer (NiNTA LB) (50 mM TrisHCl pH 7.5, 500mM NaCl), and sonicated. The lysate was centrifugated at 12,000g for 20 minutes at 4°C and added to Ni-NT Agarose (Qiagen; 30210) pre-equilibrated with Ni-NTA LB. Falcon containing the agarose and the lysate was rotated at 4°C for 1 hour, then agarose beads were collected by centrifugation for 5 min at 200 g and were transferred to the gravity column. The beads associated with the protein of interest were firstly washed with the NiNTA LB containing 10mM

Imidazole. Afterward, the protein was eluted with Ni-NTA LB containing 50/100/250 mM imidazole. Eluates were cleared of non-specific proteins by taking advantage of gel filtration chromatography (Superdex 200 Increase 10/300 GL, GE Healthcare; 28990944) and equilibrated with Buffer D (50mM Tris-HCl pH 7.5, 125mM NaCl, 1mM DTT, 10% glycerol).

Fractions containing the protein of interest were pooled and concentrated using Pierce™ Protein Concentrator PES, 10K MWCO (Thermo Scientific; 88527). The quality of eluted fractions was finally analyzed by Coomassie stained gel.

## 3.6 Droplet- formation Assay

The recombinant protein was added to Buffer D containing 10% Polyethylene glycol (PEG) 8000 (Sigma; 1546605) at varying protein, final NaCl, and 1.6- hexanediol (Santa Cruz; sc-237791) concentrations. Protein in Buffer D was spotted on a glass slide and covered with a coverslip. The solution was left at RT for 5 minutes and the formed droplets were acquired using a Zeiss Axio Observer inverted microscope with an AxioCam 503 mono D camera and a Plan-Apochromatic 100x/1.4 oil-immersion objective equipped with a prism for DIC (Zeiss).

Images were analyzed with FIJI. The intensity of the signal inside and outside the droplets was determined by setting a threshold on the base of the minimum intensity seen at the lower concentration tested in which droplets were present. This threshold was kept constant in every other condition. The saturation concentration was quantified as specified in previous work (Wang *et al.*, 2018). The fluorescence intensity was measured inside (Idroplet) and outside (Imedia) the droplets. The amount of condensed protein was defined by the ratio of Idroplet to Imedia. If no droplets were present, the ratio was set to zero.

## 3.7 Migration Assay

20.000 cells/ cm$^2$ were plated in a medium deprived of growth factors and placed onto collagen-coated (PureCol® Type I Collagen Solution, Advanced Biomatrix; 5005)

862 transwells with polycarbonate membrane harboring pores of different size: 8μm (Corning; 3422), 5μm (Corning; 3421) and 12μm (Cell Biolabs Inc.; CBA-107). The

864 medium, complete with growth factors, was added at the bottom of the transwell as a chemo-attractant. After 8 and 24h samples were fixed in 4% PFA as previously

866 described. The upper part of the transwell was cleaned with a cotton swab to facilitate imaging at SP8 Confocal Microscope. After that, DAPI staining was

868 performed as previously described and membranes were mounted on coverslips and acquired at SP8 Confocal Microscope with a 40X objective. The percentage of

870 migrated cells was calculated by counting the number of migrated cells (on the bottom of the membrane) over the number of seeded cells.

872

## 3.8 Plates at different substrate stiffness

874 For assessing the effect of different substrate stiffness on MSCs, CytoSoft® Imaging 24-well Plates (Advanced Biomatrix; 5188-1EA) of 0.5, 8 and 32kPa were used. Plates

876 were washed three times with PBS and then coated with 10 μg/μl fibronectin (Santa Cruz; sc-29011) for 1h at RT. Cells were plated with a density of 7.500 cells/ $cm^2$ (low

878 density condition) or 15.000 cells/ $cm^2$, grown for 48h and fixed with 4% PFA. Immunostaining was performed directly on the plates, then samples were acquired

880 at SP8 Confocal Microscope and analyzed as previously described.

## 3.9 Microchannels with restrictions

882

We used for this assay a 35mm Petri dish which contains a set of molded

884 microchannels, with variable dimensions and restrictions, where cells can migrate within (4DCell; MC011, MC019). Microchannel dishes were washed three times with

886 PBS for 5 minutes. The last washing was replaced in each chamber by 10μl of 10μg/μl fibronectinImage analysis and single-cell tracking and incubated for 1h at RT. After

888 the coating, the device was washed again three times with PBS, and cell culture medium containing 2% FBS was added to cover each chamber and left for 15

890 minutes at 37°C. Then, a droplet of cell solution (100.000 cells/10μl) in 2% FBS-

containing medium was added to each access port and kept again for 30 minutes at 37°C before adding another 2ml of 2% FBS culture medium. Cells were grown for 48h. 6 hours before live imaging a gradient of FBS was created by adding a droplet of 10% FBS- containing medium in the access port closest to where the cells have been plated and with whom they communicate. Finally, 10% FBS- containing medium was added to fill each chamber and Time-lapse video microscopy was performed at 37°C and 5% $CO_2$ using the Nikon Eclipse Ti2 with an ×20/ 0.75 or 60x/ 1.4 Oil Plan Apo λ objective (Nikon) integrated with a Lumencor SpectraX LED light source system and a EMCCD sensor camera (Andor iXon Ultra 888) for the detection. Images were acquired every 5 minutes for at least 12h. Image analysis and single-cell tracking were performed using the NIS software. Specifically, the time of residence (time of migration) was calculated by counting how many frames cells take to pass through the restrictions ($t_1$ = first frame in which a protrusion of the cell in the restriction is visible, $t_{final}$ = first frame in which the cell is out of the restriction). Nuclear Envelope Rupture was quantified on the basis of the NLS-GFP signal as described in previous work (Raab *et al.*, 2016). For measuring the NLS-GFP Intensity in the cytoplasm and nucleoplasm, a small ROI was put in front of the nucleus at each time frame in which the nucleus enters and passes through the restriction (ROI corresponding to the cytoplasm). The average intensity of the ROI of the cytoplasm was divided by the average intensity of the nuclear NLS-GFP signal before the nucleus entered the constriction (Cytoplasm/Nucleoplasm ratio) or vice-versa (Nucleoplasm/Cytoplasm ratio). The percentage of rupture was calculated as the ratio between the number of cells undergoing nuclear envelope rupture and the number of cells passing through the constriction. The percentage of cell death was measured by calculating the ratio between the number of cells dying while passing through the restriction and the total number of cells passing through the constriction.

## 3.10 Cell confinement

920      In order to confine cells at 3 and 6 μm the CSOW 620 – static confiner (4DCell) was used. The height of confinement is controlled by polydimethylsiloxane (PDMS)

922      micropillars, fabricated in a glass slide and attached to a PDMS piston. The confiner was handled and assembled following 4DCell instructions. Pistons and confinement

924      slides were equilibrated for 1h at 37°C in the culture medium before performing the imaging. To ensure cell adherence, the glass bottom 6-well plate provided with the

926      confiner was coated with 10 μg/μl fibronectin for 1h at RT.

20.000 cells were plated in the central circular part of the well and after 24h were

928      confined by placing the confiner lid on top of the well. Imaging was performed at the Nikon Eclipse Ti2 with an ×20/ 0.75 Plan Apo λ objective (Nikon) at controlled

930      temperature and $CO_2$. Images were taken after at least 20 minutes of confinement and after that every 5 minutes for 12h.

932

## 3.11     FLIM- FRET

934      Förster resonance energy transfer (FRET)–based assay using multiphoton fluorescence lifetime imaging microscopy (FLIM) was carried out on MSCs clones

936      expressing GFP-H2B (donor alone) and 2FPs-H2B (FRET pairs; donor and acceptor: GFP-H2B and mCherry-H2B) at 37°C and 5% $CO_2$, plated at a density of 20.000 cells/

938      $cm^2$ either in a classic petri dish or in CytoSoft® Imaging 24-well Plates. FLIM was performed using an inverted laser scanning multiphoton LSM780 microscope (Zeiss)

940      with a 40× Plan-Apochromat objective NA 1.3 (Zeiss). Two-photon excitation was performed using Chameleon Ultra II laser at 890 nm. The HPM-100 module

942      (Hamamatsu R10467-40 GaAsP hybrid photomultiplier tube) allowed the detection of the emitted photons. The fluorescence lifetime imaging was achieved by time-

944      correlated single-photon counting (TCSPC) electronics (SPC-830; Becker & Hickl), which measures the time elapsed between laser pulses and the fluorescence

946      photons. During acquisition, the laser power was adjusted to provide a mean photon count rate of about $10^5$ photons per second. FLIM measurements were acquired

948      over 90 s, and fluorescence lifetimes were quantified and calculated for all pixels in each cell by selecting specific ROI by using SPCImage software (Becker & Hickl). The

950    FRET efficiency was measured by comparing the FLIM values obtained for cells expressing the GFP donor fluorophore alone with the complete FRET pairs. The FRET

952    efficiency was calculated as "E FRET= 1- ($\tau_1$ / $\tau_2$)", where $\tau_1$ is the mean fluorescence lifetime of the donor in the presence of the acceptor in 2FPs-H2B MSCs, and $\tau_2$ is the

954    mean fluorescence lifetime of the donor expressed in GFP-H2B cells. In the non-FRET conditions, the mean fluorescence lifetime value of the donor was calculated

956    from a mean of the $\tau_2$ by applying a mono-exponential decay model to fit the fluorescence lifetime decays. In the FRET conditions, a bi-exponential fluorescence

958    decay model to fit the experimental decay curves was applied. By fixing the non-interacting proteins' lifetime $\tau_2$, we could estimate the $\tau_1$ value with the SPCImage

960    software.


## 3.12    Nuclear Envelope FRET sensor

962

       MSCs expressing pCDH-MiniNesprin1-GFP-cpstFRET were seeded at a density of

964    20.000 cells/ cm$^2$ in an IBIDI plate (82426) and stained with 1:1000 SirDNA (Spirochrome; SC007), a nuclear dye compatible with live imaging. Cells were

966    acquired using Leica TCS SP8 confocal microscope with a HCX Plan Apo ×63/1.40 objective. Donor (cpCerulean) was excited at 458 nm and emission peaks of

968    cpCerulean and cpVenus were captured, respectively, in a window of 470-490nm and 520-540nm. The inverted FRET index was calculated as the ratio between

970    cpCerulean and cpVenus mean intensity. Data were analyzed using the SirDNA channel to define nuclear ROI as described in section 3.3.1.

972

## 3.13    Optogenetics experiments

974    To allow the visualization of the MLL4-PrLD protein, MSCs expressing piggyBAC-MLL4-PrLD-HaloTag-Cry2 were stained with 200nM of 646 Janelia Fluor® HaloTag®

976    (Promega; GA1120) diluted in complete culture medium for 20 minutes at 37°C. The substrate was then quickly washed once in PBS before replacing the medium.

978      The time-lapse video was carried out continuously for the indicated timings at 37 °C

and 5% $CO_2$ using the Nikon Eclipse Ti2 with a Plan Apo 100x/1.45 Oil objective

980      implemented with a EMCCD or CMOS sensor camera (Andor). Images of fluorescent

cells were acquired before and after the stimulus (blue-light activation with LED 470

982      100% intensity for 3 seconds) as indicated in the figures, and quantified to obtain

the number, area, and mean intensity of clusters as follows: maximum intensity

984      projection in z was performed (z-step size of 0.5 μm), then the ROI was drawn on the

basis of the HaloTag 646 fluorescent intensity signal on the pre-stimulus condition.

986      After background subtraction, in which the rolling ball correction was kept constant

for every experiment, the following threshold was used to identify clusters: "(mean

988      intensity of the nucleus on the pre-stimulus) + (4X standard deviation)". This allows

to take into account variations in the expression of the protein before the stimulus

990      at the single- cell level. The function "Find Maxima" with a prominence of 20 was

used to further define the clusters.

992      We also state that we noticed variability in terms of cluster number and size by

acquiring with the two different hardware settings, although the differences and the

994      trend among samples are preserved. Indeed, the two cameras used have different

sensitivity, characteristics, and pixel sizes that could influence cluster analysis. In

996      particular, the sCMOS Andor Zyla 4.2 PLUS has a pixel size of 6.5 μm x 6.5 μm,

whereas the EMCCD sensor Andor iXon Ultra 888 has a pixel size of 13 μm x 13 μm.

998

### 3.14     Cell cycle assay

1000     MSCs were harvested, washed in PBS, and fixed in 70% ice-cold ethanol for 30

minutes at 4°C. After another wash in PBS, the pellet was resuspended in the

1002     propidium iodide (PI) staining solution, containing 3.8 mM sodium citrate, 100 μg/

ml RNase, and 50 μg/ ml PI (Thermo Scientific; J66764.MC), in order to obtain $10^6$

1004     cells/ml. Cells were incubated for 40 minutes at RT and then acquired at the Flow

Cytometer FACS CantoA recording at least 10.000 events and analyzed with the Flow

1006     Jo software (Cell Cycle platform).

## 3.15    Statistical Analysis

All experiments were performed on independent biological replicates, as specified in the results section. For the imaging data, images were acquired by random sampling by acquiring at least 15 non-overlapping fields of view, and, unless differently specified, one representative replicate is shown, even though the experiment was performed at least three times independently obtaining similar results. The exact statistical parameters used for each experiment are reported in figure captions. The statistical tests performed are two-tailed or one-tailed unpaired Student's t-test, one-way ANOVA for multiple comparisons. P-values are indicated in the figures and the corresponding figure captions as: *= $p<0.05$, **= $p<0.01$, ***= $p<0.001$, ****= $p<0.00001$, ns = not significant ($p<0.05$).

# 4. Results

In this section, I present the results obtained during my PhD, which have been carried out in the Laboratory of Chromatin Biology and Epigenetics led by Prof. Alessio Zippo at the Department of Cellular, Computational and Integrative Biology (CIBIO, University of Trento). The majority of the results shown below are unpublished, however, paragraph 4.1 contains results obtained by myself and published on Nature Genetics in 2020 (Fasciani *et al.*, 2020), of which I share the co-first authorships. My contribution to this publication was to perform the phase separation and immunofluorescence experiments and participate in data analyses. Part of these results has been mentioned in the introduction of this thesis.

Furthermore, since this project required a multidisciplinary approach encompassing molecular biology, cell biology, microscopy, physics, and material science, some of the experiments and data analyses were performed in collaboration with other laboratories having the expertise needed for a specific application: FLIM-FRET experiments and analyses were carried out in tight collaboration with David Llères from Dr. Robert Feil laboratory at the Institute of Molecular Genetics of Montpellier. Brillouin microscopy imaging and data analysis were performed by Claudia Testi from Prof. Ruocco laboratory at the Italian Institute of Technology of Rome. These research activities included also my onsite visit during which I applied FLIM-FRET and Brillouin Microscopy to assess the level of chromatin compaction and nuclear stiffness, respectively, in our model. We also thank Paolo Maiuri (AIRC Institute of Molecular Oncology, Milan) and his collaborators Alessandro Poli and Fabrizio Pennacchio for scientific discussions and help with the nuclear envelope tension experiments and cluster dynamics data analysis.

## 4.1 MLL4 undergoes Phase Separation in vitro

The evidence that within cells MLL4 protein presents a puncta-like distribution (clusters), typical of proteins that participate in nuclear condensates, led us to hypothesize that the MLL4–COMPASS complex could be organized in biomolecular condensates (Fasciani *et al.*, 2020).

Indeed, super-resolution microscopy (STORM) of the endogenous MLL4 protein in MSCs showed that it is organized in heterogeneous clusters with variable size, similar to what has been detected for BRD4 and RNA Pol II proteins. For these reasons, we sought to investigate the ability of MLL4 to undergo phase separation.

### 4.1.1 In silico analysis of IDRs

The presence of IDRs in protein amino acids sequence is known to be predictive of whether a protein will likely phase separate. In order to study the features of the amino acids sequence of MLL4 and search for the presence of IDRs we used the tool PONDR (predictor of natural disordered regions, http://www.pondr.com/). The in silico analysis performed with PONDR recognized 4473 disordered residues out of 5537, with an overall percentage of disorder of 80.78. Figure 9 showed the output of the analysis, which highlights the presence of three major IDRs with a percentage of disorder above the PONDR score (black line): segment [353]-[1363] (IDR1), segment [2055]-[3415] (IDR2), segment [3532]-[4461] (IDR3). Analysis by PLAAC (Prion-Like Amino Acid Composition) indicated that this last region contained a prion-like domain (PrLD) characterized by a PolyQ stretch of 78 amino acids (Figure 9) (Fasciani *et al.*, 2020). PrLDs are often found in RNA-binding proteins that drive protein aggregation in neurodegenerative disorders such as amyotrophic lateral sclerosis. They contain low-complexity regions composed of stretches of polar amino acids that favor the nucleation of macromolecular assemblies by promoting multivalent interactions (Alberti, 2017).

Overall, this analysis suggests that MLL4 may sustain the formation of phase-separated droplets.

To understand whether the peculiar features of IDR3 (hereinafter referred to as MLL4 PrLD) were able to drive MLL4 phase separation, we sought to purify this domain (from amino acid 3560 to 4270) fused to the mCherry

fluorescent protein, containing or deprived of the polyQ region (MLL4 PrLD

1080 ΔQ) and assess their ability to form droplets by in vitro droplet formation

assay.
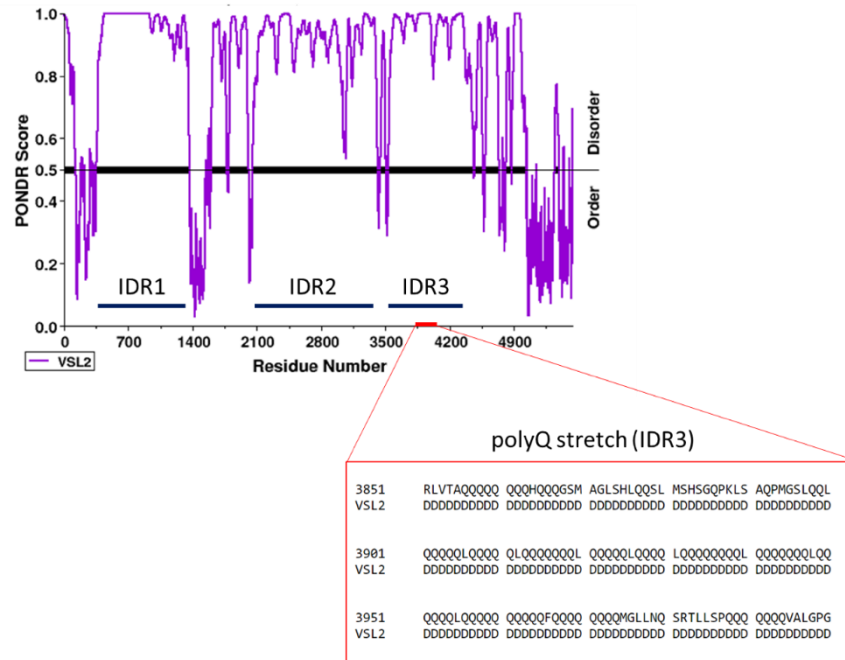


1082

*Figure 9. Representation of the predicted MLL4 IDRs retrieved by PONDR analysis. The*
*image shows The PONDR score for each amino acid residue of human MLL4 protein.*
*MLL4 IDRs (IDR1, IDR2, and IDR3) that have a percentage of disorder above the*
*PONDR score (black bolded line) are highlighted with a blue line. The red square is a*
*zoom-in of the polyQ stretch contained in IDR3. The presence of the letter "D" below*
*the amino acids sequence indicates that the region has been predicted by VSL2 to be*
*disordered.*

### 4.1.2  Protein purification and Gel Filtration

To purify mCherry-MLL4 $_{PrLD\ /\Delta Q}$ recombinant proteins we used Ni-NTA

1084 affinity chromatography, which allows exploiting the binding of the

polyhistidine-tag (His-Tag), placed at the N-terminus of the protein's

1086 sequence, with Nickel-containing Ni-NTA resin. To purify the protein, the

resin was exposed to increasing concentrations of imidazole, a competitive

1088 agent for the elution of histidine-tagged proteins. After purification, the

eluted fractions were loaded on a 12% polyacrylamide gel for SDS-PAGE

1090 and analyzed by Coomassie staining. The protein was visible in the soluble

fraction (SF), total lysate (TL), and in the fraction eluted at 100mM

Imidazole (El_100mM) between the molecular weight of 100 and 140 kDa (correct molecular weight of the protein= 107kDa), whereas the flow-

through (FT) did not contain the specific band, indicating that the majority of the protein was correctly bound to the resin (Figure 10A).
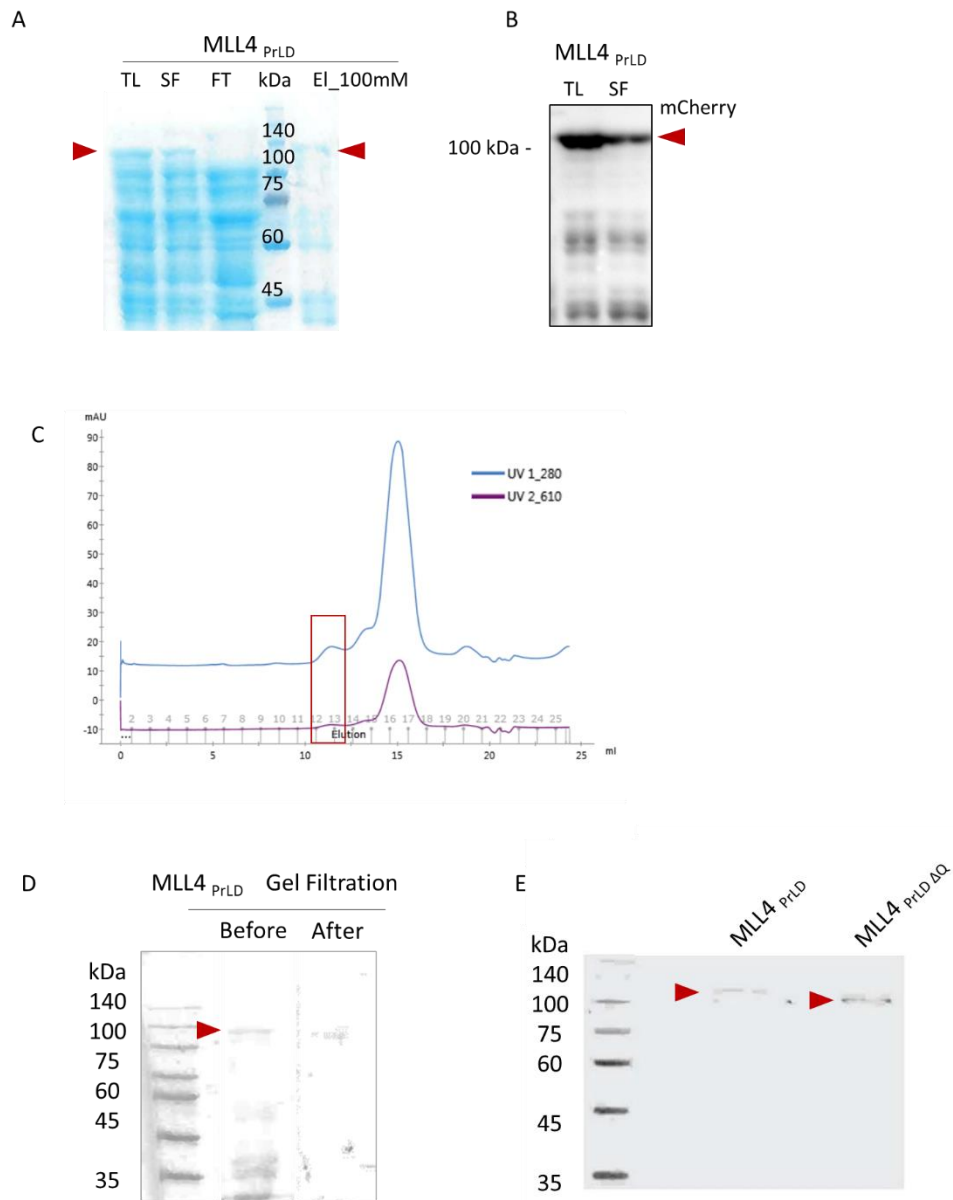


*Figure 10. MLL4 PrLD protein purification and Gel Filtration.* A) SDS-PAGE and Coomassie staining of MLL4PrLD total lysate (TL), soluble fraction (SF), flow-through (FT), and the eluted fraction at 100mM Imidazole (El_100mM). Red arrows show the protein of interest. B) Western blot analysis of MLL4PrLD TL and SF. Anti-mCherry antibody was used to detect the recombinant protein. C) Chromatogram of MLL4 PrLD Gel Filtration showing for each eluted fraction (1-25, x axis) the absorbance intensity at 280 and 610 nm (y axis). The red rectangle surrounds the peak of fractions 12-13 containing MLL4PrLD. D) SDS-PAGE and Coomassie staining of MLL4PrLD before and after Gel Filtration. Non-specific proteins are present only before gel filtration. E) SDS-PAGE and Coomassie staining of MLL4PrLD and MLL4 PrLD ΔQ, respectively 107 and 99 kDa.

| 1096 | By performing a WB against the mCherry we verified that the band observed above 100 kDa was our recombinant protein (Figure 10B). |
|---|---|
| 1098 | Considering the presence of non-specific bands below the molecular weight of 107 kDa, we further purified the eluate through Gel Filtration |
| 1100 | chromatography, a size-exclusion chromatography that allows isolating proteins on the basis of their molecular weight. Figure 10C shows the |
| 1102 | chromatogram of the Gel Filtration of MLL4 $_{PrLD}$ at the wavelength of 280nm (protein absorbance) and 610nm (mCherry signal). On the basis of |
| 1104 | the molecular weight of the MLL4 $_{PrLD}$, protein is expected to be found around fraction 12-13, indeed a peak is visible around this range. Fractions |
| 1106 | showing a peak at 280 and 610nm (12-18) were collected and analyzed by Coomassie staining. The protein cleaned of non-specifics was found in |
| 1108 | fraction 13 (Figure 10D), although fractions 14-18 contained the bands below 75 kDa that were showing a higher signal intensity in the Coomassie |
| 1110 | (Figure 10A, sample El_100mM) as well as higher peaks at 280 and 600nm in the chromatogram (Figure 10C). Figure 10D clearly shows the benefits |
| 1112 | of Gel Filtration. Indeed, after size-exclusion chromatography, only the protein of interest is present in the fraction at the expected molecular |
| 1114 | weight. The same purification procedure was applied for the mCherry-MLL4 $_{PrLD\ \Delta Q}$, the PrLD deprived of the polyQ region, for which the resulting |
| 1116 | cleaned eluted fraction is reported in Figure 10E. In this image of a Coomassie stained gel is also visible the shift in molecular weight of 8kDa |
| 1118 | between MLL4 $_{PrLD}$ and MLL4 $_{PrLD\ \Delta Q}$, due to the deletion of the polyQ stretches. |
| 1120 | These results demonstrate that we were able to purify both MLL4 $_{PrLD}$ and MLL4 $_{PrLD\ \Delta Q}$ recombinant proteins. |
| 1122 | |

## 4.1.3 Droplet formation assay

| | Once the protein of interest was purified, we determined whether |
|---|---|
| 1124 | mCherry-MLL4 $_{PrLD}$ was sufficient to drive LLPS *in vitro*. We found that the |

recombinant protein phase separated at different protein concentrations (3-10 µM) in the presence of a crowding agent (10% PEG) and constant ionic strength (125mM NaCl) (Figure 11A). To determine the saturation concentration ($C_{sat}$) at which the MLL4 $_{PrLD}$ phase-separated, we quantified the intensity of the mCherry signal inside and outside the droplets as suggested in a published work (Wang *et al.*, 2018). We found that the $C_{sat}$ of MLL4 $_{PrLD}$ was ~1.7µM, similar to the one of another PrLD-containing protein, FUS (~2µM) (Wang *et al.*, 2018) (Figure 11B). Of note, the MLL4 $_{PrLD}$ phase separation was reversible, indeed the formed droplets dissolved after increasing the ionic strength up to 600 mM NaCl or by competing out the hydrophobic interactions by adding 1,6-hexanediol (Figure 11C). Altogether these results indicate that MLL4 $_{PrLD}$ was sufficient to drive LLPS in vitro.
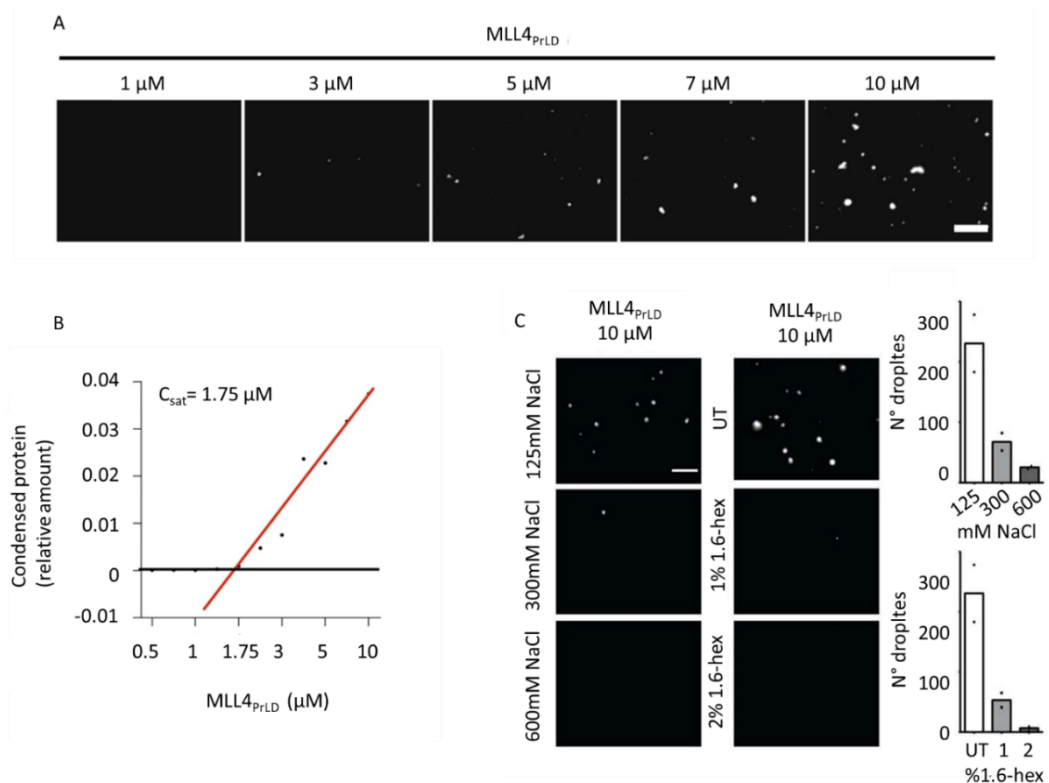


*Figure 11. Phase separation of the recombinant protein mCherry-MLL4$_{PrLD}$. A) Phase separation of MLL4$_{PrLD}$ at constant 125mM salt concentration and increasing concentrations of the protein detected by fluorescence microscopy; scale bar, 5µm. B) Measurement of the saturation concentration: relative amount of condensed MLL4PrLD (y axis) versus the protein concentration (x axis). The regression line is shown in red. C) Phase separation of the mCherry-MLL4$_{PrLD}$ protein visualized by fluorescence microscopy and quantified (bar plot; n=2), in presence of both increasing concentrations of NaCl and 1,6-hexanediol; scale bar 5 µm.*

We next sought to assess the contribution of the polyQ region to MLL4 phase separation. We found that removing the polyQ stretch (MLL4$_{PrLD\,\Delta Q}$)

was sufficient to reduce the capacity of MLL4$_{PrLD}$ to form droplets, suggesting that this region is needed to drive phase separation (Figure

12B). Accordingly, also the Csat of MLL4$_{PrLD\,\Delta Q}$ increased by about 3 times (from ~1.7µM to ~5µM) (Figure 12A), implying that the PolyQ stretch

favors the MLL4 phase separation, at least in vitro. In sum, the obtained results indicated that MLL4 harbors a PrLD which supports its phase

separation in the adopted experimental conditions.
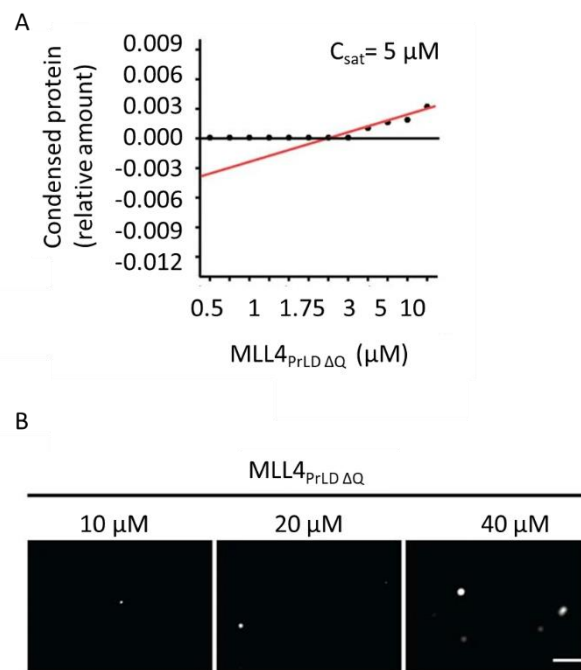


*Figure 12. Phase separation of the recombinant protein mCherry- MLL4$_{PrLD\,\Delta Q}$. A) Measurement of the saturation concentration: relative amount of condensed MLL4$_{PrLD\,\Delta Q}$ (y axis) versus the protein concentration (x axis). The regression line is shown in red. B) Phase separation of MLL4$_{PrLD\,\Delta Q}$ at constant 125mM salt concentration and increasing concentrations of the protein detected by fluorescence microscopy; scale bar, 5µm.*

### 4.1.4 An Optogenetic approach to modulate MLL4 clustering: MLL4-PrLD-HaloTag-Cry2

To determine whether MLL4 PrLD participates in the formation of condensates in living cells, we stably transduced MSCs with the light-activated optoIDR construct, in which MLL4 IDR is fused to the HaloTag and the Cry2 protein, known to self-oligomerize in response to blue light activation. Using the Halo-tagged protein allows to have technical advantages with respect to conventional fluorescent proteins (e.g. GFP, mCherry): the stable covalent bond with the ligand in living cells offers labeling specificity, as well as a versatile system (different emission/excitation wavelengths according to the chosen ligand), and the possibility to perform single-molecule imaging.

To stimulate MLL4-PrLD-HaloTag-Cry2 nucleation while reducing at the minimum the photobleaching and phototoxicity, we determined the optimal experimental conditions such as light source power and time of exposition. Using short exposure times (200 ms) allowed us to follow clusters assembly and disassembly over time, with no need of more than one pulse of light to visualize the clusters, reducing the phototoxicity during the acquisitions.

A pulse of 3 seconds of blue light was enough to stimulate cluster formation in MSCs (Figure 13A). We then measured the number of clusters per nucleus and the size of the foci (Figures 13B and C). In the quantification, we identified as clusters only the rounded foci that were above the intensity threshold calculated as "Nuclear Halo-Tag mean intensity on the pre-stimulus + 4 SD (standard deviation)", thus taking into consideration the expression at the single-cell level of the reporter in the pre-stimulus condition.

By following cluster dynamics up to 30 minutes we could appreciate that MSCs form clusters of ~0.08$\mu m^2$ upon stimulation that remained stable for 400 seconds and then partially increased, probably due to droplets

coarsening (Figure 13C). At the same time, the number of clusters after

1180 ∼300 seconds gradually decreased until it halved after 30 minutes.

Quantification of the number of clusters per cell and condensate size

1182 suggests that cluster dynamics lead small droplets to dissolve, while the

big ones remain intact after 30 minutes of live imaging.
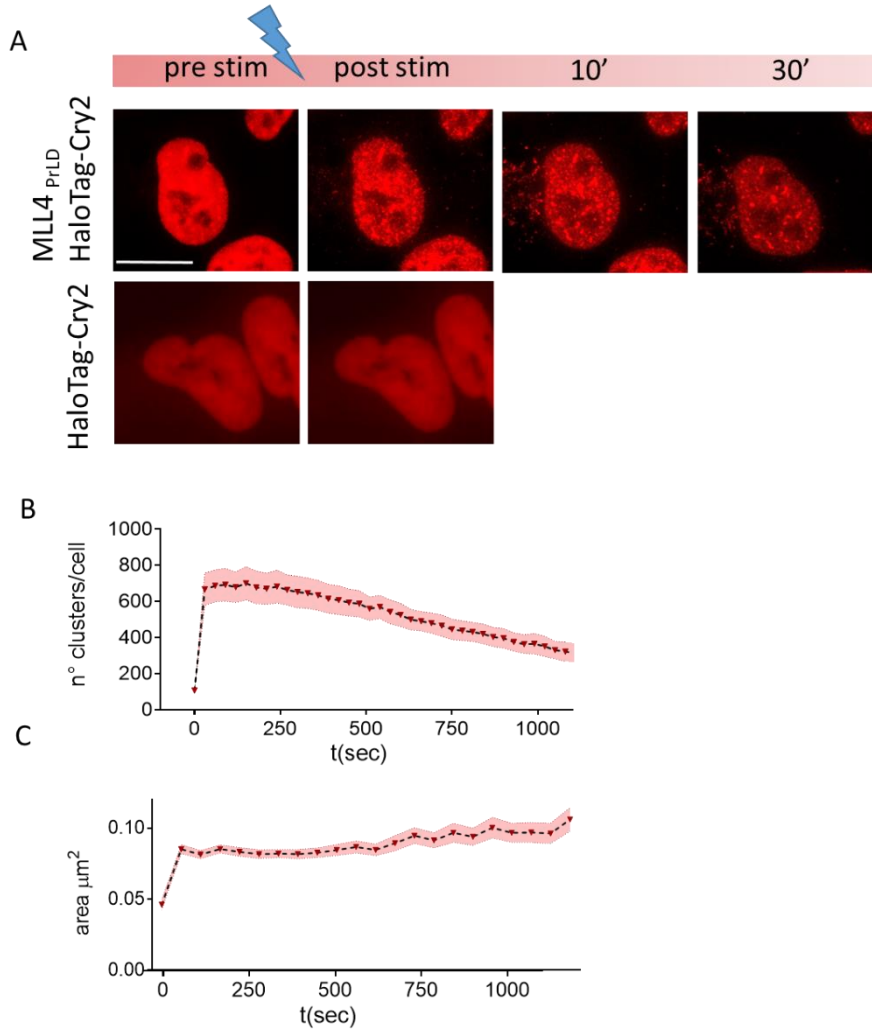


*Figure 13. Blue-light-induced clustering of MLL4-PrLD-HaloTag-Cry2.* *A) Representative images of MLL4-PrLD-HaloTag-Cry2 or HaloTag-Cry2 (control) before and after the stimulus. For the first condition other two time points (10 and 30 minutes) are included; scale bar, 10µm. B) and C) Quantification of the number (left) and area (right) of light-induced droplets of MLL4-PrLD (y axis) at different time points (x axis) (n=8, Mean +/-SEM). The time point t=0 represents the pre-stimulus.*

1184 In contrast, cells expressing only the HaloTag-Cry2 did not form clusters

upon stimulation, indicating that protein condensation is solely driven by

1186 MLL4 PrLD (Figure 13A).

These results indicated that, in living cells, MLL4 PrLD participates in the formation of condensates whose local protein concentration can be modulated by using the light-activated optoIDR approach.

### 4.1.4.1 MLL4 LoF impairs dynamic formation of clusters

We demonstrated that MSCs carrying the heterozygous frameshift mutation (Q4092X) that truncates the MLL4 protein (hereafter termed MLL4$^{LoF}$) harbor an altered chromatin context with respect to the WT

61
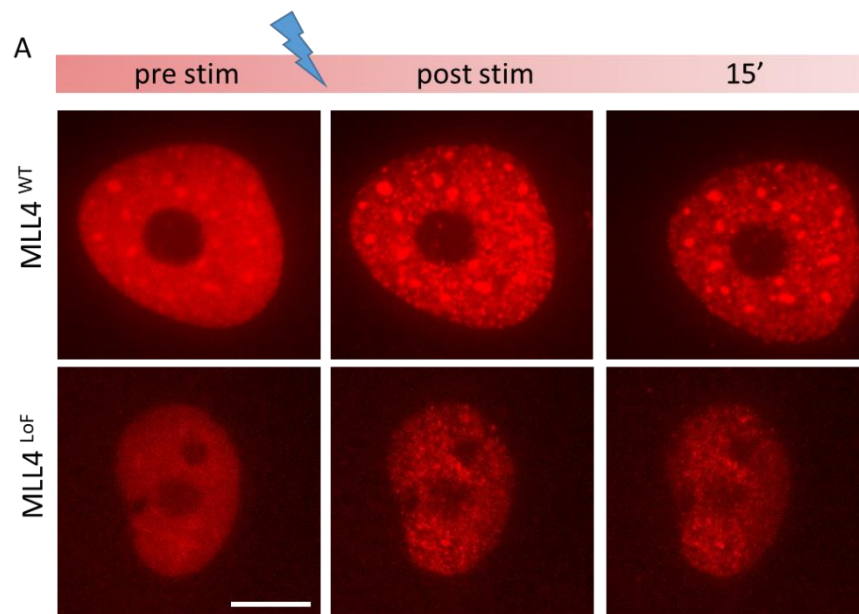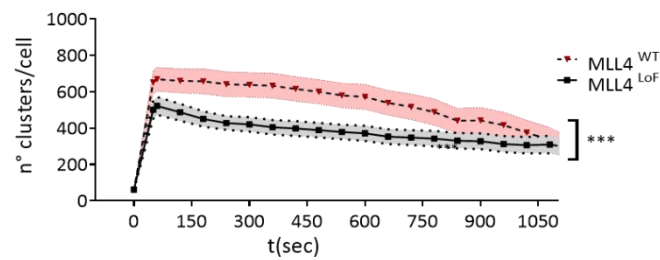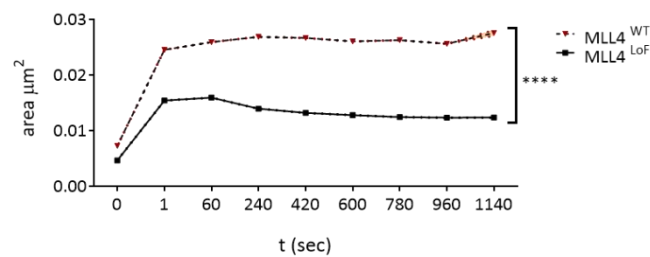
*Figure 14. MLL4 LoF impairs MLL4$_{PrLD}$ clustering.* *A) Representative images of MLL4$^{WT}$ and MLL4 $^{LoF}$ before, after stimulus and 15 minutes post stimulus; scale bar, 10μm. B) and C) Quantification of the number (up) and area (down) of light-induced droplets of MLL4-PrLD (y axis) at different time points (x axis) (n≥19, Mean +/-SEM). The time point t=0 represents the pre-stimulus. One-way ANOVA test was performed.*

counterpart (MLL4$^{WT}$) (Fasciani *et al.*, 2020). Indeed, MSCs MLL4$^{LoF}$ are characterized by an unbalancing between repressive and active chromatin compartments which affect nuclear architecture. Hence, to verify whether the altered chromatin environment in MLL4$^{LoF}$ may have an impact on Transcriptional condensates assembly dynamics, we quantified the number of clusters per cell and the corresponding area of MLL4-PrLD-HaloTag-Cry2 light-stimulated clusters in both MLL4$^{WT}$ and MLL4 $^{LoF}$ MSCs. Interestingly, we observed a decreased number of clusters upon stimulation with blue light (Figure 14B), which size is about 1.6 times smaller in MLL4$^{LoF}$ with respect to MLL4$^{WT}$ MSCs (Figure 14C). Although we are not aware of the exact mechanism underlying the process of nucleation and assembly of MLL4$_{PrLD}$ condensates, we hypothesized that the phenotype observed could be linked to the altered nuclear physical properties of MLL4$^{LoF}$ MSCs. Considering that phase separation is influenced by protein local concentration within cells, we also thought that the reduced MLL4 protein abundance in MLL4$^{LoF}$ MSCs could have an impact on the dynamics of condensates. Furthermore, we analyzed heterogeneous cell populations in which the reporter expression levels could vary in the two cell lines. As mentioned in paragraph 4.1.4 and the Methods section, to avoid bias due to differences in the expression level of the reporter within and between MLL4$^{LoF}$ and MLL4$^{WT}$ MSCs, we took into consideration the expression at the single-cell level of the reporter in the pre-stimulus condition to define and quantify clusters. Overall, this analysis indicated that MLL4 LoF alters the nucleation and growth of MLL4$_{PrLD}$-driven biomolecular condensates.

### 4.1.4.2 MLL4 LoF MSCs condensates are rescued by K27M overexpression

Taking into consideration our findings showing that MLL4 LoF induces a PcG-mediated chromatin clustering that affects nuclear mechanics, we thought to clarify whether the altered MLL4$_{PrLD}$ phase separation observed in the MLL4 LoF condition could be due to the increased PcG condensates in these cells (Fasciani *et al.*, 2020). To test this, we rescued PcG clustering in MLL4$^{LoF}$ MSCs by overexpressing histone H3.3 carrying the p.Lys27Met alteration (H3.3 K27M) (Figure 15). As shown by Western Blot analysis, MLL4 LoF –transduced cells overexpress H3.3 (~ 19kDa), but only MLL4$^{LoF}$ MSCs expressing H3.3 K27M have a lower amount of H3K27me3, due to the dominant negative effect on PcG activity (Figure 15D).

We found that the overexpression of H3K27M rescued the ability of MLL4$^{LoF}$ to form phase-separated droplets after blue light stimulation (Figure 15 A). The impact on cluster number was evident immediately after stimulation, as shown by the similar trend between WT and MLL4 LoF cells (Figure 15B), whether the size of the clusters was recovered over time (Figure 15C). We excluded that the overexpression of H3.3wt alone could have an impact on the dynamics of MLL4$_{PrLD}$ condensates since MLL4 $^{LoF}$ $^{H3.3wt}$ cells behaved similarly to MLL4 $^{LoF}$ (Figure 15 A-C).

In sum, these observations suggest that the impaired MLL4 PrLD clustering in MLL4$^{LoF}$ MSCs could depend on the increased PcG level in this condition. Indeed, restoring their abundance partially rescued MLL4$_{PrLD}$ droplets nucleation and maturation. Considering that the re-establishment of PcG clustering in MLL4$^{LoF}$ MSCs restores a multitude of interrelated processes, including nuclear compartments balancing, morphology and stiffness, further experiments will be required to dissect which exact mechanism is primarily involved in affecting MLL4$_{PrLD}$ clustering. In addition, by overexpressing the K27M histone variant we observed only a partial rescue of cluster area (Figure 15C), indicating that other factors could impact on the phase separation behavior of MLL4$_{PrLD}$ (e.g. endogenous MLL4, BRD4,

63
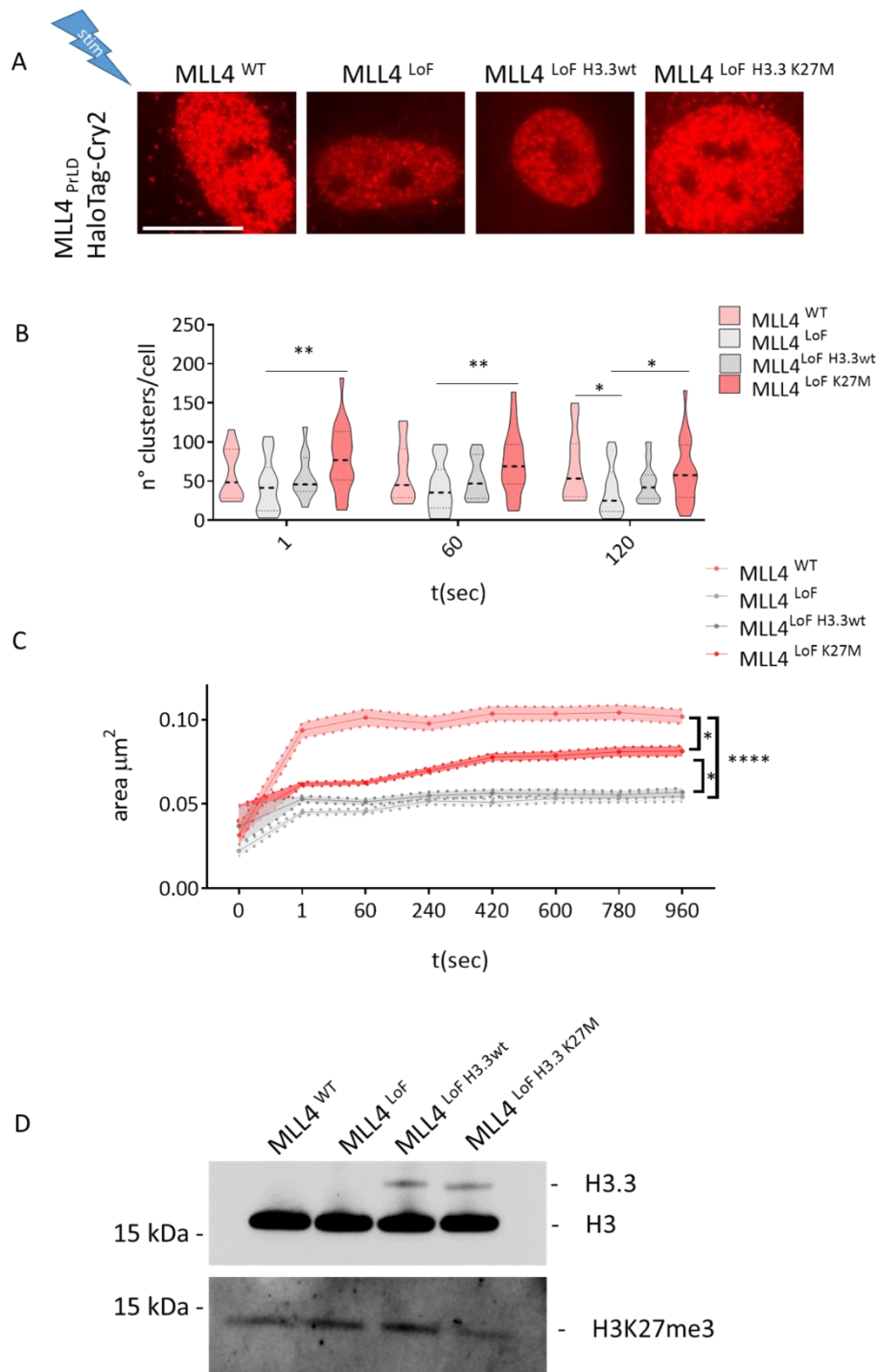
*Figure 15. MLL4 LoF MSCs condensates are rescued by K27M overexpression.* A) Representative images of MLL4$^{WT}$, MLL4 $^{LoF}$, MLL4 $^{LoF\ H3.3wt}$ and MLL4 $^{LoF\ H3.3\ K27M}$ after stimulus; scale bar, 10μm. B) and C) Quantification of the number (up, violin plot) and area (down) of light-induced droplets of MLL4-PrLD (y axis) at different time points (x axis) (n≥13, Mean +/-SEM). The time point t=0 represents the pre-stimulus, time point t=1 the post stimulus. One-tailed unpaired Student's t-test (B) or one-way ANOVA test (C) was performed. D) Western blot analysis of H3K27me3 in MLL4$^{WT}$, MLL4 $^{LoF}$, MLL4 $^{LoF\ H3.3wt}$ and MLL4 $^{LoF\ H3.3\ K27M}$. Histone H3 was used as the loading control.

MED1 protein abundance). Nonetheless, this analysis emphasized a role

for chromatin physical properties in tuning nuclear condensates assembly

1250

1252        and dynamics.


## 4.2 MLL4 LoF affects cell response to changes in substrate stiffness

1254

The extracellular matrix (ECM) is a highly dynamic structure that continuously

1256    undergoes remodeling, which is mediated by specific enzymes that are responsible

for the cleavage of ECM components, such as metalloproteinases (MMPs). ECM

1258    composition, structure, and stiffness regulate a myriad of processes. Physiologically,

the ECM interacts with cells and determines diverse functions, including

1260    proliferation, migration, cell fate, as well as tissue homeostasis and development

(Panciera *et al.*, 2017). It has been shown that ECM remodeling has a pivotal role in

1262    regulating the morphogenesis of the intestine and lungs, as well as of the mammary

and submandibular glands. For example, elastin and collagen deposition increase

1264    ECM stiffness in the neonatal lung, thus enabling signaling through the endothelial

lipoprotein receptor-related protein 5 (LRP5) pathway, which is crucial for normal

1266    lung development (Bonnans, Chou and Werb, 2014). Interestingly, dysregulation of

ECM structure contributes to several pathological conditions and can inflame

1268    disease progression (Bonnans, Chou and Werb, 2014). For instance, abnormal ECM

deposition and stiffness are observed in fibrosis and cancer, and excessive ECM

1270    degradation in osteoarthritis. In the context of tumors, ECM can promote tumor

progression. In fact, specific ECM gene signatures can layer breast cancer into

1272    subclasses that predict patient prognosis. Tumors with high expression of protease

inhibitors correlate with good outcomes, whereas those with high MMPs correlate

1274    with poor prognosis and increased risk of relapse (Bergamaschi *et al.*, 2008). Other

studies pinpoint the importance of the ECM in promoting metastatic tumor cell

1276    growth in the metastatic niche (Oskarsson *et al.*, 2011).

MSCs are an established cellular model in the mechanotransduction field, and it has

1278    been shown that the differentiation of MSCs is dictated by the physical properties

of the cell microenvironment, such as ECM stiffness. Experimentally this can be

1280    controlled by allowing cells to stretch on stiff substrates or by inducing cell rounding

by culturing them on soft substrates. Interestingly, MSCs adopt an osteogenic fate

when in contact with a stiff matrix, whereas they turn into adipocytes at low mechanical stresses in soft substrates (Panciera *et al.*, 2017).

Recently, we found that MLL4[LoF] MSCs are characterized by an impairment of nuclear mechanics which is coupled with differentiation defects (Fasciani *et al.*, 2020). Specifically, we observed that the unbalancing between chromatin compartments, namely Transcriptional and PcG condensates, in MLL4[LoF] MSCs, leads to fail osteogenesis and chondrogenesis both in vitro and in vivo.

Exogenously expressing MLL4 and releasing the nuclear mechanical stress through inhibition of the mechanosensor ATR rescued the altered differentiation potential by re-establishing the mechanical responsiveness of MSCs. Taking these results into consideration, we hypothesized that the nuclear condensates could be responsive to changes in substrate stiffness and that this specific nuclear response could be altered in the presence of *KMT2D* haploinsufficiency. Hence, we investigated whether the substrate stiffness could affect the assembly of both Transcriptional and PcG condensates in MSCs, and the relative contribution of MLL4 LoF.

### 4.2.1 Sensors and mediators of mechanical cues: Lamin A/C and Yap/Taz response

Before examining the response of nuclear condensates to change in ECM stiffness, we first analyzed by Immunostaining two mechanotransducers, LAMIN A/C and YAP/TAZ, in low (0.5 kPa), intermediate (8 kPa) and high (32 kPa) stiffness conditions. This enabled us to determine whether the applied mechanical stimuli were properly perceived by the MSCs.

We found that in the soft matrix both LAMIN A/C and YAP/TAZ nuclear to cytosolic ratio (NCI) decreased linearly in WT MSCs with respect to 32 kPa (Figure 16), in line with what has been previously reported (Swift *et al.*, 2013; Harada *et al.*, 2014; Panciera *et al.*, 2017). Of importance, MLL4[LoF] MSCs did not show the same trend, losing the linearity in the response to the increment of ECM stiffness. Indeed, immunofluorescence analysis indicated that the presence of *KMT2D* haploinsufficiency caused an increase in the nuclear signal of both markers at 0.5 kPa with respect to 32
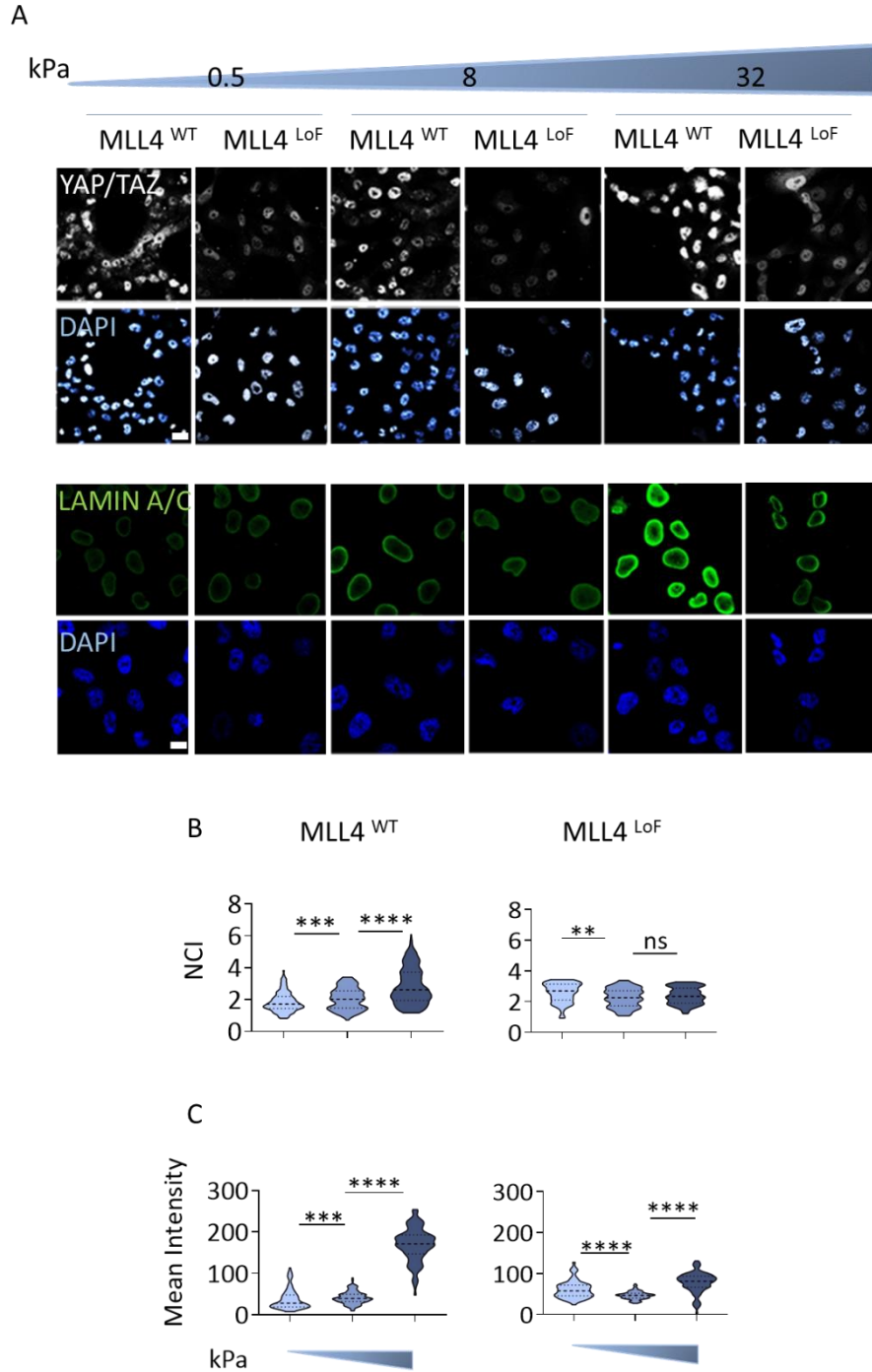
*Figure 16. LAMIN A/C and YAP/TAZ response to changes in substrate stiffness. A) Representative images of Immunostaining against YAP/TAZ (scale bar 20µm; 0.75X zoom) and LAMIN A/C (scale bar 10µm; 2X zoom) in MLL4<sup>WT</sup> and MLL4 <sup>LoF</sup> MSCs at 0.5, 8 and 32kPa. DAPI stained nuclei. B) Violin pots showing nuclear to cytosolic localization of YAP/TAZ (n≥80). C) Quantification of nuclear mean intensity of LAMIN A/C (n≥75). Two-tailed unpaired Student's t-test was performed.*

kPa, indicating that MLL4 LoF impacted on cell responsiveness. Interestingly, at 32 kPa MLL4<sup>LoF</sup> MSCs showed a decrease in LAMIN A/C and YAP/TAZ nuclear to cytosolic ratio with respect to WT state, recapitulating

1312

1314  the results obtained in normal culture conditions (plastic stiffness $\sim 1X10^7$ kPa) (Fasciani *et al.*, 2020).

1316  Overall, the quantification of LAMIN A/C signal and YAP/TAZ distribution indicated that WT MSCs mechanically sense the stiffness of the substrate

1318  responding accordingly to what is reported in previous studies, whereas MLL4[LoF] MSCs are characterized by an altered mechanical response.

## 4.2.2 Polycomb and Transcriptional condensates are modulated by changes in substrate stiffness

1320

  Considering the observed linear response of YAP/TAZ nuclear shuffling

1322  with respect to the increased ECM stiffening, we decided to continue our analyses on nuclear condensates by comparing the softest (0.5 kPa) and

1324  stiffest (32 kPa) conditions.
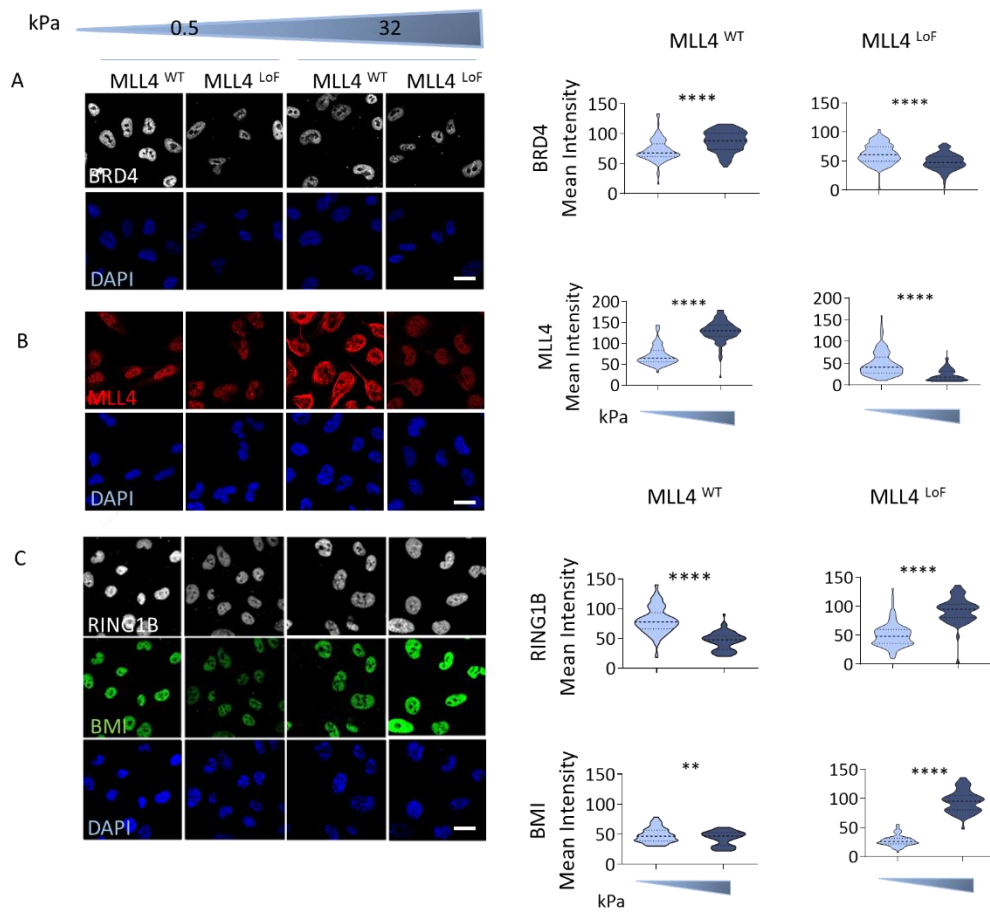
*Figure 17. Transcriptional and Polycomb condensates response to changes in substrate stiffness.*
*A-C) Representative images of Immunostaining against BRD4 (A), MLL4 (B), RING1B/BMI (C)*
*(scale bar 10µm; 2X zoom) in MLL4$^{WT}$ and MLL4 $^{LoF}$ MSCs at 0.5 and 32kPa, with the*
*corresponding quantification of the nuclear mean intensity on the right (BRD4 n≥87, MLL4 n≥83,*
*RING1B/BMI n≥76). Two-tailed unpaired Student's t-test was performed.*

Single-cell analyses by immunofluorescence, which allow to quantify endogenous protein levels, revealed that markers of Transcriptional and Polycomb condensates adapt to the soft matrix in opposite ways in WT MSCs (Figure 17A-C). Indeed, quantification of nuclear protein abundance showed that MLL4 and BRD4 decreased in MLL4$^{WT}$ at 0.5 kPa, whereas RING1B and BMI presented a higher signal with respect to 32 kPa (Figure 17A-C). Of note, quantitative immunofluorescence of the same proteins in MLL4$^{LoF}$ MSCs showed that *KMT2D* haploinsufficiency altered condensates response to increase of stiffness. MLL4$^{LoF}$ MSCs cultured at 0.5 kPa are characterized by increased MLL4/ BRD4 and decreased RING1B/ BMI protein abundance in comparison to MLL4$^{LoF}$ MSCs at 32 kPa (Figure 17A-C). Although we quantified nuclear protein levels by immunofluorescence, we did not confirm these results with other techniques, such as the evaluation of total protein extracts by Western blot analysis. Furthermore, we cannot exclude that the changes observed in terms of protein abundance are due to differences in the transcript levels, for which further experiments are needed (quantitative PCR).

To assess whether the increased or decreased nuclear protein abundance affects the distribution of condensates within the nucleus and their organization in clusters, we quantified the number of BMI and BRD4 clusters per cell (Figure 18A and B). 2D cluster analysis indicated that in MLL4$^{WT}$ the number of BMI clusters per cell increased at 0.5kPa, whereas BRD4 clusters dropped under the same stiffness. MLL4$^{LoF}$ MSCs did not follow the same pattern, showing a diminished number of BMI clusters at 0.5 kPa as well as a gain in BRD4 clusters with respect to 32 kPa (Figure 18A-C). Of note, the measurements of the number of clusters per cell reflect the same trend observed by quantifying nuclear mean intensity.

1352 Overall, these results suggest that Transcriptional and Polycomb
condensates could be involved in cell mechanoresponsiveness and that
1354 the antagonistic function between these two chromatin compartments is
maintained also when cellular mechano-environment changes.
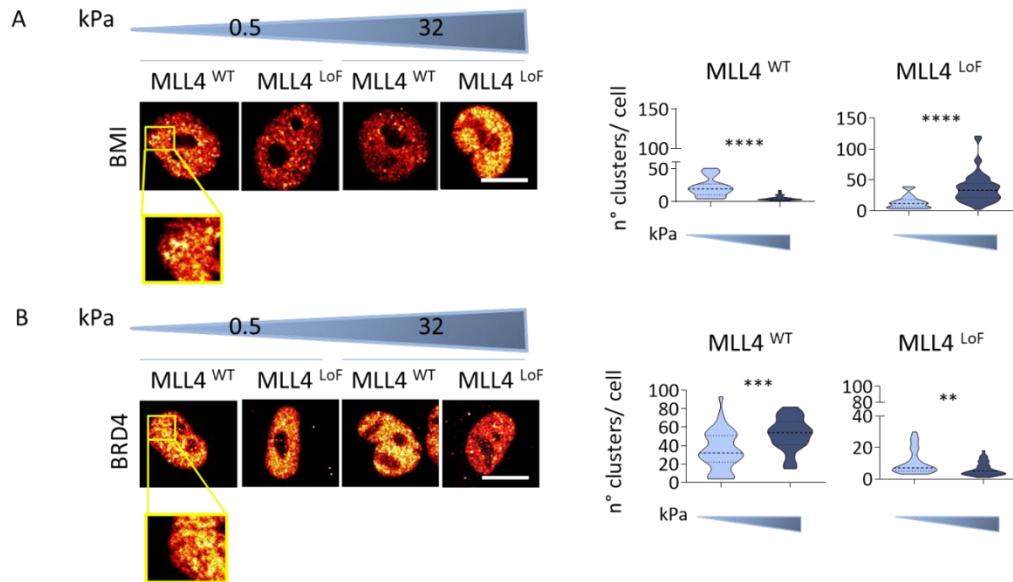


*Figure 18. BMI and BRD4 cluster quantification (2D) confirms the results obtained by measuring total nuclear intensity. A-B) Representative images of Immunostaining of BMI (A) and BRD4 (B) (scale bar 10μm; 3X zoom), with the corresponding 2D cluster quantification (on the right, n° of clusters per cell) (n≥30). Two-tailed unpaired Student's t-test was performed.*

1356 Furthermore, the presence of MLL4 LoF mutation impairs the MSCs
mechanical nuclear condensates-driven response, strengthening the role
1358 of MLL4 in the maintenance of nuclear mechanics.

1360

### 4.2.3  MLL4 LoF phenotype is rescued by K27M overexpression

To verify whether the differences observed between MLL4$^{WT}$ and MLL4$^{LoF}$
1362 MSCs at 0.5 and 32 kPa were dependent on PcG condensates, we rescued
their functionality by overexpressing H3.3 K27M in MLL4$^{LoF}$ MSCs. In
1364 Fasciani *et al.*, we observed that K27M overexpression rescued
Transcriptional and PcG condensates abundance in MLL4$^{LoF}$ MSCs.
1366 Furthermore, PcG rescue re-established nuclear architecture parameters,

including nuclear size and shape, LAMIN A/C protein abundance, and

nuclear stiffness in MLL4$^{LoF}$ MSCs (Fasciani *et al.*, 2020).

Taking into consideration these results, we quantified by

immunofluorescence LAMIN A/C levels, also in its phosphorylated state,
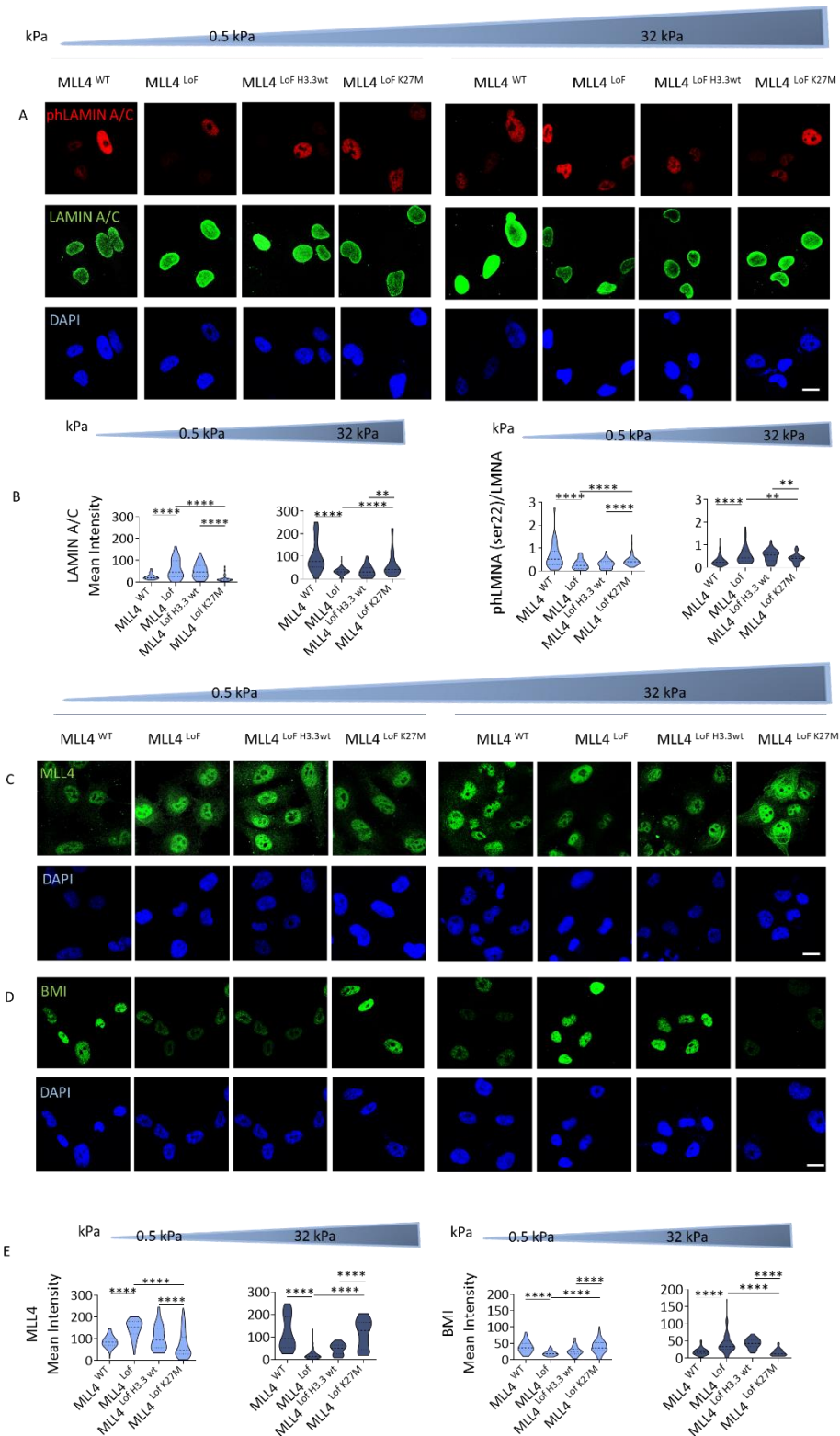
*Figure 19. MLL4 LoF phenotype is rescued by K27M overexpression. A,C,D) Representative images of Immunostaining of phLAMIN A/C, LAMIN A/C (A) MLL4 (C), BMI (D) (scale bar 10µm; 2X zoom) in MLL4$^{WT}$, MLL4$^{LoF}$, MLL4$^{LoF\ H3.3wt}$, and MLL4$^{LoF\ H3.3\ K27M}$. B,E) Nuclear mean intensity quantification is shown for LAMIN A/C and ratio between phLAMIN A/C and LAMIN A/C (B), MLL4 and BMI (E) (70 ≤n≤ 150). Two-tailed unpaired Student's t-test was performed.*

which is an indication of protein turnover (Figure 19A and B), and Transcriptional and Polycomb condensates, specifically by looking at MLL4 and BMI proteins (Figure 19C-E). By restoring PcG abundance in MLL4$^{LoF}$ MSCs we rescued LAMIN A/C and phLAMIN A/C Ser22 levels at both 0.5 and 32kPa, as well as MLL4 and BMI nuclear protein abundance. Nevertheless, further analyses are needed to clarify whether the rescue driven by K27M overexpression is due to alteration of either the transcriptional or protein stability level. Furthermore, with respect to MLL4$^{WT}$ MSCs, MLL4$^{LoF}$ MSCs showed an increased ratio between phLAMIN A/C Ser22 and LAMIN A/C at 32 kPa, an indication of lamin depolymerization, a process that is consistent with low nuclear mechanical stress conditions (Swift *et al.*, 2013).

Overall, these results indicated that restoring PcG clustering rescued the altered phenotype of MLL4$^{LoF}$ MSCs at 0.5 and 32 kPa.

## 4.2.4 MLL4 LoF interferes with nuclear morphology adaptations mediated by the soft matrix

Taking into consideration the connection between defects in chromatin compartments and nuclear architecture, we sought to investigate whether the altered equilibrium between Transcriptional and Polycomb condensates in MLL4$^{LoF}$ MSCs, which persists when cells are plated on a soft matrix, is mirrored by perturbation of nuclear architecture. Therefore, we quantified physical parameters such as nuclear area, volume, flatness and nuclear envelope (NE) perimeter on the basis of the nesprin signal, which allows taking into account NE invaginations whenever present.

Analysis of nuclear morphology showed that MLL4$^{WT}$ MSCs responded by decreasing nuclear area, volume, and flatness at 0.5 kPa in comparison

with the stiff matrix (Figure 20A-C). These results are in line with what has been previously observed by keeping MSCs under low tensional forces (Swift *et al.*, 2013). However, when we compared the nuclear morphology of MLL4$^{LoF}$ MSCs under low and high mechanical loads, we did not measure any significant difference with respect to the nuclear area, volume or flatness (Figure 20A-C). To measure nuclear envelope (NE) indentations, we calculated the perimeter of the nuclear nesprin signal in MSCs overexpressing MiniNesprin1-GFP (Figure 20D-F). To avoid bias due to the differences in the area of MLL4$^{WT}$ and MLL4$^{LoF}$ nuclei, the NE perimeter measurement was normalized on MSCs nuclear area. Quantification of NE perimeter over nuclear area showed that MLL4$^{WT}$ MSCs are characterized by an augmented presence of NE invaginations at 0.5 kPa with respect to 32 kPa. Interestingly, the same pattern is observed in MLL4$^{LoF}$ MSCs (Figure 20F). In this case, although the trend of an increased NE perimeter at 0.5 kPa in comparison to 32 kPa is maintained, the magnitude of this change is less striking. Interestingly, MLL4$^{LoF}$ MSCs cultured at 32 kPa showed increased NE perimeter with respect to MLL4$^{WT}$ MSCs at the same substrate stiffness. Of note, there are studies indicating that cells cultured on a soft matrix show wrinkled nuclei typically distinguished by an increased number of NE indentations in comparison with the smoothed-out and flattened nuclei that characterize cells plated on a stiff matrix (Swift *et al.*, 2013).

In sum, quantification of nuclear morphology's parameters suggested that *KMT2D* haploinsufficiency interfered with MSCs ability to undergo physical adaptations linked to nuclear architecture and mediated by ECM stiffness.

A
kPa

0.5                    32

MLL4 WT    MLL4 LoF        MLL4 WT    MLL4 LoF

DAPI_3D

B                    2D quantification

MLL4 WT          MLL4 LoF          32 kPa

area μm²

****              ns              ****

C                    3D quantification

MLL4 WT          MLL4 LoF          32 kPa

volume μm³

****              ns              **

flatness

****              ns              **

D
kPa

0.5                    32

MLL4 WT    MLL4 LoF        MLL4 WT    MLL4 LoF        NESPRIN

NESPRIN/DAPI

E
MLL4 WT          MLL4 LoF          32 kPa

NE perimeter μm
(Nesprin)

ns              ****              *

F

NE perimeter/
Nuclear area (μm⁻¹)

****              **              **

1420                                                                74
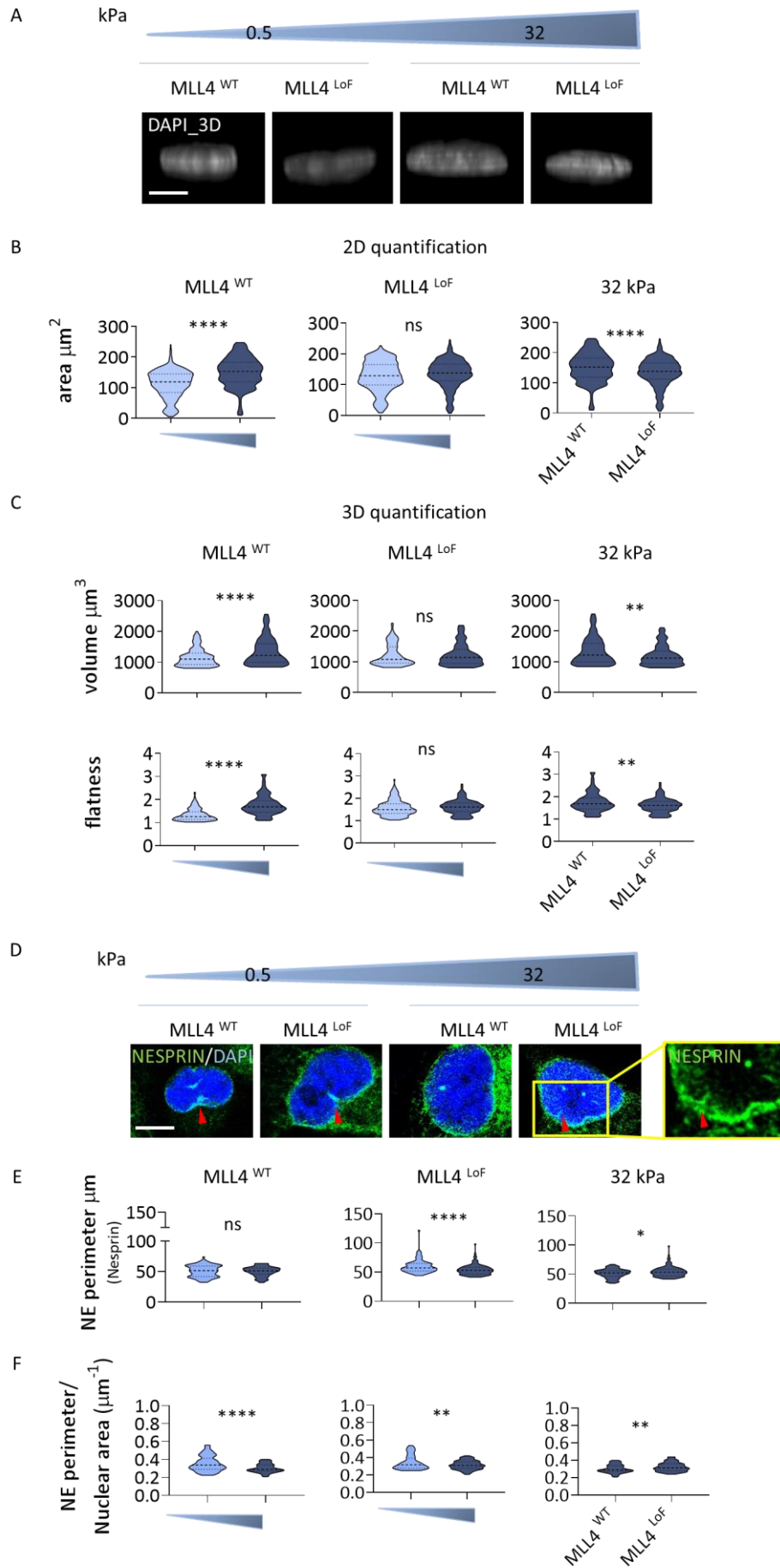
*Figure 20. MLL4 LoF interferes with nuclear morphology adaptations mediated by the soft matrix.*
*A) Reconstructed 3D images of the nuclear shape in MLL4$^{WT}$ and MLL4$^{LoF}$ MSCs cultured at 0.5*
*and 32 kPa. Scale bar, 5µm; zoom 1X. B) 2D quantification of MLL4$^{WT}$ and MLL4$^{LoF}$ MSCs nuclear*
*area (355 ≤n≤ 415, merge of three independent replicates). C) 3D quantification of MLL4$^{WT}$ and*
*MLL4$^{LoF}$ MSCs nuclear volume and flatness (130 ≤n≤ 224, merge of two independent replicates).*
*D) Representative images of MiniNesprin1-GFP expressing cells (merged with DAPI signal). Scale*
*bar, 5µm; zoom 2X. Red arrows depict NE invaginations. E-F) Quantification of nuclear envelope*
*(NE) perimeter (n≥90, merge of two independent replicates). Figure F shows NE perimeter values*
*normalized on the nuclear area. Two-tailed unpaired Student's t-test was performed.*

## 4.2.5  Validation of MLL4 LoF phenotype in independent clones

In order to avoid any bias due to clonal selection we sought to confirm
some of the results obtained in an independent MSCs MLL4$^{WT}$ clone
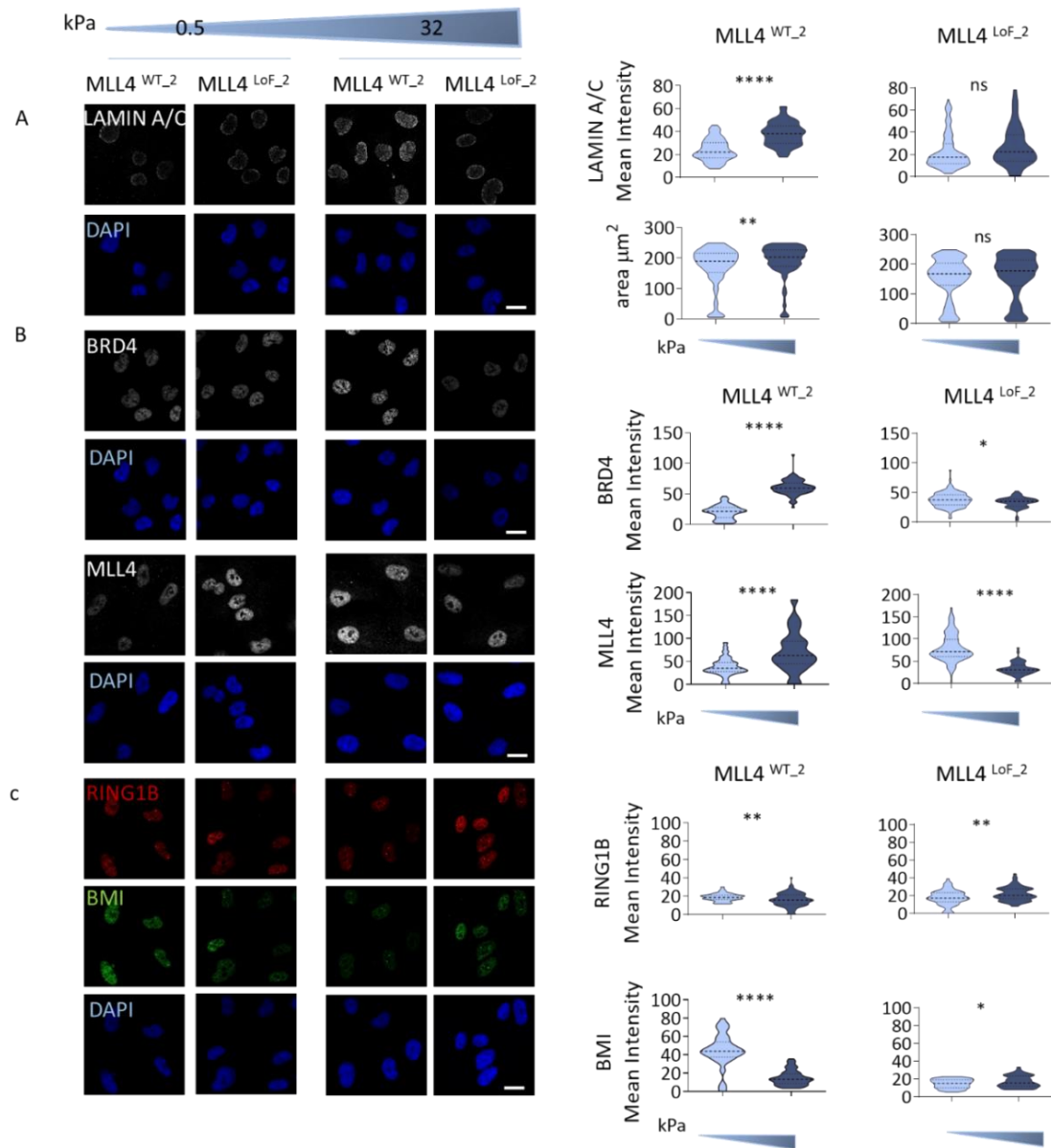
*Figure 21. Validation of MLL4 LoF phenotype in independent clones.* Representative images of Immunostaining of LAMIN A/C (A), BRD4 and MLL4 – Transcriptional condensates (B), RING1B and BMI – Polycomb condensates (C) in MLL4 $^{WT\_2}$ and MLL4 $^{LoF\_2}$ (scale bar 10μm; 2X zoom). On the right, nuclear mean intensity quantification is shown for each protein (60 ≤n≤ 130). Next to LAMIN A/C staining is reported the quantification of nuclear area (264 ≤n≤ 413, merge of three independent replicates). Two-tailed unpaired Student's t-test was performed.

(MLL4$^{WT\_2}$) and another MLL4$^{LoF}$ clone carrying a different truncating mutation of MLL4 (P4093X), hereinafter referred to as MLL4$^{LoF\_2}$.

Quantifications of LAMIN A/C (Figure 21A), Transcriptional (Figure 21B) and Polycomb condensates (Figure 21C) nuclear signal showed that MLL4$^{WT\_2}$ and MLL4 $^{LoF\_2}$ MSCs behaved similarly to MLL4$^{WT}$ and MLL4$^{LoF}$ MSCs at 0.5 and 32 kPa. In addition, the nuclear area of MLL4 $^{WT\_2}$ and MLL4 $^{LoF\_2}$ MSCs responded accordingly to previous results, indicating that the pattern observed is independent from the point mutation causing MLL4 LoF and from the clonal selection procedure.

## 4.2.6  Substrate stiffness tunes MLL4 condensates assembly

At the steady state, we observed that markers of Transcriptional and Polycomb condensates are modulated by changes in substrate stiffness. To verify whether the MLL4-PrLD clustering dynamics could be affected similarly, we adopted the optogenetic tool to determine the pattern of cluster assembly over time in MSCs plated at 0.5 and 32 kPa.

After blue light stimulation of MLL4$^{WT}$ MSCs, we measured a reduced assembly of MLL4-PrLD clusters in the soft matrix. In the same setting, we also determined an increment of the cluster size, with respect to what we measured by plating cells on the stiff matrix (Figure 22). Although we could appreciate the same trend of larger clusters in MLL4$^{LoF}$ MSCs in the soft matrix (2.3 times bigger), no significant change was measured in terms of number of clusters.

76

Altogether, these findings suggest that substrate rigidity affects the dynamic assembly of MLL4-PrLD clusters in living cells. Furthermore, MLL4 LoF partially impairs condensate formation in response to matrix softening.
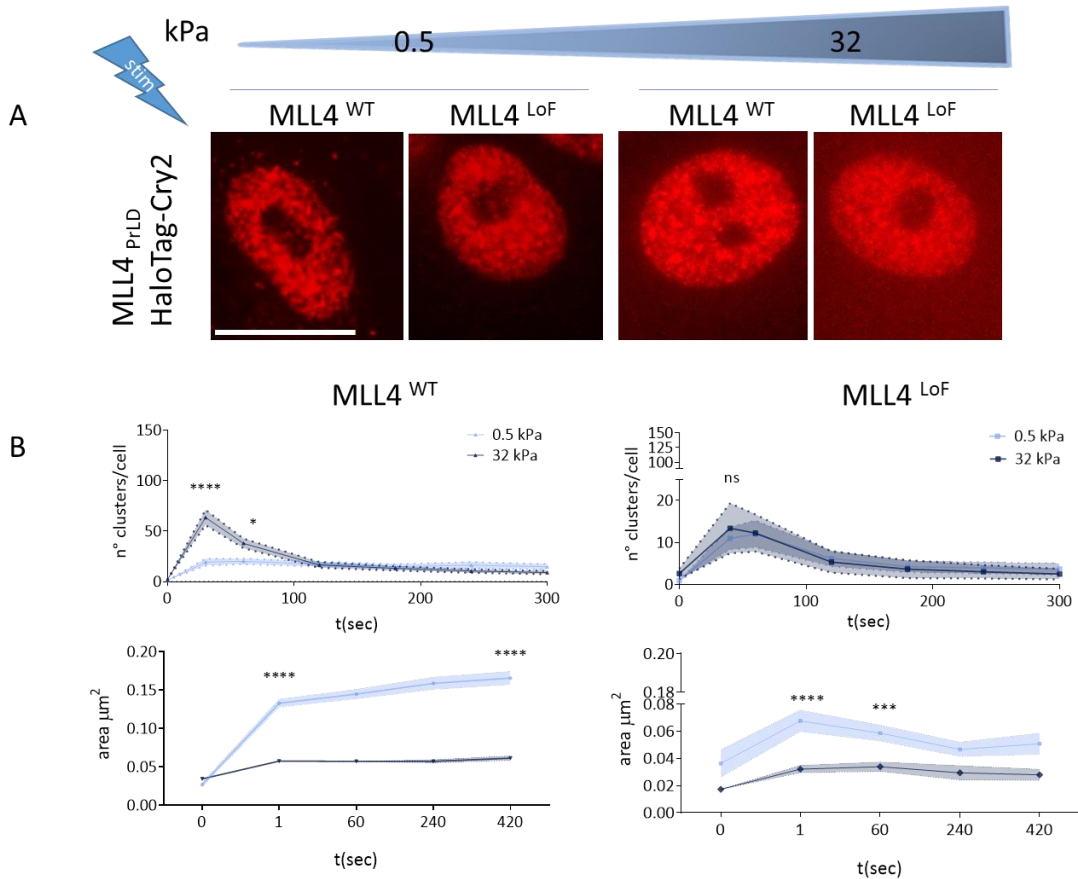


Figure 22. Substrate stiffness tunes MLL4 condensates assembly. A) Representative images of MLL4$^{WT}$ and MLL4 $^{LoF}$ after stimulus at 0.5 and 32 kPa; scale bar, 10μm. B) Quantification of the number of clusters per cell and cluster area of light-induced droplets (MLL4-PrLD) (y axis) at different time points (x axis) (n≥17, Mean +/-SEM). The time point t=0 represents the pre-stimulus, time point t=1 the post stimulus. One-way ANOVA test was performed.

## 4.3 Quantification of nanoscale chromatin compaction by FLIM-FRET approach

In our previous work, we showed that the increased Polycomb clustering in MLL4 LoF is associated with higher nuclear stiffness, as we demonstrated by Brillouin microscopy (Fasciani *et al.*, 2020). We also observed in MLL4$^{LoF}$ MSCs increased chromatin compaction by measuring H4K16ac level, a histone mark known to weaken internucleosomal interactions, thus affecting chromatin structure.

77

We proceeded to further investigate this aspect by taking advantage of FLIM-FRET, a technique that allows the spatial and quantitative mapping of direct interactions between fluorescent probes in living conditions. Indeed, FRET is a distance-dependent physical phenomenon by which energy is transferred non- radiatively from an excited fluorophore molecule (Donor) to another fluorophore (Acceptor). In this setting, FRET occurs if the donor and acceptor fluorophores are positioned between 1-10 nm one from each other (Sekar and Periasamy, 2003). In our study, GFP and mCherry fluorescent proteins are the donor and acceptor molecules, respectively. FRET can be detected by different fluorescence intensity-based imaging techniques such as sensitized emission or acceptor photobleaching. In this study, we used fluorescence lifetime imaging (FLIM) to measure FRET. This technique monitors changes in the fluorescence lifetime regardless of the fluorescence intensity levels and provides high spatial and temporal resolution (Llères *et al.*, 2009). We applied the FLIM-FRET approach to characterize the nucleosomal structure of chromatin in living cells. To study nucleosome-nucleosome proximity (chromatin nano-compaction), we generated single MSCs clones stably expressing H2B-GFP alone (Donor) and both H2B-GFP and H2B-mCherry (Donor + Acceptor) and performed FLIM-FRET measurements.

### 4.3.1 Generation of MSCs clones co-expressing H2B-mCherry/H2B-GFP

In order to have a homogenous cell population with a comparable level of expression of H2B-mCherry/H2B-GFP (2FPs), we isolated single clones. After clonal selection (at least two per cell line), we verified the level of expression of MSCs clones co-expressing H2B-mCherry/ H2B-GFP by fluorescent microscopy, quantifying the GFP and mCherry signal intensity (Figure 23A).

As shown in panel Figure 23A, the H2B signal was nuclear and homogenous within the cell populations. The nuclear mean intensity quantification showed some variability in the expression of both H2B-mCherry and H2B-GFP among MSCs MLL4$^{WT}$ and MLL4$^{LoF}$ clones, which was overall in the same range. Furthermore, Western blot analysis of histone extracts confirmed a comparable level of H2B-mCherry and H2B-GFP expression among MSCs clones (Figure 23B). To further characterize the selected

1482

1484

1486
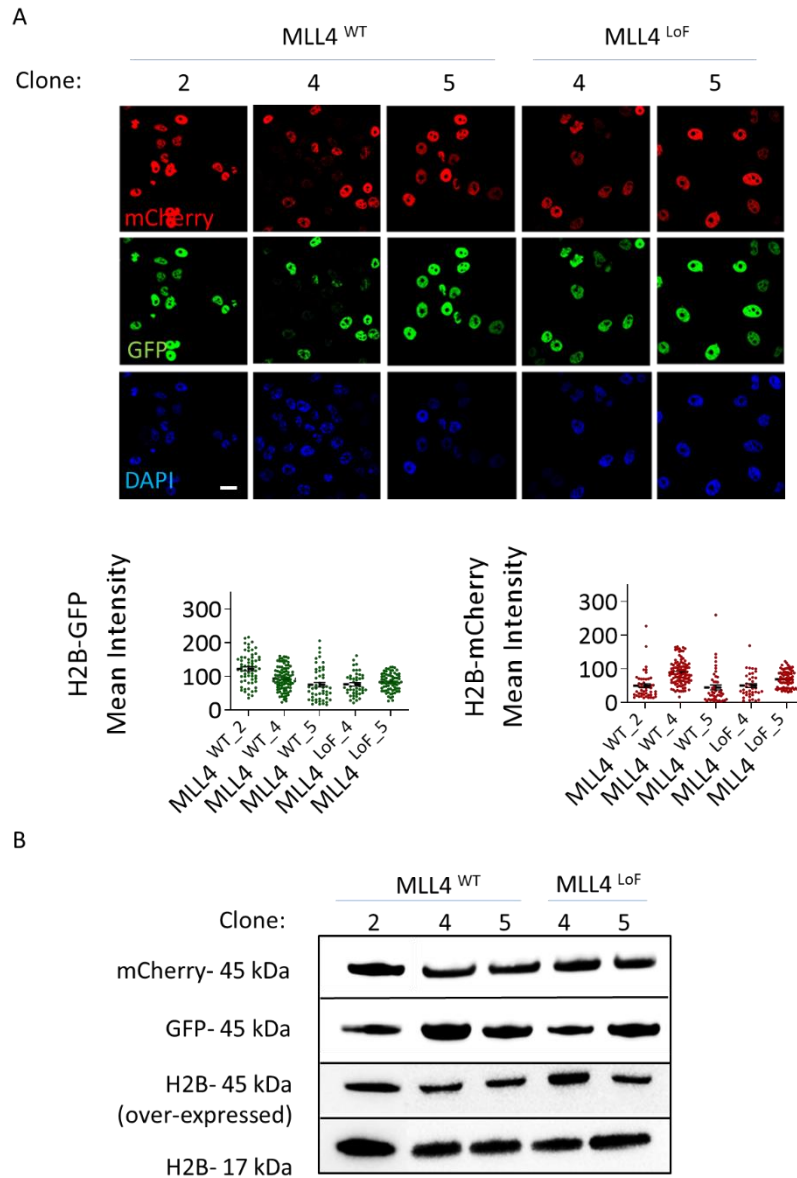


*Figure 23. Expression analysis of 2FPs-H2B MSC single clones.* A) Upper panel: representative images of MLL4$^{WT}$ and MLL4$^{LoF}$ H2B-2FPs (mCherry/ GFP) single clones (scale bar 20μm; 1X zoom). Lower panel: scatter dot plot of H2B-mCherry (red) H2B-GFP (green) (Mean +/-SEM; 50 ≤n≤ 90). B) Western blot analysis of H2B endogenous (17 kDa) and exogenous (recombinant protein, 45 kDa), catched by H2B, mCherry, and GFP antibody in H2B-2FPs MLL4$^{WT}$ and MLL4$^{LoF}$ clones.

79

clones, we monitored the nuclear morphology and chromatin features that distinguished the MLL4$^{LoF}$ from the MLL4$^{WT}$ MSCs (Figure 24A).

MLL4$^{LoF}$ MSCs clones showed a decreased BRD4 signal intensity, as well as smaller nuclei, with respect to MLL4$^{WT}$ MSCs clones. Of importance, the

expression of H2B-2FPs did not impact on the cell growth and cell cycle profile, suggesting that the expression of the exogenous H2B reporter

system did not alter the cellular state (Figure 24B).
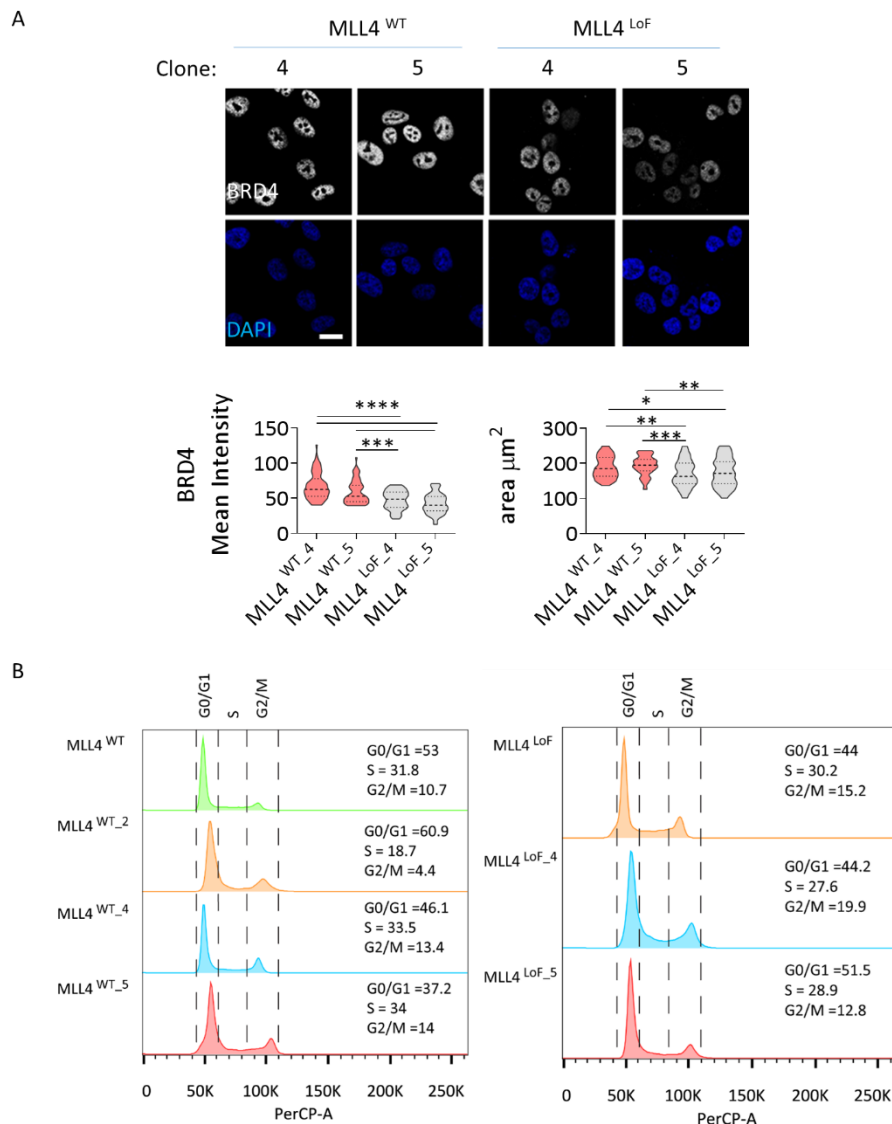


*Figure 24. Phenotypic characterization of 2FPs-H2B MSC single clones. A) Representative images of BRD4 Immunostaining in MLL4$^{WT}$ and MLL4$^{LoF}$ indicated clones (scale bar 10µm; 2X zoom). Below, nuclear mean intensity quantification is shown (60 ≤n≤ 115). Two-tailed unpaired Student's t-test was performed. B) FACS analyses showing cell cycle distribution of MLL4$^{WT}$ and MLL4$^{LoF}$ H2B-2FPs stable cell lines.*

## 4.3.2 FLIM-FRET analysis reveals a High-FRET population in MLL4 LoF

To measure chromatin compaction at the scale of nucleosomal arrays in live cells, we performed a FRET-based assay that exploits multiphoton fluorescence lifetime imaging microscopy. FRET occurs between Fluorescent Protein-tagged histones on nucleosomes and is increased when chromatin compacts and the physical distance between nucleosomes is reduced. Interphase cells are characterized by multiple chromatin populations with several degrees of FRET efficiency ($E_{FRET}$) (e.g. low, medium, or high), which represent spatially distinct regions with
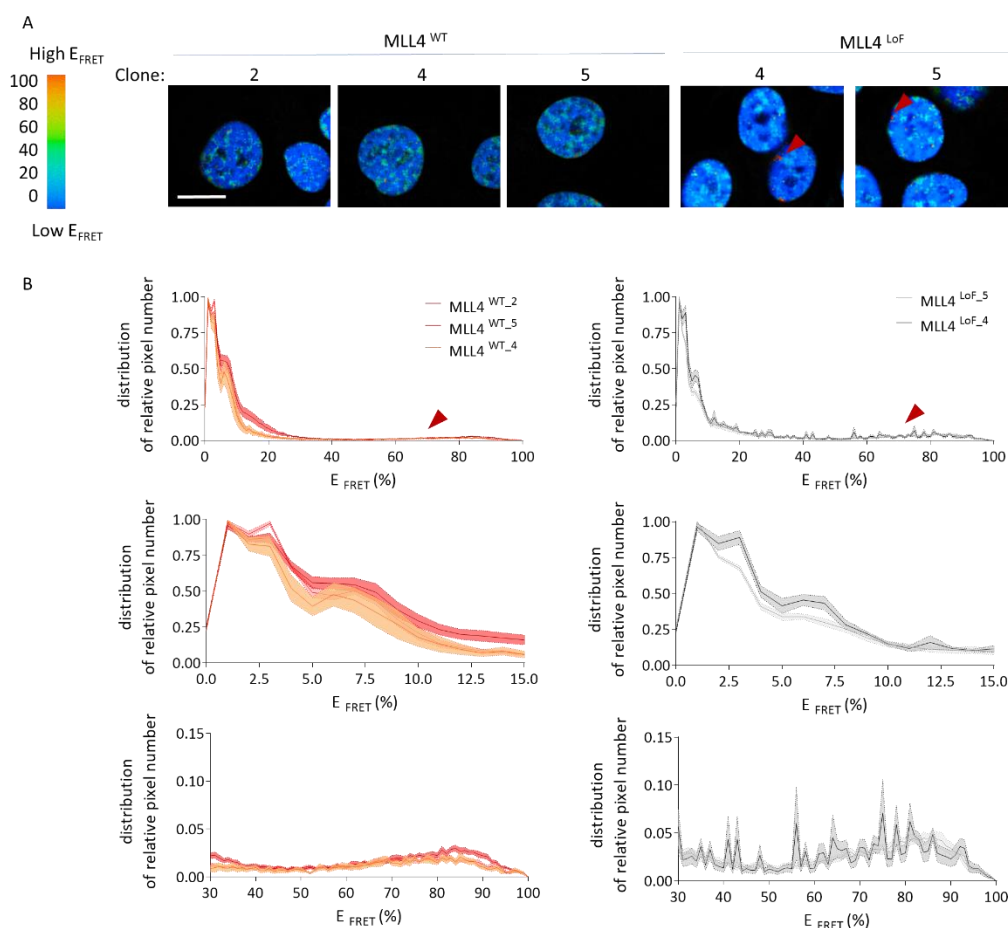
**Figure 25. Chromatin compaction measurements by FLIM FRET.** *A) $E_{FRET}$ (%) color- coded maps of MLL4^WT and MLL4^LoF H2B-2FPs clones. Red arrows indicate a high $E_{FRET}$ signal (scale bar 10μm; 3X zoom). B) Upper panel: distribution of relative pixel number (N° of pixels found in each $E_{FRET}$ category normalized on the n° of pixels of the most abundant $E_{FRET}$ category) over $E_{FRET}$ (%) (Mean +/-SEM; merge of at least 5 fields of view derived from 2 independent experiments, 80 ≤n cells≤ 160); lower panels: insights of the distribution of relative pixel number for the $E_{FRET}$ category 0-15 and 30-100 %.*

81

different levels of chromatin compaction (Llères *et al.*, 2009). As shown from the $E_{FRET}$ color-coded maps, we observed a higher $E_{FRET}$ signal at the periphery of MLL4 LoF nucleus, which is conceivable to represent some peripheral heterochromatin compartments attached to the nuclear envelope (Figure 25A). By looking at how pixels were distributed over $E_{FRET}$ we noticed the existence of at least two FRET chromatin populations in both cell types (Figure 25). The first population was comprised of 0-5 % $E_{FRET,}$ and it was represented by ~40% of pixels (AUC %, percentage of area under the curve); the second one was around 5-15 % $E_{FRET}$ and comprehended ~36% of pixels. By comparing the relative abundance of these two Low-FRET populations in the MLL4$^{WT}$ and MLL4$^{LoF}$ MSCs, we did not detect relevant differences. However, a third FRET sub-population (~11% of pixels) with higher $E_{FRET}$ (>30) was distinguishable specifically in MLL4$^{LoF}$ MSCs, possibly indicating a more compacted state of chromatin.

### 4.3.3 Chromatin compaction is tuned by substrate rigidity

To further investigate the effects of matrix stiffness on chromatin properties we analyzed by FLIM-FRET two H2B- 2FPs clones for MLL4$^{WT}$ and MLL4$^{LoF}$ MSCs at 0.5 and 32 kPa.

The distribution of the relative pixel number over $E_{FRET}$ (%) in MLL4$^{WT}$ MSCs showed a different pattern at 32 kPa with respect to what was observed in standard culture conditions, showing mainly one low-FRET chromatin population (0-15 % $E_{FRET}$), whereas MLL4$^{LoF}$ MSCs are characterized by three FRET chromatin sub-populations: 0-5 %, 5-15 % and 70-90 % $E_{FRET}$ (Figure 26). Interestingly, in MLL4$^{WT}$ MSCs (clone 2 and 4) at 0.5 kPa, a new peak appeared between 80-100% FRET, indicating a small subset of pixels (~16,8% AUC) with high-FRET exclusive of this condition (red arrows in Figure 26A and B). Even though MLL4$^{LoF}$ MSCs clone 4 and 5 did not present the same high-FRET peak (80-100% $E_{FRET}$) in the soft matrix, an increase in
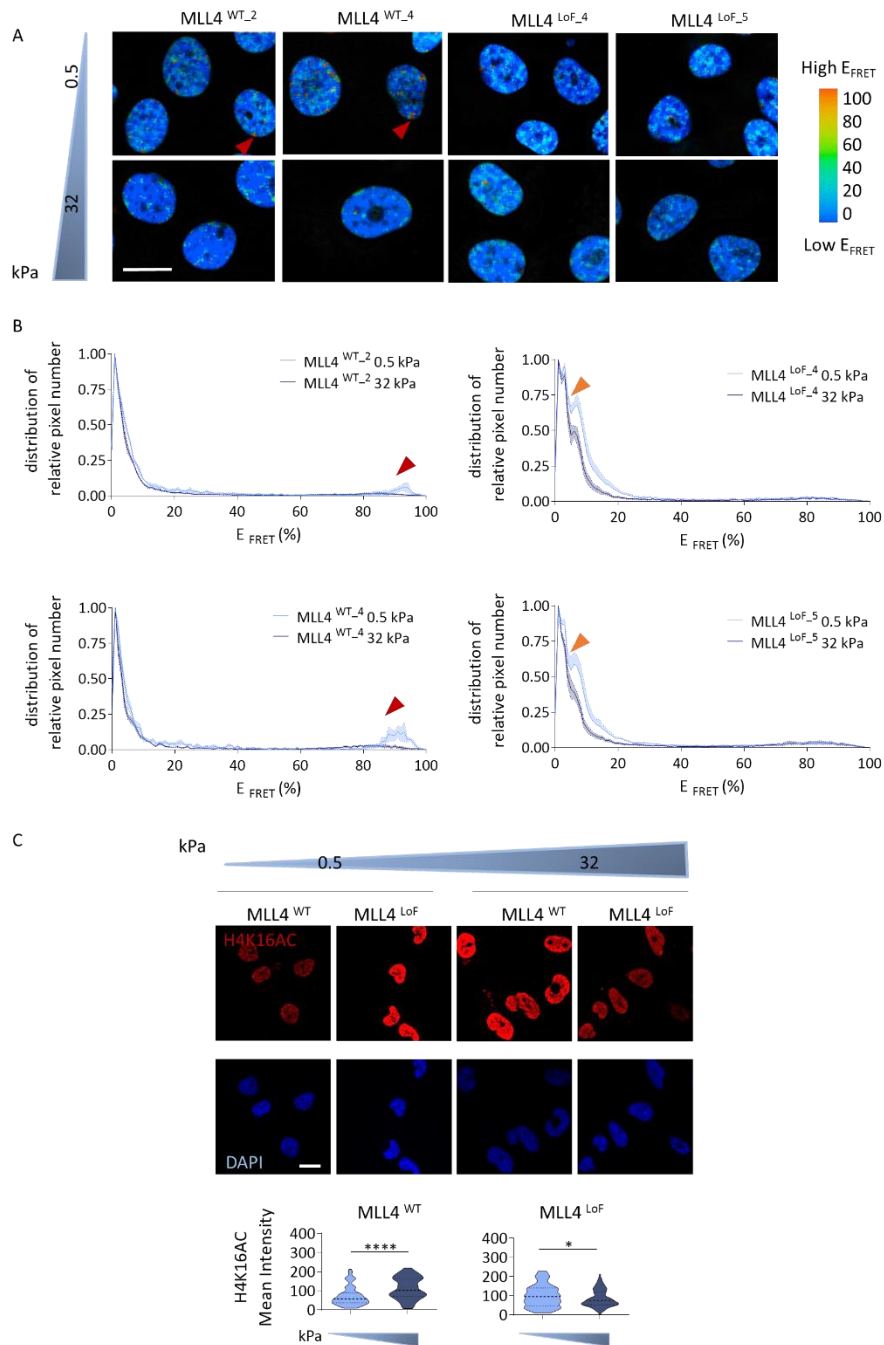
*Figure 26. Chromatin compaction is tuned by substrate rigidity. A) $E_{FRET}$ (%) color-coded maps of MLL4$^{WT\_2/4}$ and MLL4 $^{LoF\_4/5}$ H2B-2FPs clones at 0.5 and 32 kPa. Red arrows indicate a high $E_{FRET}$ signal. (scale bar 10µm; 3X zoom). B) Distribution of relative pixel number (N° of pixels found in each $E_{FRET}$ category normalized on the n° of pixels of the most abundant $E_{FRET}$ category) over $E_{FRET}$ (%) (Mean +/-SEM; merge of at least 5 fields of view derived from 2 independent experiments, 50 ≤n cells≤ 66). Orange arrows highlight the 5-10% $E_{FRET}$ sub-population. C) Representative images of H4K16AC Immunostaining in MLL4$^{WT}$ and MLL4$^{LoF}$ (scale bar 10µm; 2X zoom). Below, nuclear mean intensity quantification is shown (80 ≤n≤ 156). Two-tailed unpaired Student's t-test was performed.*

the relative pixel number between 5-15% $E_{FRET}$ was detectable (orange arrows in Figure 26B).

1534

These results indicate that substrate rigidity can affect chromatin compaction. We noticed the presence of condensed chromatin at 0.5 kPa, in line with our observation of an increased PcG abundance in the same condition. Again, *KMT2D* haploinsufficiency impairs chromatin compaction driven by matrix stiffness. To confirm these data, we performed an immunostaining against H4K16AC in MLL4[WT] and MLL4[LoF] MSCs not over-expressing H2B-2FPs (Figure 26C). In MLL4[WT] MSCs, the increased chromatin condensation that was detectable by FLIM-FRET in the soft matrix was associated with a lower level of H4K16ac, a histone modification that modulates higher order chromatin architecture by inducing chromatin decompaction (Shogren-Knaak *et al.*, 2006).

For the MLL4[LoF] MSCs, we registered a slight increase of the H4K16ac nuclear signal at 0.5 kPa with respect to 32 kPa, suggesting more accessible chromatin states in the soft matrix.

In sum, quantification of the percentage of H2B-H2B FRET efficiency in MLL4[WT] MSCs indicated that substrate rigidity affects chromatin compaction, leading to an increased high-FRET chromatin population at 0.5 kPa with respect to the stiff matrix, which is absent in MLL4[LoF] MSCs in the same condition.

## 4.4 Analysis of nuclear deformation in microchannels with restrictions

The nuclear envelope (NE) is a physical barrier that separates the chromatin from the cytoplasm, and its integrity is a pre-requisite to protect the genome integrity. However, there are pathological circumstances in which NE rupture takes place in interphase. For example, pathologies associated with mutations in genes coding for nuclear lamina proteins, in particular LAMIN A/C, fall into this category (Malashicheva and Perepelina, 2021). Considering that the *KMT2D* haploinsufficiency affects not only chromatin compartments but also nuclear stiffness and LAMIN A/C level, we were intrigued to understand whether MLL4 LoF could influence nuclear deformation capacity and cell survival rate. Hence, we

followed the migration of MSCs in microchannels with constrictions that provide an

1566 impediment to cell migration and eventually promote NE breakage.

1568

### 4.4.1 MLL4$^{LoF}$ MSCs undergo NE rupture and cell death with a higher percentage with respect to MLL4$^{WT}$ MSCs

1570 To study nuclear deformation capacity, we used microchannels with

restrictions of different widths (2, 3 and 5 μm) and a height of 5 μm, in

1572 which cells can migrate bi-directionally. Restrictions ranging from 2 to 5

μm widths represent a mechanically restrictive environment in which

1574 MSCs are expected to deform their nuclei (nuclear diameter = 10 μm).

Interestingly, in vitro reconstitution of collagen matrices derived from rat

1576 tendons or bovine dermis demonstrated that the fibrillar collagen

architecture is characterized by narrow pores whose size ranges from 1 to

1578 6 μm in diameter (Wolf et al., 2013). Furthermore, during the process of

transmigration through the endothelial barrier, tumor cells have been

1580 shown to deform their nucleus to overcome the gaps of ~1–8 μm which

are present in the blood vessels (Chen et al., 2013). On the basis of these

1582 observations, the widths of the restrictions were chosen in a size range

that cells might encounter in physiological conditions (2- 5 μm). To

1584 investigate nuclear deformation, we performed time-lapse imaging for 15

hours using as a reporter the expression of GFP fused to a nuclear

1586 localization signal (GFP-NLS). This biosensor allows assessing nuclear

integrity. Indeed, cytoplasmic accumulation of GFP-NLS indicates NE

1588 rupture (Figure 27A). Specifically, if NE rupture occurs in correspondence

with the constriction, the NLS fluorescent signal is not confined to the

1590 nucleus anymore and diffuses into the cytosol. In this case, it is possible to

quantify this event as the Cytoplasm/Nucleoplasm ratio. In case of NE

1592 breakage because of the transient nuclear deformation for the cellular
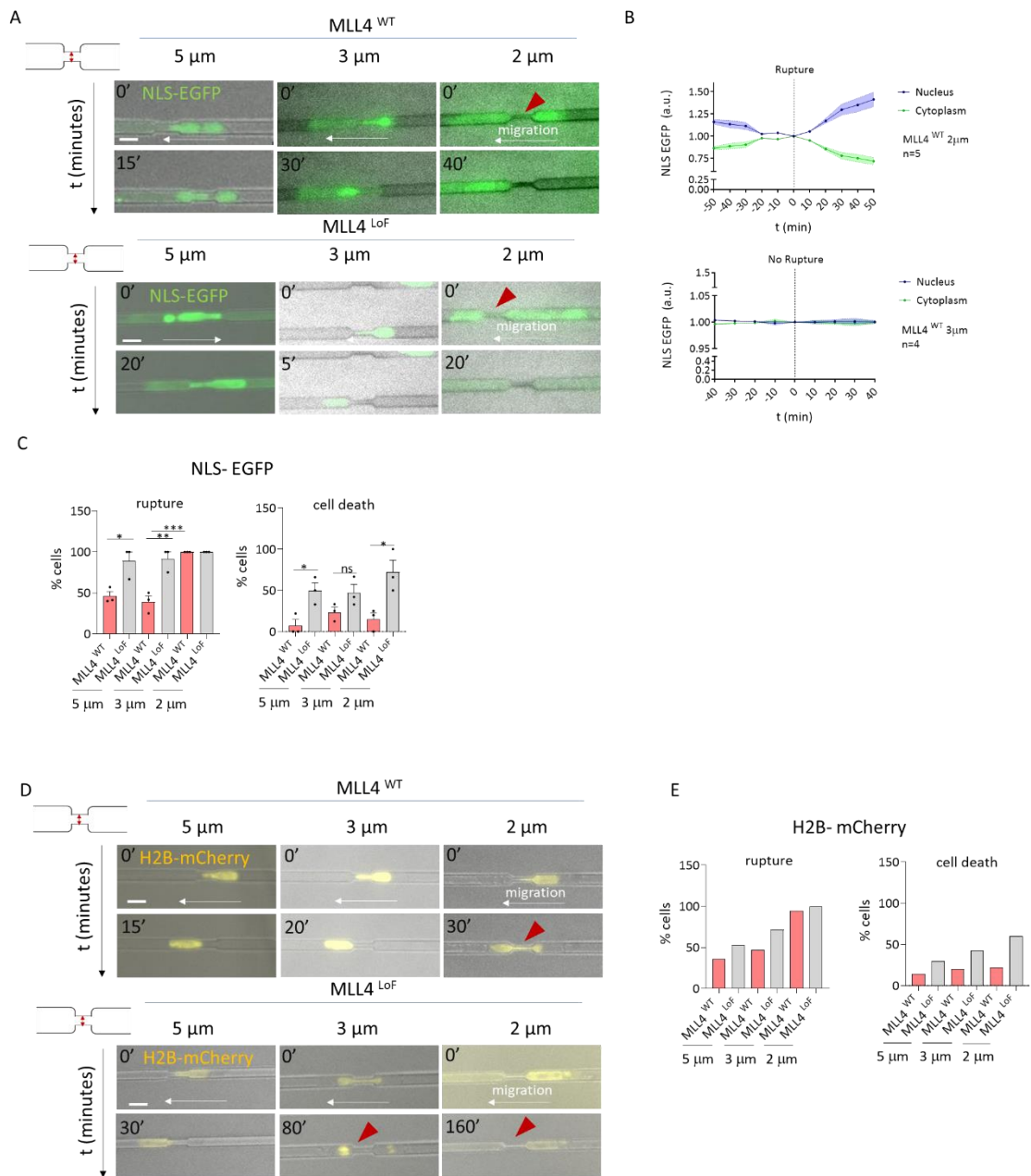
*Figure 27. MLL4^LoF undergoes NE rupture and cell death with a higher percentage with respect to MLL4^WT.*
*A) Representative images of MLL4^WT and MLL4 ^LoF NLS-EGFP in the process of passing through restrictions of different widths at the indicated time points (scale bar 10μm). The white arrows indicate the direction of migration, the red arrow highlights a nucleus undergoing NE rupture. B) NLS-EGFP normalized mean intensity inside the nucleus (blue) and in the cytoplasm (green) of MLL4^WT in case of NE rupture (2 μm; upper panel) or not (3 μ; lower panel) (Mean +/-SEM). To obtain NLS nuclear or cytosolic signal, cytoplasmatic NLS-EGFP intensity was normalized to initial nuclear intensity and vice-versa. Time equal to 0 (x axis) corresponds to the tip of the nucleus reaching the end of the constriction in which NE rupture occurs. C) Bar plots showing the % of cells undergoing NE rupture and cell death in NLS EGFP- MSCs (Mean +/-SEM, merge of three independent experiments). One-tailed unpaired Student's t-test was performed. D) Representative images of MLL4^WT and MLL4^LoF H2B-mCherry in the process of passing through restrictions of different widths at the indicated time points (scale bar 10μm). E) Bar plots showing the % of MLL4^WT and MLL4^LoF H2B-mCherry cells undergoing NE rupture and cell death (single experiment).*

passages through the restriction, the Cytoplasm/Nucleoplasm ratio of the

| 1594 | NLS-EGFP increases (Figure 27B). By quantifying the percentage of NE rupture in three independent biological replicates we observed that MLL4$^{LoF}$ MSCs were more subjected to nuclear membrane breakdown with respect to MLL4$^{WT}$ MSCs at 5 and 3 μm, whether at the extreme constriction of 2 μm the two cell lines endured this event with the same magnitude (Figure 27C). We noticed that a consistent fraction of these cells died during this process, not being able to succeed in overcoming the restriction (e.g. MLL4$^{LoF}$ MSCs at 2 μm, 90' in Figure 27A). We observed a significant increase of cell death in MLL4 LoF cells with respect to the WT cells in all the analyzed conditions, yet with a certain level of variability. Indeed, although the same trend is observed at 3 μm, the differences between WT and MLL4 LoF MSCs were not statistically significant, probably due to high variability between replicates (Figure 27C). For strengthening these results, we used H2B-mCherry as an independent biosensor of NE integrity in MSCs undergoing mechanical constrain. Although in a single replicate, we observed that MLL4$^{LoF}$ MSCs underwent NE rupture and cell death more frequently than MLL4$^{WT}$ MSCs (Figure 27D and E), corroborating the previous results. Overall, these findings indicated that MLL4$^{LoF}$ MSCs undergo NE rupture and cell death with a higher percentage with respect to MLL4$^{WT}$ MSCs. |

## 4.4.2 Increased NE rupture in MLL4$^{LoF}$ MSCs is rescued by K27M overexpression

By rescuing PcG activity through the overexpression of H3.3 K27M in MLL4$^{LoF}$ MSCs we could restore the level of NE rupture in the constrictions of 5 and 3 μm of widths. As shown in Figure 28B, MLL4$^{LoF}$ MSCs expressing the WT variant H3.3 showed a higher percentage of NE breakdown with respect to K27M- transduced cells. These results suggest that the alteration of chromatin compartmentalization caused by the unbalancing of PcG and TrxG-associated compartments influences the nuclear deformation capacity of MSCs. Of note, the contribution of chromatin

The line numbers in the left margin are 1616, 1618, 1620, 1622.

organization resulted in being dependent on the level of nuclear deformation as forcing cells through a constriction of 2µm caused NE

rupture in most of the analyzed cells, independently from the chromatin context. Although MLL4$^{LoF\ H3.3\ K27M}$ MSCs showed a decrease in the

percentage of cells that die while passing through the constrictions with respect to the control (H3.3wt), the difference observed resulted to be not

statistically significant. Nevertheless, the observed correlation between the frequency of NE rupture and cell death with respect to the increased
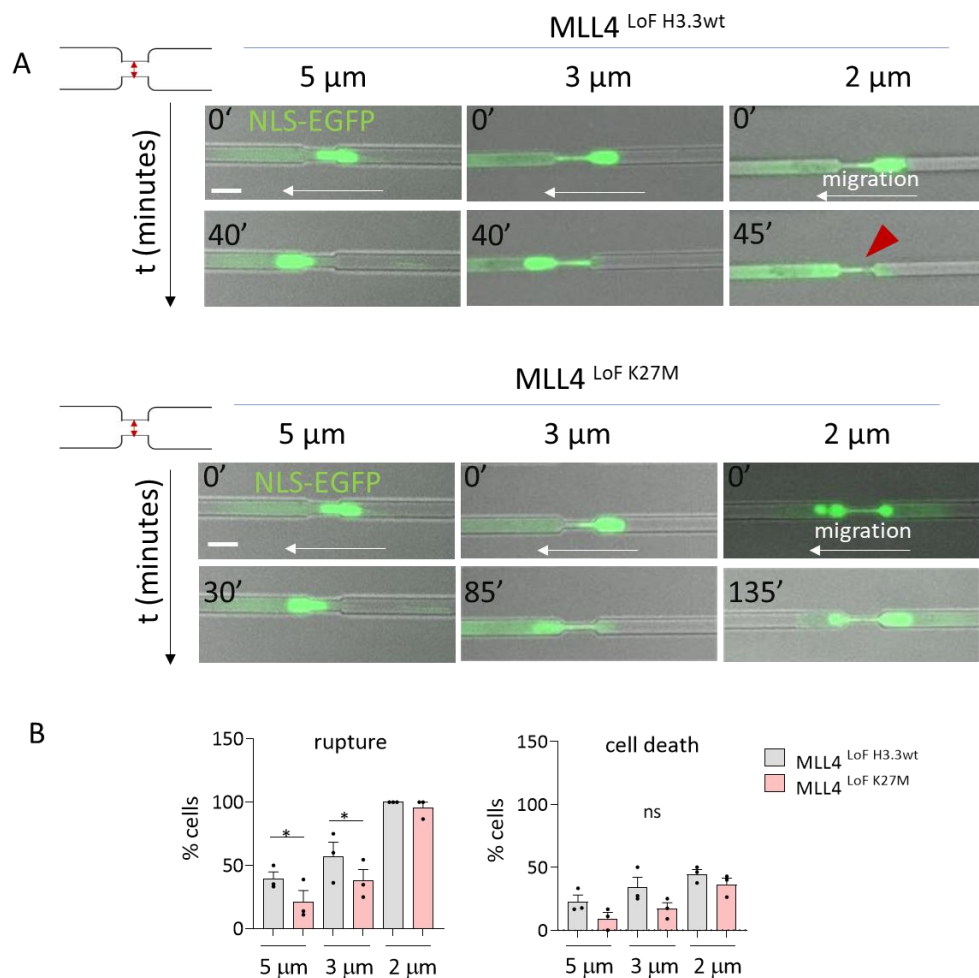


*Figure 28. Increased NE rupture in MLL4$^{LoF}$ is rescued by K27M overexpression. A) Representative images of MLL4$^{LoF\ H3.3wt}$ and MLL4$^{LoF\ H3.3\ K27M}$ - NLS-EGFP in the process of passing through restrictions of different widths at the indicated time points (scale bar 10µm). The white arrows indicate the direction of migration; the red arrow highlights a nucleus undergoing NE rupture. B) Bar plots showing the % of cells undergoing NE rupture and cell death (Mean +/-SEM, merge of three independent experiments). One-tailed unpaired Student's t-test was performed.*

level of nuclear deformation indicates that the PcG-mediated chromatin

compartmentalization contributes to define the nuclear mechanical
properties.

## 4.5 Physical confinement: another tool for studying cell deformability and survival

We observed that MLL4$^{LoF}$ MSCs undergo cell death with a higher percentage with respect to MLL4$^{WT}$ MSCs in microchannels with restrictions of different widths. Consequently, we sought to use another mechanical device to further confirm MLL4$^{LoF}$ nuclear fragility under a different type of physical cue: static confinement. We followed by live imaging MSCs confined at 3 and 6 µm after being stained with Hoechst and SirActin to mark nuclei and actin, respectively (Figure 29). Interestingly, we noticed in MLL4$^{WT}$ MSCs the formation after 2 hours of confinement of ring-like structure in the cytoskeleton, suggesting actomyosin recruitment to the cortex, under 3 and 6 µm heights of confinement (yellow arrows in Figure 29A), in accordance with previous works (Le Berre, Aubertin and Piel, 2012). Quantification of the nuclear area showed that confined nuclei shrunk over time with respect to the control (not confined cells) (Figure 29B). Actomyosin recruitment to the cortex was observed in MLL4$^{LoF}$ MSCs when confined under 6 µm, with no dramatic changes in nuclear area. Of note, already after 20 minutes of confinement at 3 µm, MLL4$^{LoF}$ MSCs were visibly in a diminished number and suffering, showing membrane blebbing and rupture. Unfortunately, due to technical reasons, we could not follow the first 20 minutes of confinement, hence we are not aware of the specific form of cell death that occurred nor the processes that took place before this time. However, MLL4$^{LoF}$ MSCs confined at 3 µm showed a phenotype consistent with cell stress and characterized by increased cell mortality, which is absent in MLL4$^{WT}$ MSCs. These results, together with the previous ones, suggest that MLL4 LoF alters nuclear capacity to deal with confined spaces by incrementing nuclear fragility and susceptibility to nuclear membrane breakage.
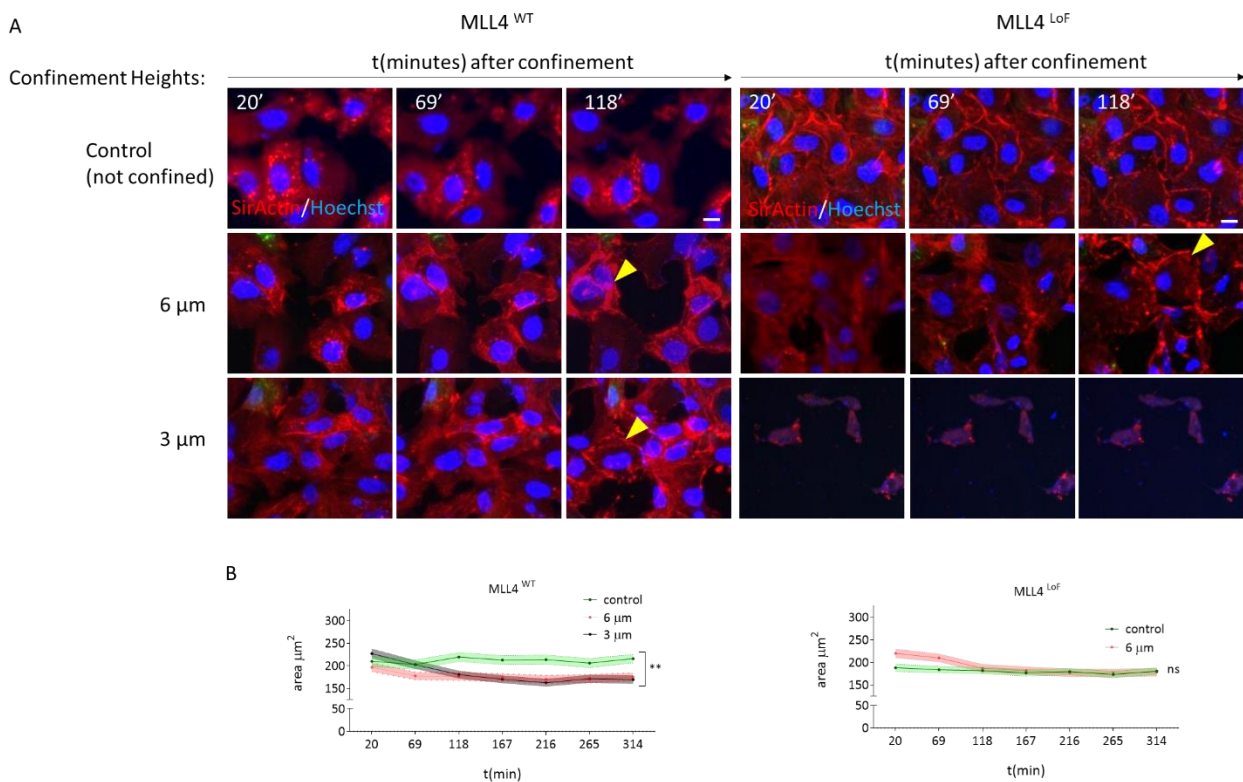
***Figure 29. MLL4 LoF increases nuclear fragility to physical confinement.*** *A) Representative images of MLL4[WT] and MLL4 [LoF] stained with Hoechst and SirActin at the indicated heights of confinement and time points (scale bar 10μm). Yellow arrows show the actomyosin cortex. B) Quantification of the nuclear area over time (x-axis) (Mean +/-SEM, 150 ≤n≤ 350).*

## 4.6 NE tension investigation by MiniNesprin1-cpstFRET sensor

Quantification of nuclear nesprin signal showed that MLL4[LoF] nuclei have increased NE perimeter at the steady state with respect to MLL4[WT] MSCs. Furthermore, analysis of the of NE rupture in a state of deformation showed that MLL4[LoF] nuclei had increased nuclear membrane rupture compared to MLL4[WT] MSCs. In the attempt to understand whether these observations could be coupled to changes in NE tension, we investigated nuclear rigidity by taking advantage of orientation-based FRET biosensor (circularly permutated stretch sensitive -cpst) that uses the N-terminus and C- terminus of Nesprin-1 protein, part of the LINC complex, as backbone (Figure 30A).

This FRET biosensor has been recently developed by Alessandro Poli and it was designed to be modulated by the angles between the donor (cpst Cerulean) and

90

acceptor (cpst Venus) rather than by the distance between them (Poli *et al.*, 2022).

1674 If the probes are physically parallel one respect to the other, the level of FRET is high, indicating that there is negligible mechanical stress on the nucleus and the NE

1676 is relaxed (Poli *et al.*, 2022) (Figure 30A). However, when the NE is under tension, the position of the donor with respect to the acceptor is altered, and the level of

1678 FRET decreases dependently on the amplitude of the angle formed between the cpstFRET probes (Θ) (Figure 30A). As shown in Figure 30B, MLL4[LoF] nuclei have a
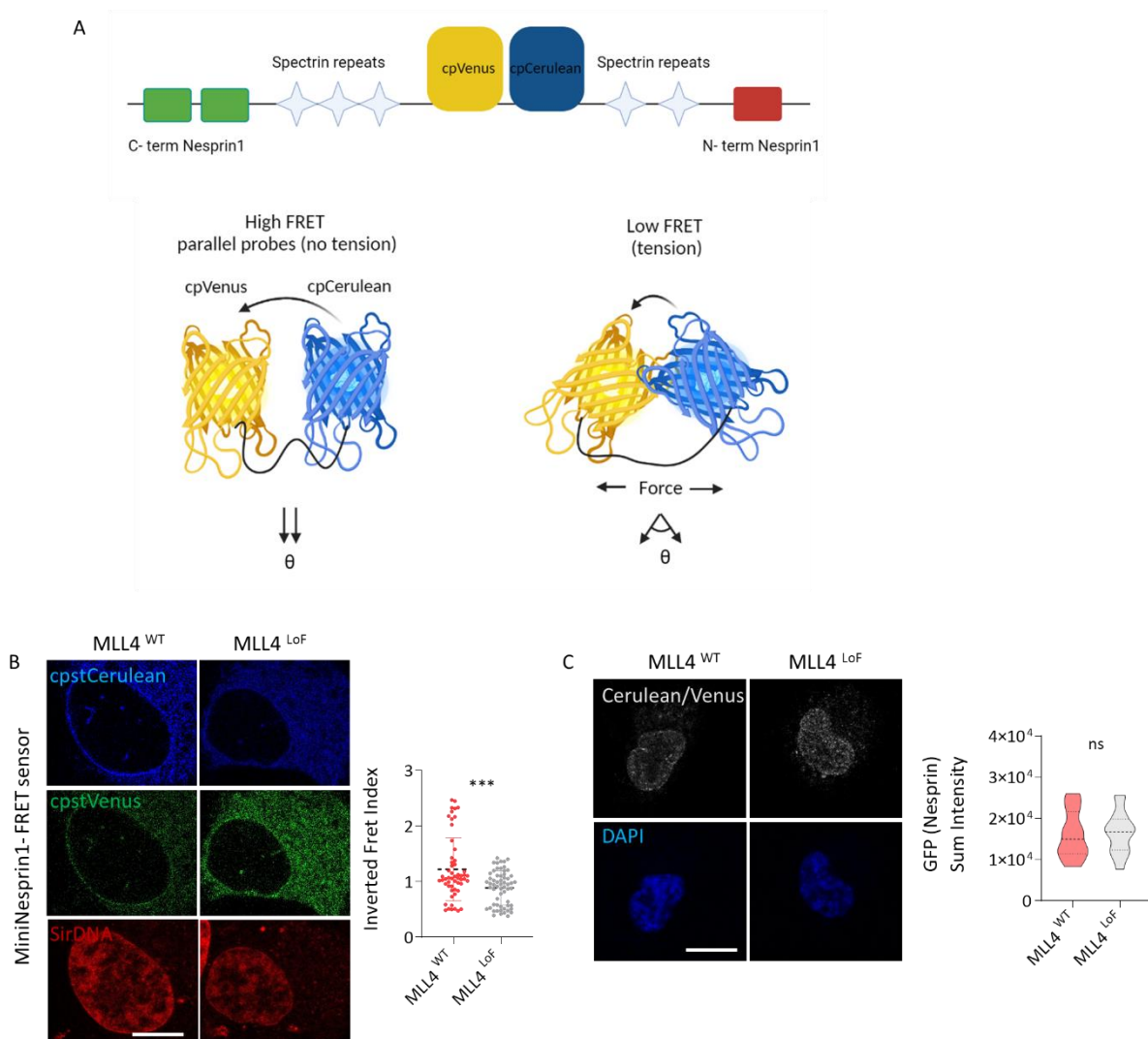


***Figure 30. MLL4 LoF affects NE tension.*** *A) Graphical representation of Mini Neprin 1 cpst-FRET sensor (top) and working mechanism (bottom). Illustration created with BioRender. B) Representative images of cpstCerulean, cpstVenus in MLL4[WT] and MLL4[LoF] - MiniNesprin1-cpstFRET stained with SirDNA (scale bar 5µm). Donor (cpstCerulean) was excited at 458 nm and emission peaks of cpCerulean and cpVenus were captured, respectively, in a window of 470-490nm and 520-540nm. On the right, scatter plot (Mean +/-SD, merge of four independent replicates, n≥60) showing the Inverted FRET index. C) Representative images of the Immunostaining of cpstCerulean/ cpstVenus catched by using anti-GFP primary antibody (scale bar 10µm). On the right, violin plot of the GFP nuclear intensity signal. Two-tailed unpaired Student's t-test was performed.*

1680 higher level of FRET (lower Inverted FRET index) with respect to MLL4$^{WT}$ MSCs. This means that MLL4 LoF affects NE tension leading to more relaxed nuclei. Reasonably,

1682 this may also be compatible with the fact that MLL4$^{LoF}$ MSCs have decreased level of LAMIN A/C.

1684 To exclude that the differences observed in the NE tensional state between MLL4$^{WT}$ and MLL4$^{LoF}$ MSCs could be due to dissimilar levels of expression of the cpstFRET

1686 probes between the two cell types, we performed an immunostaining against Cerulean and Venus by using an anti-GFP antibody, which recognizes both proteins.

1688 Of note, to avoid the stimulation of either the acceptor or the donor, the immunofluorescent signal was detected by using a secondary antibody conjugated

1690 with Alexa 647. The obtained results (Figure 30C) showed that MLL4$^{WT}$ and MLL4$^{LoF}$ MSCs have a comparable level of expression of cpstFRET probes, indicating that the

1692 nuclear relaxation observed in MLL4 LoF is merely due to changes in NE tensional state.

1694

## 4.7 MLL4 LoF influences MSCs migratory capacity

1696 The microchannels with restrictions, besides being a useful tool for studying nuclear deformation, also provide information about cell migration. By using less stringent

1698 constrictions (MC011) which do not cause relevant NE rupture (7, 5, and 3 µm widths with a height of 10 µm) we noticed that MLL4$^{LoF}$ MSCs were able to go

1700 through the restrictions more rapidly than MLL4$^{WT}$ MSCs. Thus, we measured the residence time in the restrictions of MLL4$^{WT}$ and MLL4$^{LoF}$ - NLS-EGFP MSCs (including

1702 MLL4$^{LoF}$ overexpressing H3.3wt and H3.3K27M), by measuring the interval of time (n° of frames) that MSCs require to migrate from end to end of the restrictions ($t_1$ -

1704 $t_{final}$) (Figure 31B). This quantification showed that MLL4$^{LoF}$ MSCs were able to overcome the restrictions faster than MLL4$^{WT}$ MSCs (Figure 31C). Interestingly, the

1706 velocity of migration is rescued by overexpressing the K27M histone variant, while MLL4$^{LoF\ H3.3wt}$ MSCs behave similarly to the parental cell line. Of importance, the

1708 measured differences were maintained in all the tested conditions, irrespective of the level of restriction widths, which instead contributed to determine the residence
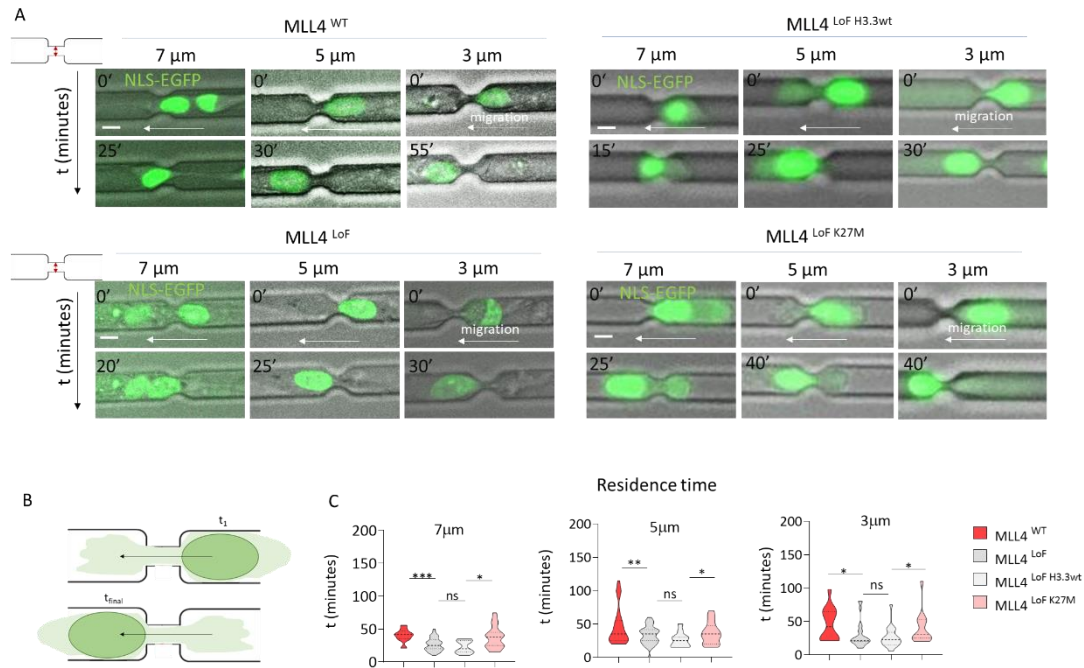
*Figure 31. MLL4 LoF influences MSCs time of residence.* A) *Representative images of MLL4$^{WT}$, MLL4 $^{LoF}$, MLL4 $^{LoF\ H3.3wt}$ and MLL4 $^{LoF\ H3.3\ K27M}$ - NLS-EGFP before and after passing through restrictions of different widths at the indicated time points (scale bar 10μm). The white arrows indicate the direction of migration. B) Graphic illustration describing how t$_1$ and t$_{final}$ were identified. C) Quantification of the velocity of migration through the constrictions (residence time) (15 ≤n≤ 30). One-tailed unpaired student's t-test was performed.*

1710      time. In order to confirm these observations with an independent technique, we performed a migration assay in collagen-coated transwells with polycarbonate

1712      membranes harboring pores of different sizes (5, 8 and 12μm) (Figure 32). By quantifying the number of cells that migrated through the pores towards a

1714      chemoattractant after 8 and 24h from seeding, we found that in comparison to MLL4$^{WT}$ MSCs, MLL4$^{LoF}$ MSCs were characterized by a higher percentage of

1716      migrating cells in membranes with pores of 5 or 12 μm (Figure 32B). Although this phenotypic assay shows a certain level of intrinsic variability, we were able to assess

1718      a trend of a higher level of migrating cells in MLL4$^{LoF}$ MSCs with respect to MLL4$^{WT}$ MSCs in all the tested conditions; nevertheless, only replicates obtained at the pore

1720      size of 5 or 12 μm showed statistical significance, thus increasing the number of replicates could strengthen this observation in all settings. We then asked whether

1722      the higher migratory capacity of MLL4LoF MSCs could depend also on non – chromatin-related factors. Indeed, during migration, cells use focal adhesions (FA)

1724      to apply traction forces on the ECM (Rape, Guo and Wang, 2011). Therefore, we

sought to investigate one of the membrane-cytoskeletal proteins involved in FA

1726 plaques. Of note, vinculin plays key functions in the maintenance of FA, which exerts

by linking adhesion receptors (e.g. integrins) to the contractile actin-myosin

1728 cytoskeleton, thus building a physical connection for transmitting forces between

the cytoskeleton and the ECM (Humphries et al., 2007). Hence, by

1730 Immunofluorescence, we quantified the number and the abundance of FA, as well

as their area in MLL4$^{WT}$ and MLL4$^{LoF}$ MSCs (Figure 33). We found that MLL4$^{LoF}$ MSCs

1732 were characterized by a higher number of FA per cell, which resulted in being larger

and more abundant in comparison with MLL4$^{WT}$ MSCs (Figure 33 B-D). Overall, this

1734 analysis suggested that MLL4 LoF impairs vinculin-mediated focal adhesions.
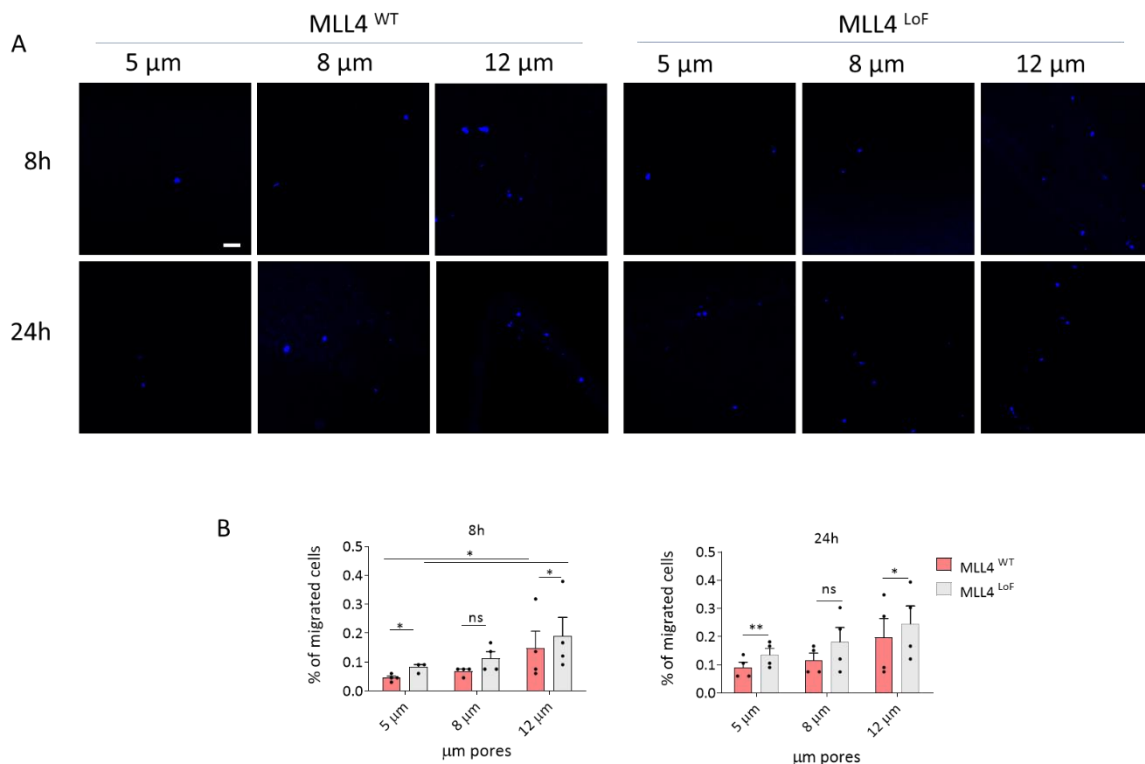


Figure 32. MLL4 LoF impacts MSCs migratory capacity. A) Representative images of the DAPI signal of membrane bottom attached MSCs (scale bar 20µm). B) Quantification of the percentage of migrating cells (attached to the lower part of the membrane) relative to the number of seeded cells (merge of 4 biological replicates). One-tailed unpaired student's t-test.

Nonetheless, further experiments are required to clarify the single contributions of

1736 the altered cytoskeletal and nuclear structures to MLL4$^{LoF}$ MSCs migratory capacity.

For instance, the overexpression of the dominant negative Nesprin–KASH protein,

1738 which interferes with the formation of a functional LINC complex, could clarify

94

whether the migratory phenotype observed is coupled to the altered nuclear
mechanics caused by MLL4 LoF.
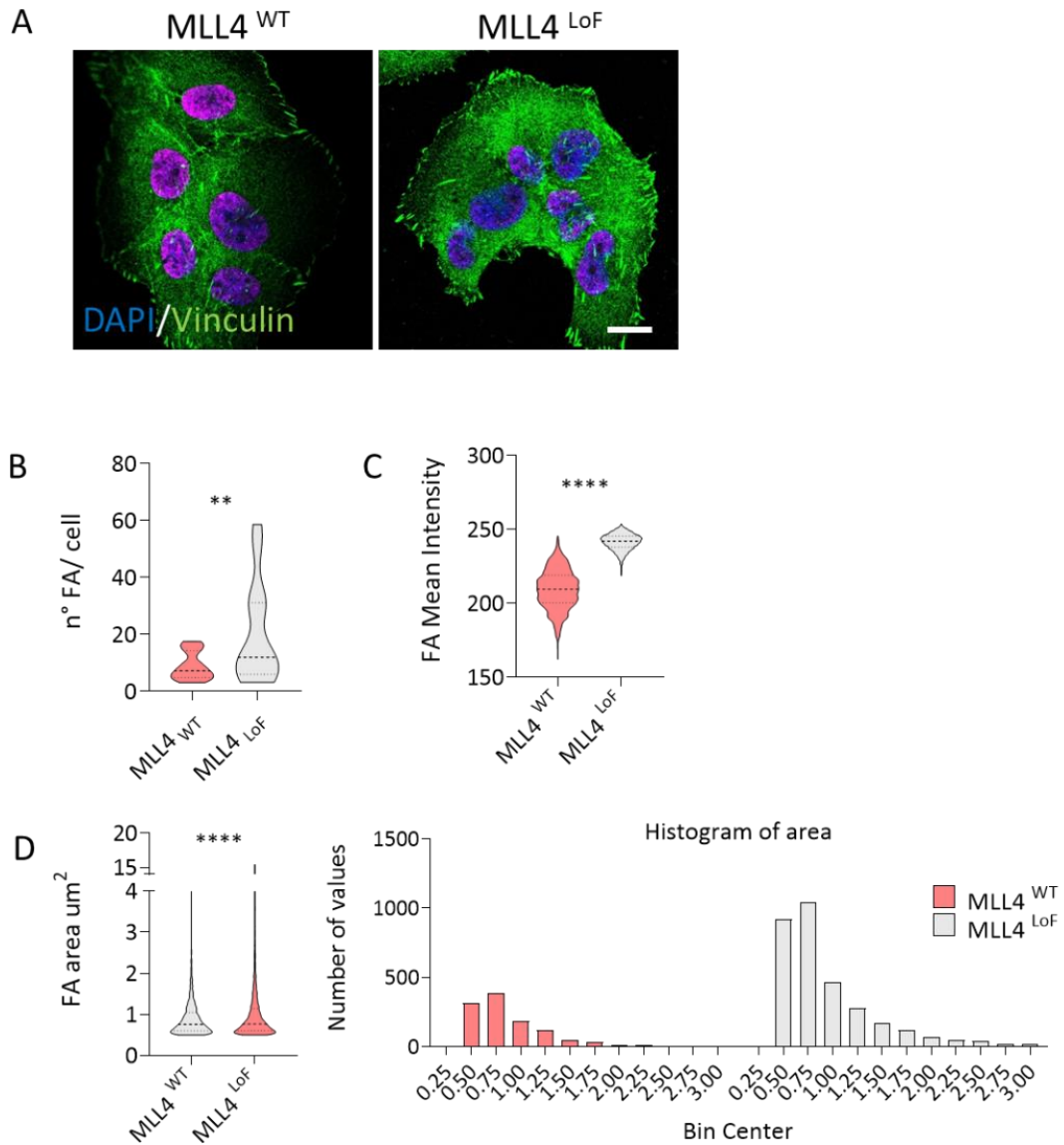


*Figure 33. Analysis of vinculin-mediated focal adhesions. A) Merged confocal images of Vinculin (green) and DAPI (blue) in MLL4^WT and MLL4 ^LoF (scale bar 10µm). B-C) Quantification of the n° of FA per cell and FA Mean Intensity. D) Quantification of FA area. The histogram of area highlights the distribution of FA among specific values of area (bin center). N≥14 field of views. Two-tailed unpaired student's t-test was carried out.*

# 5. Discussion

1744     Mechanical forces regulate cell structure and function.  A growing amount of evidence suggests that the genome participates in determining the mechanical

1746     properties of the nucleus, which are essential for cells to sense forces and transduce them into biochemical signals that impact several cellular responses (Bustin and

1748     Misteli, 2016; Lomakin *et al.*, 2020; Venturini *et al.*, 2020). However, the exact process by which chromatin remodelling occurs in response to mechanical stimuli

1750     has remained elusive.

    In Fasciani *et al.*, we demonstrated that MLL4 chromatin-binding protein maintains

1752     the equilibrium between Transcriptional and PcG condensates. The balancing between these chromatin compartments is required for preserving nuclear

1754     mechanical properties in a MSCs-based Kabuki Syndrome disease model carrying a frameshift mutation in the *KMT2D* gene (MLL4 LoF).

1756     Interestingly, MLL4 impacts on MSCs differentiation program, interfering with their commitment towards chondrocytes and osteocytes, indicating a connection

1758     between MLL4 LoF and KS symptoms, such as facial dysmorphisms, skeletal abnormalities, and postnatal growth retardation, affecting bone and cartilage

1760     tissues. Overall, these findings suggest an interplay between nuclear condensates and nuclear mechanics and architecture.

1762

    In the present study, we investigated the role of Transcriptional and PcG

1764     condensates in regulating nuclear responses to external mechanical stimuli. We provided data supporting the knowledge that the balancing between repressive and

1766     active chromatin compartments affects nuclear mechanics under different mechano-physical conditions. In particular, we showed that Transcriptional and PcG

1768     condensates are responsive to changes in substrate stiffness and that MLL4 LoF impairs the mechanical nuclear condensates-driven response. By assessing the

1770     effect of MLL4 haploinsufficiency on nuclear deformation capacity in microchannels with constrictions we also found that the unbalancing between Transcriptional and

1772     PcG condensates increases the susceptibility to nuclear envelope rupture and cell

death. Furthermore, the increased nuclear fragility in MLL4$^{LoF}$ MSCs is accompanied

1774    by an alteration of cell migratory capacity.

Altogether our findings suggest that active and repressive nuclear condensates

1776    orchestrate cell mechanoresponsiveness to external mechanical cues. Importantly, MLL4 LoF alters cell responses to mechanical stimuli, strengthening the role of MLL4

1778    in the maintenance of nuclear mechanics.


## 5.1 MLL4-PrLD phase separation

1780

After proving by in vitro Droplet- formation Assay that MLL4 IDR (Prion-like domain)

1782    is able to phase-separates, we took advantage of the OptoIDR inducible system to characterize MLL4-PrLD phase separation in living cells. We showed that MLL4-PrLD

1784    forms phase-separated droplets upon stimulation in MSCs (Figure 13), whose number decreases within 15 minutes. Clusters size, instead, slightly increases over

1786    the same period. Basic thermodynamics explains that after an initial nucleation phase, the growth and evolution of droplets is driven by the minimization of droplets

1788    surface area. This process can be guided by Brownian motion-driven coalescence, wherein droplets diffuse and merge after collision, or by Ostwald ripening, wherein

1790    molecules diffuse from small condensates to large ones (Lee, Strom and Brangwynne, 2022). Either way, this could explain why we observed after 15

1792    minutes a tendency for smaller clusters to fuse into the bigger ones, resulting in the retention of large clusters and the disappearance of the small ones (Figure 13).

1794    We also showed that MLL4-PrLD phase separation is impaired in MLL4$^{LoF}$ MSCs, with condensates that are smaller and fewer with respect to the ones formed by MLL4$^{WT}$

1796    MSCs (Figure 14). This could be due to multiple factors; for instance, the evidence that MLL4$^{LoF}$ MSCs have half amount of the MLL4 protein (Fasciani *et al.*, 2020) could

1798    influence the phase separation behavior of its over-expressed PrLD, as there is overall less protein available to overcome the C$_{critical}$ needed to clusterize (Figure 4).

1800    Furthermore, other components of the COMPASS complex, such as UTX, are reduced as consequence of MLL4 LoF. Of note, it has been demonstrated that UTX

1802    undergoes phase separation and participates to the assembly of the Transcriptional

97

condensates (Shi *et al.*, 2021). Other aspects may be related to the different chromatin contexts of MLL4[LoF] MSCs with respect to MLL4[WT] MSCs; indeed, MLL4[LoF] MSCs have reduced amount of H3K27ac, which could influence condensates assembly.
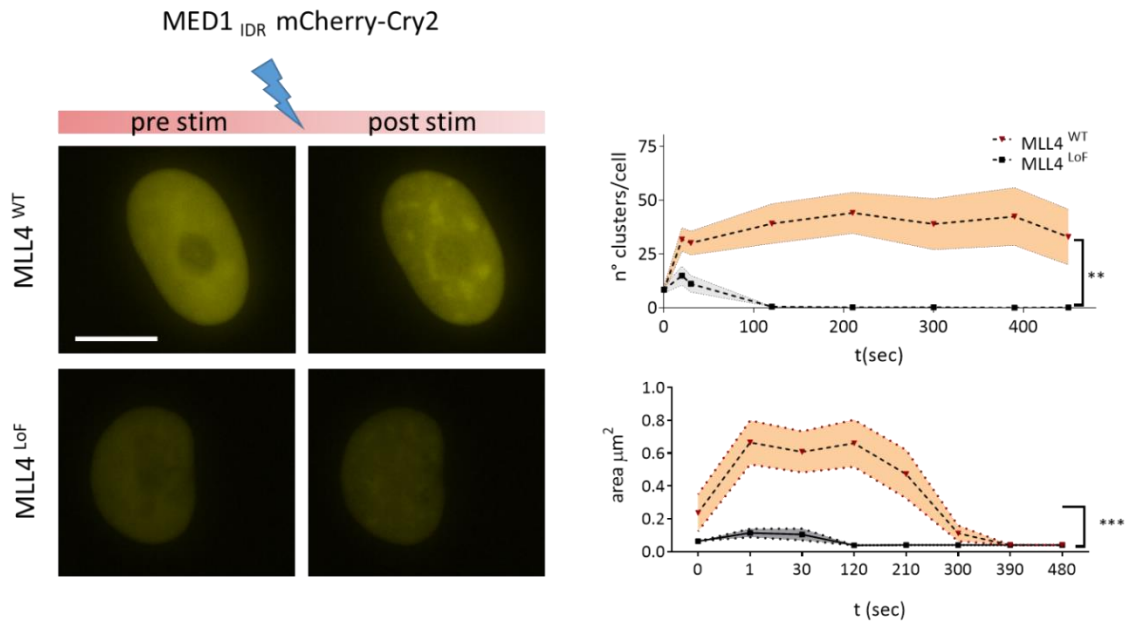


*Figure 34. MED1[IDR] phase separation (OptoIDR System).* On the left: representative images of MLL4[WT] and MLL4[LoF] before and after stimulus; scale bar, 10µm. On the right: quantification of the number (up) and area (down) of light-induced droplets of MED1-IDR (y axis) at different time points (x axis) (n≥6, Mean +/-SEM). The time point t=0 represents the pre-stimulus, t=1 the post-stimulus. One-way ANOVA test was performed.

The physical properties of the nucleus could affect the phase separation behavior of condensates as well. Indeed, the highly viscoelastic chromatin network can impact the formation of condensates, that preferentially form in softer environments (chromatin-poor regions) (Lee, Strom and Brangwynne, 2022). Interestingly, MLL4[LoF] MSCs are characterized by a stiffer nucleus with a more compacted chromatin, as shown by Brillouin Microscopy (Fasciani *et al.*, 2020) and confirmed by the analysis of nucleosome- nucleosome interactions through FLIM-FRET experiments (Figure 25). A more condensed chromatin could limit the diffusion and growth of MLL4 protein, thus impacting the formation of condensates. This hypothesis is strengthened by the observation that the rescue of PcG level in MLL4[LoF] MSCs by K27M overexpression partially restores MLL4-PrLD cluster formation in mutant cells (Figure 15).

As proof of concept, we compared in MLL4$^{WT}$ and MLL4$^{LoF}$ MSCs the phase separation behavior of the IDR of another protein which is part of the Transcriptional condensates and is downregulated in MLL4 LoF: MED1 (Figure 34). MED1-IDR forms fewer and smaller clusters in MLL4$^{LoF}$ MSCs with respect to MLL4$^{WT}$ MSCs, possibly suggesting that both the protein abundance and the chromatin environment of MLL4$^{LoF}$ MSCs could influence cluster formation and dynamics.

In the future, the observation of the motion of individual molecules of MLL4 by Single-particle tracking (SPT) could clarify the phase separation behavior of this protein. Indeed, it would be interesting to assess whether the mobility of MLL4 molecules could be influenced by its diffusion in accessible versus compacted chromatin regions (e.g nuclear periphery) in both physiological and perturbed chromatin states.

## 5.2 Nuclear condensates are modulated by changes in substrate stiffness

By confocal microscopy, we investigated the level and distribution inside the nucleus of some of the chromatin-binding proteins that are part of the Transcriptional (e.g. MLL4, BRD4) and PcG condensates (RING1B, BMI) at two different substrate rigidities: 0.5 and 32 kPa, and found that these proteins are responsive to changes in substrate stiffness. Specifically, we observed in MSCs WT plated in the soft matrix an increase of PcG-associated proteins, counterbalanced by a decrease of MLL4 and
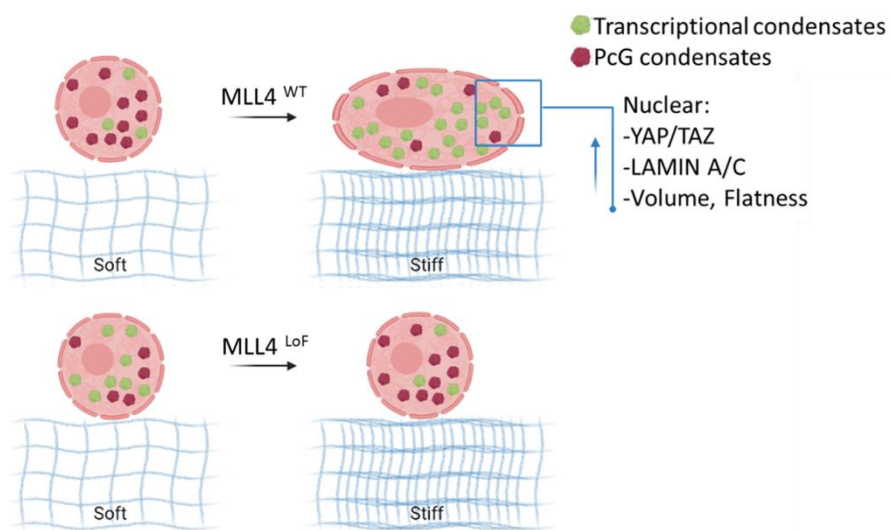
BRD4 (Figure 17). In this condition, LAMIN A/C and YAP/TAZ, key players in mediating nuclear mechanotransduction, respond in accordance to the stimulus applied as reported in the literature: at 0.5 kPa, LAMIN A/C signal decreases at the nuclear periphery, whether YAP/TAZ localizes mainly in the cytosol (Figure 19) (Swift *et al.*, 2013). As regards the nuclear morphology, when MSCs were plated in the soft matrix, nuclei acquired a balled-up conformation with a decreased volume and flatness, indicating low nuclear stress.

Interestingly, MLL4 LoF (Q4092X) alters MSCs response to the increase of ECM stiffness, by impairing nuclear condensates distribution and nuclear architecture, suggesting a possible role for Transcriptional and Polycomb condensates in cell mechanoresponsiveness (Figure 35).

These data have been confirmed in an independent clone of MSCs carrying a different truncating mutation of MLL4 (P4093X) (Figure 21), supporting the relevance fo these findings. Furthermore, by restoring PcG abundance in MLL4^LoF MSCs through the overexpression of histone H3.3 carrying the p.Lys27Met alteration (H3.3 K27M), we rescued LAMIN A/C level as well as MLL4 and BMI clustering abundance and distribution (Figure 19).

Although MLL4^LoF MSCs physical parameters such as nuclear volume, flatness, and area are not affected by the changes in matrix rigidity, we observed an increase in NE perimeter in the soft matrix with respect to the stiff one (Figure 20). Interestingly, several studies reported a correlation between the presence of NE invaginations and lamin proteins level. For instance, in diseases caused by LMNA mutations (laminopathies), such as X-linked EDMD, familial partial lipodystrophy (FPLD), dilated cardiomyopathy, limb girdle muscular dystrophy 1B, congenital muscular dystrophy, and progeroid syndromes (include Hutchinson-Gilford progeria syndrome- HGPS, atypical Werner's syndrome- WS, restricted dermopathy- RD, and mandibuloacral dysplasia- MAD), the amount and organization of A-type lamins throughout the

nucleus is decreased or disturbed (Stiekema *et al.*, 2022; Dechat *et al.*, 2008). Moreover, it has been reported that HGPS fibroblasts from donors have lobulated nuclei with an increased number of nuclear invaginations in comparison with normal fibroblasts (Dechat *et al.*, 2008). Decreased LAMIN A/C level in MLL4$^{LoF}$ MSCs likely leads to collapsed nuclei with a higher number of NE invaginations. Furthermore, the presence of these structures within MLL4$^{LoF}$ nuclei is compatible with the evidence that these cells have decreased NE tension, as shown by MiniNesprin1-cpstFRET sensor (Figure 30).

Nuclear envelope invaginations can originate by pushing forces exerted by the polymerization of cytoskeletal filaments or nuclear pulling forces, and are the results of the interaction of several proteins, from A-type lamins to B-type lamins and other lamin-binding proteins (Stiekema *et al.*, 2022). In addition, they are shaped by chromatin-lamin interactions, in particular with the heterochromatic region at the periphery of the nucleus called lamina-associated domains (LADs) (Schoen *et al.*, 2017). Of note, in laminopathic cells, the disrupted integrity of the nuclear lamina leads to disorganized peripheral heterochromatin. For determining nanoscale chromatin compaction we used an assay based on fluorescence lifetime imaging microscopy (FLIM) to measure Förster resonance energy transfer (FRET) between histone-tagged fluorescent proteins (Llères *et al.*, 2009, 2017). The FLIM approach has the advantage of quantitatively measuring the fluorophore lifetime of the donor protein species only, which is independent from the relative concentrations of the interacting proteins and their diffusion rates. By measuring H2B-H2B chromatin interactions we showed that MLL4$^{LoF}$ MSCs are characterized by a higher nucleosome nanocompaction at the periphery of the nucleus in comparison with MLL4$^{WT}$ MSCs (Figure 25). Although we did not specifically look at the constitutive heterochromatin and further experiments are needed to clarify this hypothesis, we can speculate that in MLL4$^{LoF}$ MSCs possible aberrations in chromatin-lamin interactions and LAMIN A/C abundance may contribute to the formation of NE invaginations. Interestingly, we noticed the presence of nuclear invaginations also in MLL4$^{WT}$ MSCs plated at 0.5 kPa (Figure 20); of note, in this condition, MLL4$^{WT}$ MSCs showed decreased LAMIN A/C level and higher chromatin compaction. These

1898    results are in agreement with previous observations of wrinkled nuclei in soft

substrates (0.3 kPa) (Swift *et al.*, 2013).

1900

In concomitance with the response of Transcriptional and PcG condensates to

1902    stiffness rigidity, we also observed changes in chromatin compaction (Figure 26).

In the soft matrix, MLL4[WT] MSCs are characterized by higher nucleosome-

1904    nucleosome interactions as well as a lower level of H4k16ac in comparison to the

stiff matrix. These results are in line with what has been previously reported: indeed,

1906    contact with soft matrices induces in MSCs chromatin remodeling and condensation

(Rabineau *et al.*, 2018; Killaars *et al.*, 2019). However, MLL4[LoF] MSCs did not show a

1908    high- H2B/H2B- FRET chromatin population (80-100% $E_{FRET}$) when in contact with

the soft substrate; instead, we noticed an increase in the low-FRET chromatin

1910    population (5-15% $E_{FRET}$), which is associated with a higher level of H4k16ac in

comparison to the stiff matrix. Altogether, these results suggest that MLL4 LoF

1912    impairs the chromatin remodeling induced by matrix softening.

In Fasciani *et al.*, we demonstrated that the increased PcG clustering in MLL4[LoF]

1914    MSCs leads to more compacted nuclei, as shown by Brillouin Microscopy and

analysis of H4K16ac levels. In MLL4[WT] MSCs plated at 0.5 kPa of substrate rigidity,

1916    we observed an increase of PcG levels, accompanied by an augmented fraction of

compacted chromatin. In the present work, we did not clarify what is the

1918    contribution of PcG proteins or peripheral heterochromatin to promote chromatin

condensation. The use of other microscopy techniques, such as Stochastic Optical

1920    Reconstruction Microscopy (STORM), could facilitate the comprehension of this

process. In particular, this super- resolution microscopy, achieving an axial

1922    resolution of 20nm (Rust, Bates and Zhuang, 2006), could allow us to investigate the

spatial distribution of PcG in relation to nuclear lamina.

1924

All the experiments performed to assess the response of nuclear condensates to

1926    changes in substrate stiffness are imaging-based. Confocal microscopy is particularly

suited to visualize fluorescently-labeled biomolecules clustering inside the nucleus,

1928    in which they appear as bright foci (Sabari, Dall'Agnese and Young, 2020).

Quantification of nuclear signal intensity or puncta features such as number and shape facilitates comparisons of biomolecular condensates formed under different cellular conditions or by different biomolecules. For this reason, we measured nuclear signal intensity and the number of clusters per cell of the proteins of interest (Figure 16-19, 21). Nevertheless, considering that for technical reasons we analyzed the markers of nuclear condensates at the steady state after 48h from plating, we cannot exclude a response of Transcriptional and PcG condensates before this timing, as well as an alteration of the transcript abundance, for which further experiments are needed (qPCR analysis). However, we followed and quantified over time the dynamic assembly and disassembly of MLL4-PrLD clusters in MSCs plated at 0.5 and 32 kPa, showing that substrate stiffness impacts MLL4-PrLD phase separation behavior in living cells (Figure 22). In the soft matrix, MLL4-PrLD forms fewer but larger condensates with respect to the stiff matrix: this may indicate a higher droplet coarsening and fusion. The overall decrease in Transcriptional condensates together with the changes in chromatin compaction could potentially explain the phenotype observed in the soft matrix, even though we did not elucidate the mechanism underneath this phenomenon. Analysis of the phase separation behavior of other proteins (e.g. BMI, MED1) and molecular in-silico simulations, as well as an in-depth study of cluster dynamics through the use of SPT, could help us better understand this process.

MLL4 belongs to the TrxG group of proteins that are known to functionally antagonize PcG proteins by maintaining an active state of gene expression (Schuettengruber *et al.*, 2017). Although we described a perturbation of these proteins in response to mechanical cues, we did not further investigate the impact of these alterations on transcription. However, differential expression analyses in a steady state condition showed that only a small subset of genes encoding for mitotic factors and chromatin architectural proteins was downregulated in MLL4[LoF] MSCs compared with MLL4[WT] MSCs, suggesting a novel function of MLL4 in structuring chromatin architecture rather than primarily affecting global gene expression (Fasciani *et al.*, 2020).

To our knowledge, this study provides for the first time evidence that Polycomb (PRC1 complex) and Transcriptional condensates are modulated by changes in substrate rigidity. Despite that, it has been reported that mechanical strain induces gene expression repression through PRC2-mediated gene silencing, indicating that PcG proteins mediate cell responses to mechanical cues (Le *et al.*, 2016). Interestingly, BRD4, together with YAP, is a key mechanosensor of matrix stiffening in liver fibrosis which regulates patterns of gene expression that initiate and perpetuate fibrosis (Ding *et al.*, 2015; Zhubanchaliyev *et al.,* 2016; Wu *et al.*, 2021). Albeit the differences in the biological context, this piece of evidence is in line with our observation in MLL4$^{WT}$ MSCs of higher BRD4 nuclear signal in the stiffer matrix in comparison to the soft one.

### 5.3 The unbalancing between Transcriptional and PcG condensates increases the susceptibility to nuclear envelope rupture and cell death

The nuclear envelope (NE), comprising the inner and outer nuclear membranes and the lamina, provides a physical barrier between the nuclear interior and the cytoplasm and protects the genome from cytoplasmic components. Loss of NE integrity has been linked to the normal aging process as well as to several pathologies, including cancer and laminopathies (Hatch and Hetzer, 2014). Even in physiological conditions, the physical deformation of the nucleus, being the larger and stiffer organelle of the cell, represents a mechanical challenge during cell migration through the tight pores of the ECM. Considering that MLL4$^{LoF}$ MSCs possess an altered chromatin environment and nuclear structure, we investigated whether cell deformation through confining spaces could induce NE rupture or affect cell survival and migration differentially in MLL4$^{WT}$ and MLL4$^{LoF}$ MSCs. Overall, we observed that *KMT2D* haploinsufficiency leads MSCs nuclei to be more prone to nuclear membrane breakdown with respect to the healthy condition (Figure 27). At the same time, we observed a significant increase in cell death after NE rupture in MLL4$^{LoF}$ MSCs with respect to the MLL4$^{WT}$ MSCs (Figure 27). The decreased LAMIN A/C abundance and NE tension in MLL4$^{LoF}$ MSCs might mutually contribute to both

phenomena (Swift *et al.*, 2013; Harada *et al.*, 2014). Of note, by rescuing PcG activity through the overexpression of H3.3 K27M in MLL4[LoF] MSCs, which in turn re-established LAMIN A/C level, we restored NE integrity in the constrictions of 5 and 3 μm of widths (Figure 28). Furthermore, in support of these data, we observed high cell mortality in MLL4[LoF] MSCs with another mechanical device such as static cell confinement. Under 3 μm of confinement, all MLL4[LoF] nuclei were ruptured (Figure 28). Further experiments will be necessary to assess the exact process that led to increased cell mortality, such as the use of intermediate height between 6 and 3 μm.

The level of chromatin compaction is also known to determine nuclear mechanical properties. Indeed, there are supporting data indicating that chromatin de-condensation diminishes the ability of the nucleus to withstand external mechanical stress (Furusawa *et al.*, 2015). This evidence clashes with the results observed in our MSCs-based KS disease model, in which MLL4[LoF] nuclei are highly compacted. However, a recent work pinpoints a novel role of chromatin in altering nuclear stiffness in order to maintain genome integrity in response to deformation (Nava *et al.*, 2020). Nava *et al.*, demonstrated that stretch triggers a rapid loss of lamina-associated H3K9me3 heterochromatin and subsequent nuclear softening as a protection mechanism to dissipate mechanical stress and preserve the genome from DNA damage. Albeit we did not use stretch as mechanical input, we can speculate that MLL4[LoF] highly compacted nuclei fail to undergo stress-induced nuclear softening, therefore leading to increased cell mortality.

As mentioned, nuclear deformation causes loss of NE integrity, which leads to herniation of chromatin across the NE and compromises genome integrity (Denais *et al.*, 2016; Raab *et al.*, 2016). We still must investigate the degree of DNA damage occurring in this setting, but preliminary data showed that MLL4[LoF] MSCs, at the steady state and plated on glass coverslips, harbor higher levels of DNA damage, as shown by nuclear quantification of 53BP1 (p53-binding protein 1), a crucial component of DNA double-strand break (DSB) signaling and repair (Panier and Boulton, 2014) (Figure 36). In the same plating condition, MLL4[LoF] MSCs also showed

105

2020    low LAMIN A/C levels and increased n° of focal adhesions (vinculin), which represent active sites for actin polymerization and mediate cell migration (Figure 33).

2022    Interestingly, these data are congruent with a recent study showing that stiff ECM, high actomyosin contractility, and low lamin-A favor nuclear rupture, which in turn

2024    promotes DNA damage (Cho *et al.*, 2019).
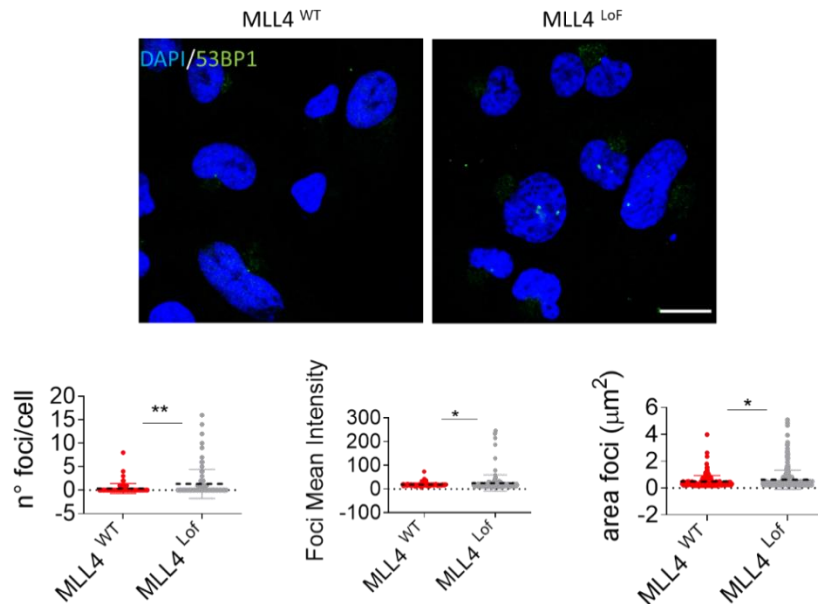


*Figure 36. Quantification of 53BP1 nuclear foci.* Merged confocal images of 53BP1 foci (green) and DAPI (blue) in MLL4$^{WT}$ and MLL $^{LoF}$ (scale bar 10μm). On the bottom, quantification of the n° of foci per cell, foci mean intensity, and area (n≥88). Two-tailed unpaired student's t-test was carried out.

2026    Lastly, by comparing the time of migration through channels with constrictions or porous membranes, we demonstrated that the unbalancing between

2028    Transcriptional and PcG condensates also affects cell migratory capacity that is rescued by the overexpression of the K27M histone variant (Figure 31). The MLL4

2030    LoF phenotype of an increased migration speed could be due to several factors. For instance, high levels of nuclear lamins have been shown to impede 3D migration,

2032    even though promoting cell survival against migration-induced stress (Harada *et al.*, 2014). Hence, low LAMIN A/C levels in MLL4$^{LoF}$ MSCs could favor cell migration,

2034    although compromising cell survival. Another edge could be given by the increased nuclear stiffness of MLL4$^{LoF}$ nuclei. Indeed, global chromatin condensation facilitates

2036    the passage of cells through narrow openings (Gerlitz and Bustin, 2010). Furthermore, the altered nuclear morphology of MLL4$^{LoF}$ MSCs could further ease

2038 the passage through pores/constrictions from a physical point of view. Finally, the

higher number of mechanically active adhesion sites in MLL4<sup>LoF</sup> MSCs with respect

2040 to the healthy condition could contribute to the increased migration capacity as

well. In this last matter, future studies will be directed to understand the relationship

2042 between *KMT2D* haploinsufficiency and the cytoskeletal alterations, to date

unknown.

2044

## 5.4 Conclusion and future perspectives

2046 In this study, we provided evidence that the balancing between active and

repressive nuclear compartments, secured by MLL4 protein, is necessary to

2048 determine cell mechanoresponsiveness to external stimuli and establish

mechanoprotection from nuclear rupture and subsequent cell death under physical

2050 constraints. In addition, we demonstrated that chromatin condensates driven by

Transcriptional and Polycomb proteins are responsive to changes in matrix rigidity.

2052 We found increased level of Transcriptional condensates in the stiff matrix,

counterbalanced by low PcG abundance, *KMT2D* haploinsufficiency affects MSCs

2054 condensates-driven response. These findings reinforce the role of the nucleus as

mechanosensor and suggest a novel role for chromatin biomolecular condensates

2056 as mediators of cell mechano-responses.

Although some of the data presented in this thesis are still preliminary and will need

2058 to be confirmed by further investigation and techniques, the results described in this

work potentially clarify the pathological connection between MLL4 LoF and Kabuki-

2060 Syndrome symptoms. We hypothesized that skeletal and cartilage anomalies, which

are among the most common clinical manifestations in KS-affected individuals,

2062 could be linked to the altered cell mechanoresponsiveness during differentiation,

which is known to be regulated by ECM stiffness.

2064 Key experiments that could strengthen the results shown in this thesis may involve

Single-Particle tracking to better dissect the dynamics of MLL4 PrLD. Furthermore,

2066 genomic approaches such as RNA-seq analysis may be needed to investigate

whether the response of Transcriptional and Polycomb proteins observed at

2068 different substrate stiffness could be associated with broad changes in transcription. In addition, DNA- Fluorescence In Situ Hybridization (DNA- FISH) might be used to

2070 uncover genome–nuclear lamina interactions in MSCs in both physiological and pathological conditions (MLL4 LoF), as well as in different mechanical contexts.

2072 The majority of data collected in this thesis are correlative or descriptive. Hence, future experiments will be centered on elucidating the functional process by which

2074 biomolecular condensates control nuclear mechanical properties. For instance, time-lapse imaging of fluorescent-tagged IDRs in MSCs undergoing nuclear

2076 deformation in microchannels with restrictions could shed light on how nuclear condensates affect cellular responses to external mechanical cues.

2078

# 6. Limitation of the study

In some cases, both the experimental design and test combination appeared

2080 underpowered for detecting the hypothetical effect of interest. Specifically, microchannels and optogenetics experiments as well as the migration assay showed

2082 variability between samples (Figures 15, 27, 28, 31, 32). For this reason, some of the results need to be confirmed by further replicates to improve the statistical analysis

2084 and ensure the robustness of the findings. Furthermore, the overall cluster intensities and area of some of the MLL4-PrLD condensation experiments appeared

2086 highly variable between different replicates. Although we are aware that part of this variability is due to technical reasons (two different hardware settings have been

2088 used as specified in paragraph 3.13), it would be important to exclude variations in protein levels as potential confounding factors for the observed effects.

# List of acronyms

| | |
|---|---|
| AUC | Area Under the Curve |
| $C_{critical}$ | Critical Concentration |
| $E_{FRET}$ (%) | FRET Efficiency (%) |
| IDR | Intrinsically Disordered Region |
| KS | Kabuki Syndrome |
| LLPS | Liquid-Liquid Phase Separation |
| LoF | Loss of Function |
| $MLL4^{LoF}/ MLL4^{LoF\_1}$ | MSCs MLL4 $^{Q4092X}$ |
| $MLL4^{LoF\_2}$ | MSCs MLL4 $^{P4093X}$ |
| $MLL4^{WT}/ MLL4^{WT\_1}$ | MSCs WT Clone 1 |
| $MLL4^{WT\_2}$ | MSCs WT Clone 2 |
| MSCs | Mesenchymal Stem Cells |
| NE | Nuclear Envelope |
| PcG | Polycomb |
| PrLD | Prion-Like Domain |
| SPT | Single- Particle Tracking |

# Bibliography

- Alam, H. et al. (2020) 'KMT2D Deficiency Impairs Super-Enhancers to Confer a Glycolytic Vulnerability in Lung Cancer.', Cancer cell, 37(4), pp. 599-617.e7. doi: 10.1016/j.ccell.2020.03.005.

- Alberti, S. (2017) 'Phase separation in biology', Current Biology, 27(20), pp. R1097–R1102. doi: https://doi.org/10.1016/j.cub.2017.08.069.

- Ang, S.-Y. et al. (2016) 'KMT2D regulates specific programs in heart development via histone H3 lysine 4 di-methylation.', Development (Cambridge, England), 143(5), pp. 810–821. doi: 10.1242/dev.132688.

- Antonacci, G. et al. (2018) 'Background-deflection Brillouin microscopy reveals altered biomechanics of intracellular stress granules by ALS protein FUS.', Communications biology, 1, p. 139. doi: 10.1038/s42003-018-0148-x.

- Banani, S. F. et al. (2017) 'Biomolecular condensates: organizers of cellular biochemistry', Nature Reviews Molecular Cell Biology, 18(5), pp. 285–298. doi: 10.1038/nrm.2017.7.

- Bergamaschi, A. et al. (2008) 'Extracellular matrix signature identifies breast cancer subgroups with different clinical outcome.', The Journal of pathology. England, 214(3), pp. 357–367. doi: 10.1002/path.2278.

- Le Berre, M., Aubertin, J. and Piel, M. (2012) 'Fine control of nuclear confinement identifies a threshold deformation leading to lamina rupture and induction of specific genes', Integrative Biology, 4(11), pp. 1406–1414. doi: 10.1039/c2ib20056b.

- Bögershausen, N. and Wollnik, B. (2013) 'Unmasking Kabuki syndrome.', Clinical genetics. Denmark, 83(3), pp. 201–211. doi: 10.1111/cge.12051.

- Boniel, S. et al. (2021) 'Kabuki Syndrome—Clinical Review with Molecular Aspects', Genes, 12(4). doi: 10.3390/genes12040468.

- Bonnans, C., Chou, J. and Werb, Z. (2014) 'Remodelling the extracellular matrix in development and disease.', Nature reviews. Molecular cell biology, 15(12), pp.

786–801. doi: 10.1038/nrm3904.

- Bustin, M. and Misteli, T. (2016) 'Nongenetic functions of the genome.', Science (New York, N.Y.), 352(6286), p. aad6933. doi: 10.1126/science.aad6933.

- Calo, E. and Wysocka, J. (2013) 'Modification of enhancer chromatin: what, how, and why?', Molecular cell, 49(5), pp. 825–837. doi: 10.1016/j.molcel.2013.01.038.

- Chen, M. B. et al. (2013) 'Mechanisms of tumor cell extravasation in an in vitro microvascular network platform.', Integrative biology : quantitative biosciences from nano to macro, 5(10), pp. 1262–1271. doi: 10.1039/c3ib40149a.

- Cheon, C.-K. and Ko, J. M. (2015) 'Kabuki syndrome: clinical and molecular characteristics.', Korean journal of pediatrics, 58(9), pp. 317–324. doi: 10.3345/kjp.2015.58.9.317.

- Cho, S. et al. (2019) 'Mechanosensing by the Lamina Protects against Nuclear Rupture, DNA Damage, and Cell-Cycle Arrest.', Developmental cell, 49(6), pp. 920-935.e5. doi: 10.1016/j.devcel.2019.04.020.

- Chou, S.-J. et al. (2016) 'Analysis of spatial-temporal gene expression patterns reveals dynamics and regionalization in developing mouse brain', Scientific Reports, 6(1), p. 19274. doi: 10.1038/srep19274.

- Dechat, T. et al. (2008) 'Nuclear lamins: major factors in the structural organization and function of the nucleus and chromatin.', Genes & development, 22(7), pp. 832–853. doi: 10.1101/gad.1652708.

- Dechat, T., Gesson, K. and Foisner, R. (2010) 'Lamina-independent lamins in the nuclear interior serve important functions.', Cold Spring Harbor symposia on quantitative biology. United States, 75, pp. 533–543. doi: 10.1101/sqb.2010.75.018.

- Denais, C. M. et al. (2016) 'Nuclear envelope rupture and repair during cancer cell migration.', Science (New York, N.Y.), 352(6283), pp. 353–358. doi: 10.1126/science.aad7297.

- Ding, N. et al. (2015) 'BRD4 is a novel therapeutic target for liver fibrosis.', Proceedings of the National Academy of Sciences of the United States of America, 112(51), pp. 15713–15718. doi: 10.1073/pnas.1522163112.

- Eeftens, J. M. et al. (2021) 'Polycomb condensates can promote epigenetic marks

but are not required for sustained chromatin compaction', Nature Communications, 12(1), p. 5888. doi: 10.1038/s41467-021-26147-5.

- Fagnocchi, L., Poli, V. and Zippo, A. (2018) 'Enhancer reprogramming in tumor progression: a new route towards cancer cell plasticity.', Cellular and molecular life sciences : CMLS. Switzerland, 75(14), pp. 2537–2555. doi: 10.1007/s00018-018-2820-1.

- Fasciani, A. et al. (2020) 'MLL4-associated condensates counterbalance Polycomb-mediated nuclear mechanical stress in Kabuki syndrome', Nature Genetics, 52(12), pp. 1397–1411. doi: 10.1038/s41588-020-00724-8.

- Feric, M. and Misteli, T. (2021) 'Phase separation in genome organization across evolution', Trends in Cell Biology, 31(8), pp. 671–685. doi: https://doi.org/10.1016/j.tcb.2021.03.001.

- Forbes, D. J., Kirschner, M. W. and Newport, J. W. (1983) 'Spontaneous formation of nucleus-like structures around bacteriophage DNA microinjected into Xenopus eggs.', Cell. United States, 34(1), pp. 13–23. doi: 10.1016/0092-8674(83)90132-0.

- Furusawa, T. et al. (2015) 'Chromatin decompaction by the nucleosomal binding protein HMGN5 impairs nuclear sturdiness', Nature Communications, 6(1), p. 6138. doi: 10.1038/ncomms7138.

- Gerlitz, G. and Bustin, M. (2010) 'Efficient cell migration requires global chromatin condensation.', Journal of cell science, 123(Pt 13), pp. 2207–2217. doi: 10.1242/jcs.058271.

- Gibson, B. A. et al. (2019) 'Organization of Chromatin by Intrinsic and Regulated Phase Separation', Cell, 179(2), pp. 470-484.e21. doi: https://doi.org/10.1016/j.cell.2019.08.037.

- Harada, T. et al. (2014) 'Nuclear lamin stiffness is a barrier to 3D migration, but softness can limit survival.', The Journal of cell biology, 204(5), pp. 669–682. doi: 10.1083/jcb.201308029.

- Hatch, E. and Hetzer, M. (2014) 'Breaching the nuclear envelope in development and disease.', The Journal of cell biology, 205(2), pp. 133–141. doi: 10.1083/jcb.201402003.

- Herz, H.-M. et al. (2012) 'Enhancer-associated H3K4 monomethylation by

Trithorax-related, the Drosophila homolog of mammalian Mll3/Mll4.', Genes & development, 26(23), pp. 2604–2620. doi: 10.1101/gad.201327.112.

- Hnisz, D. et al. (2013) 'Super-enhancers in the control of cell identity and disease.', Cell, 155(4), pp. 934–947. doi: 10.1016/j.cell.2013.09.053.

- Huisman, C. et al. (2021) 'The histone H3-lysine 4-methyltransferase Mll4 regulates the development of growth hormone-releasing hormone-producing neurons in the mouse hypothalamus', Nature Communications, 12(1), p. 256. doi: 10.1038/s41467-020-20511-7.

- Humphries, J. D. et al. (2007) 'Vinculin controls focal adhesion formation by direct interactions with talin and actin.', The Journal of cell biology, 179(5), pp. 1043–1057. doi: 10.1083/jcb.200703036.

- Inoue, A. and Zhang, Y. (2014) 'Nucleosome assembly is required for nuclear pore complex assembly in mouse zygotes.', Nature structural & molecular biology, 21(7), pp. 609–616. doi: 10.1038/nsmb.2839.

- Killaars, A. R. et al. (2019) 'Extended Exposure to Stiff Microenvironments Leads to Persistent Chromatin Remodeling in Human Mesenchymal Stem Cells.', Advanced science (Weinheim, Baden-Wurttemberg, Germany), 6(3), p. 1801483. doi: 10.1002/advs.201801483.

- Kim, T.-K. and Shiekhattar, R. (2015) 'Architectural and Functional Commonalities between Enhancers and Promoters.', Cell, 162(5), pp. 948–959. doi: 10.1016/j.cell.2015.08.008.

- Kumar, A. et al. (2014) 'ATR mediates a checkpoint at the nuclear envelope in response to mechanical stress.', Cell, 158(3), pp. 633–646. doi: 10.1016/j.cell.2014.05.046.

- Van Laarhoven, P. M. et al. (2015) 'Kabuki syndrome genes KMT2D and KDM6A: functional analyses demonstrate critical roles in craniofacial, heart and brain development', Human Molecular Genetics, 24(15), pp. 4443–4453. doi: 10.1093/hmg/ddv180.

- Le, H. Q. et al. (2016) 'Mechanical regulation of transcription controls Polycomb-mediated gene silencing during lineage commitment.', Nature cell biology. England, 18(8), pp. 864–875. doi: 10.1038/ncb3387.

- Lederer, D. et al. (2012) 'Deletion of KDM6A, a histone demethylase interacting with MLL2, in three patients with Kabuki syndrome.', American journal of human genetics, 90(1), pp. 119–124. doi: 10.1016/j.ajhg.2011.11.021.

- Lee, D. S. W., Strom, A. R. and Brangwynne, C. P. (2022) 'The mechanobiology of nuclear phase separation.', APL bioengineering, 6(2), p. 21503. doi: 10.1063/5.0083286.

- Lewis, P. W. et al. (2013) 'Inhibition of PRC2 activity by a gain-of-function H3 mutation found in pediatric glioblastoma.', Science (New York, N.Y.), 340(6134), pp. 857–861. doi: 10.1126/science.1232245.

- Llères, D. et al. (2009) 'Quantitative analysis of chromatin compaction in living cells using FLIM-FRET.', The Journal of cell biology, 187(4), pp. 481–496. doi: 10.1083/jcb.200907029.

- Llères, D. et al. (2017) 'Quantitative FLIM-FRET Microscopy to Monitor Nanoscale Chromatin Compaction In Vivo Reveals Structural Roles of Condensin Complexes.', Cell reports. United States, 18(7), pp. 1791–1803. doi: 10.1016/j.celrep.2017.01.043.

- Lomakin, A. J. et al. (2020) 'The nucleus acts as a ruler tailoring cell responses to spatial constraints.', Science (New York, N.Y.), 370(6514). doi: 10.1126/science.aba2894.

- Malashicheva, A. and Perepelina, K. (2021) 'Diversity of Nuclear Lamin A/C Action as a Key to Tissue-Specific Regulation of Cellular Identity in Health and Disease.', Frontiers in cell and developmental biology, 9, p. 761469. doi: 10.3389/fcell.2021.761469.

- Maniatis, T., Goodbourn, S. and Fischer, J. A. (1987) 'Regulation of inducible and tissue-specific gene expression.', Science (New York, N.Y.). United States, 236(4806), pp. 1237–1245. doi: 10.1126/science.3296191.

- Margot, H. et al. (2020) 'Immunopathological manifestations in Kabuki syndrome: a registry study of 177 individuals', Genetics in Medicine, 22(1), pp. 181–188. doi: https://doi.org/10.1038/s41436-019-0623-x.

- Martin, E. W. and Holehouse, A. S. (2020) 'Intrinsically disordered protein regions and phase separation: sequence determinants of assembly or lack thereof.',

Emerging topics in life sciences. England, 4(3), pp. 307–329. doi: 10.1042/ETLS20190164.

- Maurer, M. and Lammerding, J. (2019) 'The Driving Force: Nuclear Mechanotransduction in Cellular Function, Fate, and Disease.', Annual review of biomedical engineering, 21, pp. 443–468. doi: 10.1146/annurev-bioeng-060418-052139.

- Nava, M. M. et al. (2020) 'Heterochromatin-Driven Nuclear Softening Protects the Genome against Mechanical Stress-Induced Damage.', Cell, 181(4), pp. 800-817.e22. doi: 10.1016/j.cell.2020.03.052.

- Ng, S. B. et al. (2010) 'Exome sequencing identifies MLL2 mutations as a cause of Kabuki syndrome.', Nature genetics, 42(9), pp. 790–793. doi: 10.1038/ng.646.

- Niikawa, N. et al. (1981) 'Kabuki make-up syndrome: a syndrome of mental retardation, unusual facies, large and protruding ears, and postnatal growth deficiency.', The Journal of pediatrics. United States, 99(4), pp. 565–569. doi: 10.1016/s0022-3476(81)80255-7.

- Niikawa, N. et al. (1988) 'Kabuki make-up (Niikawa-Kuroki) syndrome: a study of 62 patients.', American journal of medical genetics. United States, 31(3), pp. 565–589. doi: 10.1002/ajmg.1320310312.

- Northcott, J. M. et al. (2018) 'Feeling Stress: The Mechanics of Cancer Progression and Aggression.', Frontiers in cell and developmental biology, 6, p. 17. doi: 10.3389/fcell.2018.00017.

- Oskarsson, T. et al. (2011) 'Breast cancer cells produce tenascin C as a metastatic niche component to colonize the lungs.', Nature medicine, 17(7), pp. 867–874. doi: 10.1038/nm.2379.

- Panciera, T. et al. (2017) 'Mechanobiology of YAP and TAZ in physiology and disease', Nature Reviews Molecular Cell Biology, 18(12), pp. 758–770. doi: 10.1038/nrm.2017.87.

- Panier, S. and Boulton, S. J. (2014) 'Double-strand break repair: 53BP1 comes into focus', Nature Reviews Molecular Cell Biology, 15(1), pp. 7–18. doi: 10.1038/nrm3719.

- Plys, A. J. et al. (2019) 'Phase separation of Polycomb-repressive complex 1 is

governed by a charged disordered region of CBX2.', Genes & development, 33(13–14), pp. 799–813. doi: 10.1101/gad.326488.119.

- Poli, A. et al. (2022) 'PIP4K2B is a mechanosensor and induces heterochromatin-driven nuclear softening through UHRF1', bioRxiv. Cold Spring Harbor Laboratory. doi: 10.1101/2022.03.25.485814.

- Raab, M. et al. (2016) 'ESCRT III repairs nuclear envelope ruptures during cell migration to limit DNA damage and cell death.', Science (New York, N.Y.). United States, 352(6283), pp. 359–362. doi: 10.1126/science.aad7611.

- Rabineau, M. et al. (2018) 'Chromatin de-condensation by switching substrate elasticity', Scientific Reports, 8(1), p. 12655. doi: 10.1038/s41598-018-31023-2.

- Rape, A. D., Guo, W.-H. and Wang, Y.-L. (2011) 'The regulation of traction force in relation to cell shape and focal adhesions.', Biomaterials, 32(8), pp. 2043–2051. doi: 10.1016/j.biomaterials.2010.11.044.

- Rawlings, J. S. et al. (2011) 'Chromatin condensation via the condensin II complex is required for peripheral T-cell quiescence.', The EMBO journal, 30(2), pp. 263–276. doi: 10.1038/emboj.2010.314.

- Rust, M. J., Bates, M. and Zhuang, X. (2006) 'Sub-diffraction-limit imaging by stochastic optical reconstruction microscopy (STORM)', Nature Methods, 3(10), pp. 793–796. doi: 10.1038/nmeth929.

- Sabari, B. R. et al. (2018) 'Coactivator condensation at super-enhancers links phase separation and gene control.', Science (New York, N.Y.), 361(6400). doi: 10.1126/science.aar3958.

- Sabari, B. R., Dall'Agnese, A. and Young, R. A. (2020) 'Biomolecular Condensates in the Nucleus', Trends in Biochemical Sciences, 45(11), pp. 961–977. doi: https://doi.org/10.1016/j.tibs.2020.06.007.

- Sanulli, S. et al. (2019) 'HP1 reshapes nucleosome core to promote phase separation of heterochromatin', Nature, 575(7782), pp. 390–394. doi: 10.1038/s41586-019-1669-2.

- Schoen, I. et al. (2017) 'Nanoscale invaginations of the nuclear envelope: Shedding new light on wormholes with elusive function.', Nucleus (Austin, Tex.), 8(5), pp. 506–514. doi: 10.1080/19491034.2017.1337621.

- Schuettengruber, B. et al. (2017) 'Genome Regulation by Polycomb and Trithorax: 70 Years and Counting.', Cell. United States, 171(1), pp. 34–57. doi: 10.1016/j.cell.2017.08.002.

- Sekar, R. B. and Periasamy, A. (2003) 'Fluorescence resonance energy transfer (FRET) microscopy imaging of live cell protein localizations.', The Journal of cell biology, 160(5), pp. 629–633. doi: 10.1083/jcb.200210140.

- Shi, B. et al. (2021) 'UTX condensation underlies its tumour-suppressive activity', Nature, 597(7878), pp. 726–731. doi: 10.1038/s41586-021-03903-7.

- Shogren-Knaak, M. et al. (2006) 'Histone H4-K16 acetylation controls chromatin structure and protein interactions.', Science (New York, N.Y.). United States, 311(5762), pp. 844–847. doi: 10.1126/science.1124000.

- Solovei, I. et al. (2009) 'Nuclear architecture of rod photoreceptor cells adapts to vision in mammalian evolution.', Cell. United States, 137(2), pp. 356–368. doi: 10.1016/j.cell.2009.01.052.

- Stiekema, M. et al. (2022) 'The Role of Lamins in the Nucleoplasmic Reticulum, a Pleiomorphic Organelle That Enhances Nucleo-Cytoplasmic Interplay.', Frontiers in cell and developmental biology, 10, p. 914286. doi: 10.3389/fcell.2022.914286.

- Strom, A. R. et al. (2017) 'Phase separation drives heterochromatin domain formation', Nature, 547(7662), pp. 241–245. doi: 10.1038/nature22989.

- Swift, J. et al. (2013) 'Nuclear lamin-A scales with tissue stiffness and enhances matrix-directed differentiation.', Science (New York, N.Y.), 341(6149), p. 1240104. doi: 10.1126/science.1240104.

- Sze, C. C. and Shilatifard, A. (2016) 'MLL3/MLL4/COMPASS Family on Epigenetic Regulation of Enhancer Function and Cancer.', Cold Spring Harbor perspectives in medicine, 6(11). doi: 10.1101/cshperspect.a026427.

- Venturini, V. et al. (2020) 'The nucleus measures shape changes for cellular proprioception to control dynamic cell behavior.', Science (New York, N.Y.). United States, 370(6514). doi: 10.1126/science.aba2644.

- Wang, J. et al. (2018) 'A Molecular Grammar Governing the Driving Forces for Phase Separation of Prion-like RNA Binding Proteins.', Cell, 174(3), pp. 688-699.e16. doi: 10.1016/j.cell.2018.06.006.

- Wolf, K. et al. (2013) 'Physical limits of cell migration: control by ECM space and nuclear deformation  and tuning by proteolysis and traction force.', The Journal of cell biology, 201(7), pp. 1069–1084. doi: 10.1083/jcb.201210152.

- Wu, C. et al. (2021) 'Hepatic BRD4 Is Upregulated in Liver Fibrosis of Various Etiologies and  Positively Correlated to Fibrotic Severity.', Frontiers in medicine, 8, p. 683506. doi: 10.3389/fmed.2021.683506.

- Zhubanchaliyev, A. et al. (2016) 'Targeting Mechanotransduction at the Transcriptional Level: YAP and BRD4 Are  Novel Therapeutic Targets for the Reversal of Liver Fibrosis.', Frontiers in pharmacology, 7, p. 462. doi: 10.3389/fphar.2016.00462.